

# ENGINEERING PERSPECTIVE

## CONTENTS

### Review Articles

	<u>Page Number</u>
<b>Musabyimana JOSEE, Kazima SOSTHENE, Turabimana PACIFIQUE</b> Review of semi-active suspension based on Magneto-rheological damper .....	38-51

### Research Articles

<b>Oğuzhan KARAKAŞ, Umut Buğra ŞEKER, Hamit SOLMAZ</b> Modeling of an Electric Bus Using MATLAB/Simulink and Determining Cost Saving for a Realistic City Bus Line Driving Cycle .....	52-62
--	-------

<b>Seyed Mohammad Safieddin ARDEBİLİ, Çağatay NACAĞ, Tolga KOCAKULAK, Mustafa BABAGİRAY</b> Experimental investigation and optimization of HCCI engine fueled by isopropanol and heptane mixture .....	63-78
---	-------

<b>Tolga KOCAKULAK, Venkata Krishna Teja THALLAPALLI, Ahmet Onur KIYAKLI</b> Modeling of an Electric Tractor and Determining Energy Consumption Values In Different Duties .....	79-85
---	-------

# ENGINEERING PERSPECTIVE

An International Journal

Volume: 1

Issue: 2

30 June 2021

ENGINEERING PERSPECTIVE

Volume: 1

Issue: 2

30 June 2021



## Review of semi-active suspension based on Magneto-rheological damper

Musabyimana Josee<sup>1\*</sup>, Kazima Sosthene<sup>2</sup>, Turabimana Pacifique<sup>2</sup>

<sup>1</sup> *Electrical and Electronic Engineering Department, College science and Technology, University of Rwanda, 3900, Kigali, Rwanda*

<sup>2</sup> *Mechanical Engineering Department, Rwanda Polytechnic- IPRC Gishari, 60 Rwamagana, Rwanda*

### ABSTRACT

Vehicle suspension system plays a critical role in transferring static and dynamic loads produced by the vibration of vehicle body and wheels and absorbing shock vibration caused by road roughness. Low damping provides a better vehicle mass isolation and it give a ride comfort and hard damping provides vehicle stability with good road holding. The need to enhance conflicting odds between ride comfort and vehicle stability makes the design of the suspension a significant part particularly for off- road vehicles. Passive suspension can't mitigate tradeoff between ride comfort and vehicle stability, because it presents a high frequency vibration. It is in this line various types of suspension, like semi- active suspension, active suspension and intelligent suspension have been developed to reduce this compromise need. This paper aims to describe in details different types of vehicle suspensions, their characteristics, and their working principles mode. It illustrates in details the magneto rheological fluid (intelligent fluid) properties, compositions, mechanical model of Magneto-rheological damper like Bingham model and Bouc-Wen model. It also reviews semi active suspension control strategies based on Magneto rheological damper, like skyhook, ground hook, sliding mode, fuzzy logic and linear quadratic Gaussian. Simulations shows that a combination of more than two control strategies provide a better vehicle comfort and vehicle stability at the same time.

**Keywords:** Semi-active suspension; Magneto-rheological damper; control strategies

#### History

Received: 13.04.2021

Accepted: 25.05.2021

#### Author Contacts

\*Corresponding Author

e-mail addresses: [josee.musabyimana@gmail.com](mailto:josee.musabyimana@gmail.com), [kazima10@gmail.com](mailto:kazima10@gmail.com)

Orcid numbers : 0000-0003-4433-9586; 0000-0002-4427-130X; 0000-0003-2422-9056

<http://dx.doi.org/10.29228/eng.pers.50853>

## 1. Introduction

The main key responsibilities suspension is to ensure ride comfort and road holding. It transfers different load and ground forces to the vehicle body. A tradition vehicle suspension constitutes by a spring coil spring or air spring and a damping element. The coefficients of damping element and spring are selected based on comfort, road holding, and handling characteristics[1]. Even if conventional suspensions may thrive a trade-off between ride comfort and road holding as though their spring and damping coefficients cannot be adjustably tuned depending on driving efforts and road situation. It means that good ride comfort and road holding is gotten only under the designed circumstances. The studies and investigations on intelligent suspension with the development of micro-processor, sensors and actuators in 1980s have showed a great impact on avoiding the trade off by controlling the damping characteristics of suspensions. Based on the mode of generation of the desired control forces, intelligent suspension systems can be categorized into two main types: active and semi-active. The active suspension often requires significant amount of external energy to produce the desired control damping forces. It is achieved by using pneumatic or hydraulic actuators .

### 1.1 Types of suspension

In automotive dynamic era, suspension system is classified into primary and secondary, the primary suspension ensures the connection between vehicle body and wheels and secondary type represent the seat. There are two basic types of elements in tradition suspension systems. These elements are springs and dampers. The spring in a vehicle's suspension system ensure the mount of static weight of the vehicle and storage of energy applied to the vehicle body. The damper ensures the dissipation vibration energy and monitor different forces from the road transmitted to the vehicle. Basically the role and form of a suspension remain the same regardless of the category of suspension or automobile. Primary suspensions will be classified into passive, active and semi-active suspension.

#### 1.1.1 Passive suspension

As it shown in the Figure1 passive suspension is a type of suspension which implies the control of inherent odds between minimum-frequency and maximum-frequency vibration mitigation.

This kind suspension system has of two important elements an energy evacuating element (shock absorber), which is the damper, and an energy-storing element, which is the spring. As these two elements can't give energy to the system, reason why this type of suspension systems is named passive. Passive suspension systems are exposed to different tradeoffs when they applied to a huge vibration frequencies[2]. Passive dampers figure out the conventional shock absorbers mostly applicable to many vehicles. They have the fixed damping characteristics, i.e. their damping characteristics cannot be adjusted while the car is being driven and thus, they are designed to achieve the most convenient trade-off between ride, road holding, and stability[3].

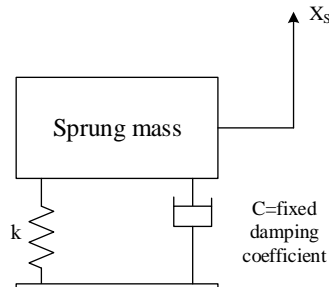


Figure 1 Passive suspension

A high damping suspension will lead best vehicle road handling. However, it transmits much of the road forces to the vehicle body. Whenever the vehicle is riding at low speed on a harsh road or at high speed in a straight line, this will be perceived as a tough ride. The harsh ride is obnoxious for the drivers because it can damage the payloads or cause an accident. A soft damping suspension will lead a more comfortable drive, but may substantially mitigate the stability while the car turning, changing the lane, or exiting the ramp. Best design of a passive suspension can adjust some extensions on improving ride and road handling, but cannot remove this odd as indicated in Figure 2[28].

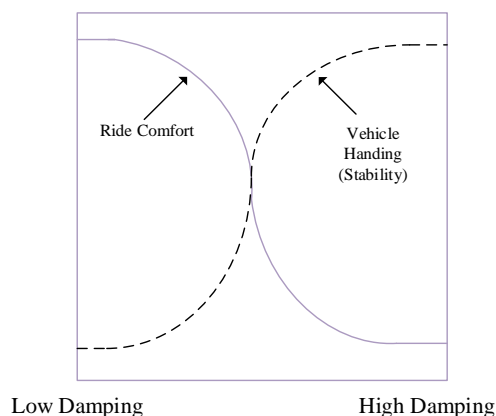


Figure 2 Passive suspension trade off

An ideal suspension system should provide good vibration isolation, i.e. minimum acceleration of the body mass, and ensure the maximal acceptable relative displacement between the vehicle body and different suspension components.

### 1.1.2 Active suspension

The active suspension is a kind of suspension where the passive shock absorber (damper) or both the passive damper and spring are replaced by an actuator force as it shown in the Figure 3. Actuator force has the capacity to the spring and the damper to add and dissipate energy from the system, inversely to a passive damper, can only dissipates energy. In an active suspension, necessary displacement and velocity is applied independently by the actuator force. In active suspension the active force is provided by actuator, which is monitored and controlled by a control algorithm utilizing data from sensors mounted to the vehicle[4]. The active suspension has two important parties' actuator and spring. The spring has a role supporting the static load of sprung mass and force actuator provides the necessary reactive force to mitigate or assimilate deflection caused by road abnormal. The actuator may be hydraulically, electromagnetically, pneumatically, or hybrid systems. These actuator systems are controlled and monitored by electric drives, the electric power of these drives is provided by the battery of vehicle or any other system in vehicle. Based to the high force ability, the easy design, advanced of technology, and commercial availability of the many parts, the hydraulic systems are commonly utilized in control of sprung systems of vehicle. The active suspension system equipped with electromagnetic actuator is named electromagnetic active suspension system; it is constituted by spring and electromagnetic actuator fixed in parallel combination between vehicle body and unsprung mass. The electromagnetic actuator is controlled by embedded systems which supply the required electric power of the actuator. It gives active controlled force to mitigate road shocks in small time, eliminates the roll and pitch vibration, and optimize road handling and ride comfort. When the actuator is operated and mounted mechanically it provides a high bandwidth active suspension and control body mass and unsprung mass. Low-bandwidth is provided to active suspension monitoring the vehicle body (sprung mass) when the active actuator operates and mounted mechanically in series with the spring and the damper. Generally, the range frequencies of the unsprung mass vary between 10-15 Hz, and the range of sprung mass frequency vary between 1-2 Hz. The desired frequency bandwidth determines the price of active suspension. When the desired bandwidth is limited the cost of control force actuator is minimize as cost of active suspension is minimized also[5]. With high damping force of active suspension, the best ride control is gotten. Active suspension operates by constantly sensing various vibrations in the road surface and provides those signals to the ECU, to activate actuator components. Actuators react upon the system to change its behavior, adjusting shock absorber, spring rate and the like, to optimize ride comfort, drivability, and responsiveness. The ECU ensure the collections, analyzes and interpretations of data provided by sensors in little time like 10 milliseconds. Nowadays a new kind of active suspension are being developed with linear electromagnetic motors monitored and controlled by microprocessors and complex mathematics equations[6].

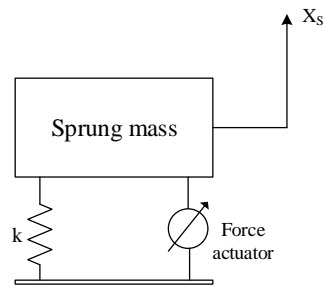


Figure 3 Active suspension

### 1.1.3 Semi- active suspension

Semi-active suspension systems have been investigated and studied in the early 1970's, the tradition spring element is remained in this kind of suspension, however the shock absorber damper is replaced with an adjustable and controllable damper as it is shown in Figure 4 below.

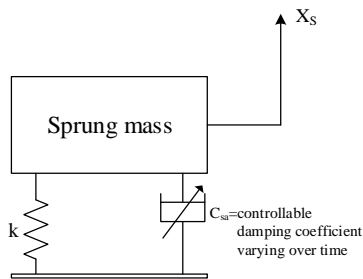


Figure 4. Semi-active suspension

Meanwhile an active suspension system requires an external energy source to activate an actuator which is controls and monitoring the vehicle. The semi-active system utilizes just external power sensors and microcontroller to change the damping characteristics of shock absorber. The embedded microcontroller provides the level of damping force based on a control strategy program to change the shock absorber characteristics to achieve that the necessary damping force. The semi-active suspension dampers adjust their damping force in real time according to a controller strategy which is often based on the system dynamics. By adjusting the damper's fluid resistance movement, or damping coefficient, changes the damper force. Based on its low cost and the capacity to change the damping coefficient independently of damper velocity, within limits, has increased a number of institutions companies and industries to investigate the ability of optimization suspension performance by utilizing semi-active damper technology[7].The implementation of semi-active control law, is based on real time adjustment of damping force. Nowadays, many semi-active dampers are using hydraulic or electromagnetic systems. The first type of semi-active utilizes mechanical valves which are activated by coil or stepper motor to control damper force in a hydraulic damper. The last kind of system uses controllable fluids like electro-rheological or magneto-rheological to change their rheological effect in order to provide the required damping force. Even if the cost of semi-active suspensions remains high compare to the passive suspensions, they are very cheaper compare to active suspensions; as such, they are considered as a more commercially viable option for many vehicles cat-

egories including commercial vehicle. Many researches and studies have shown that semi-active presents the best performance of vehicle dynamic.

## 2. Magneto rheological fluid

Magneto-rheological (MR) materials are classified in smart materials, they are presently being applied many applications. Smart materials are the materials which physical properties can be adjusted or changes by external physical properties such as, temperature, pH, moisture, stress, electric or magnetic fields. Magneto-rheological material has various form of fluids; it can be a gel or even a solid material like elastomers. A magneto-rheological fluid mainly composed by micron-sized iron element that is immersed in carrier oil. Magneto rheological fluid presents the capacity of varying from free-moving liquid state into a semi-solid condition with limited fluid movement in fast response within some milliseconds when applied to the external magnetic field. During the middle of the 20th century, researchers and scientists started to work with fluids able of experiment physical changes in a little time approximatively 10 milliseconds, for example, rheological fluids change viscosity or became semi-solids when are subjected to magnetic fields or electric currents. As it said above their viscosity varies in little time which is less than ten milliseconds. In four decades ago, magneto-rheological fluids were introduced in automotive applications. The main effort were emphasized on autonomous suspensions from the first intelligent approaches[8]. In 1940s Jacob Rabinow [9] invented the fluid , which yield stress and viscosity changes when magnetic field is applied on it; since its invention different applications using MR fluid have been investigated and designed such as dampers, clutches, engine mounts, haptic devices and building dampers, etc[10]. Physical characteristics changes of MR fluid are resulted from the chain-like structures between paramagnetic MR particles in the low permeability solvent[11]. At the normal state, MR fluid presents the isotropic Newtonian behavior because the MR particles move freely as shown in Figure 5 (a). However, when the magnetic field is subjected to the MR fluid, MR fluid forms a chain structure as it is indicated in Figure 5 (b), MR fluids present the anisotropic Bingham behavior which result on resisting on flow and external shear stress. From this property, force or torque of application devices can be easily monitored by the density of magnetic field[12].

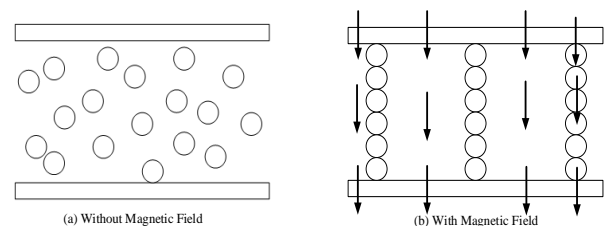


Figure 5 Magneto-rheological fluid

### 2.1 Rheological properties of magneto-rheological fluid

Rheology is the field which study and investigate the flow and changes of materials under exposed forces which is often measured by a rheometer. The process of measurement and test of rheological properties is applicable to all materials. Rheological

properties can be measured from bulk sample twist utilizing a mechanical rheometer or on a micro-scale by using a micro capillary viscometer or an optical technique such as micro-rheology. Various mostly utilized materials and formulations show complex rheological properties, whose viscosity and visco-elasticity can change according to the external conditions subjected, such as temperature, pH, moisture, stress, electric or magnetic fields. Rheological properties is also measured in medical application where it given by internal changes of biopharmaceutical element such as protein concentration, stability or any kind interaction of between its properties[13]. Characteristics effects of magneto rheological fluid is based on increasing or decrease the viscosity of a magneto-rheological fluid and presenting yield stress based on a magnetic field applied on it as indicated by chain form of iron micro sized particles[14]. The MR effect is controlled and monitored by magnetic field intensity and rheological characteristics of magneto-rheological fluid components. It means that rheological properties depend on particles polarity induced magnetic field applied on MR fluid. When there is a presence of a magnetic field, every micro iron particle is changed into a dipole and makes a chain structure with its consecutive particles which can resist failure for some ratio of heat and thus form a semi-solid structure. The interactions between the induced dipoles provoke the micro iron particles to be aligned along exposed field and make a form of column structure. The chain structure will then prevent the fluid motion and consequently rise the viscosity of the suspension[15]. Among other factors, the rheology of MR suspensions depend on, particle shape distribution, quantity of particle, properties of the constituent oil, additional additives, applied magnetic field, temperature [16]. In normal application, the off-state behavior of MR fluids relies on carrier fluid properties, additives, particle volume fraction, etc, as it shown in table 1, while the on-state performance depends on the solidity stage properties and the volume fraction of the solid stage. Rheology of MR fluids is explained in terms of pre-yield as well as post-yield conditions[17].

$$\tau = \begin{cases} G * \gamma_e & \dot{\gamma}_e = 0, \tau < \tau_o \\ \mu \dot{\gamma} + \tau_o & \tau \geq \tau_o \end{cases} \quad (1)$$

Where,  $\gamma_e$  indicates wrench and G the post-yield behavior of MR fluids provided by experimental test.

Table 1. Table of rheological property of MR fluid

Property	Typical value
Initial viscosity	0.2-0.3 [Pa.s] at 25°C
Density	3-4[g/cm <sup>3</sup> ]
Magnetic field strength	150-250[kA/m]
Yield point $\tau_o$	50-100[kPa]
Reaction time	10 milliseconds
Typical supply voltage and current	2-25V, 1-2A
Work temperature	-50 to 150 [°C]

Characteristically, the diameter size of iron particles varies between ranges of 3 to 5 microns meters. If the MR fluid is made with big size particles; it becomes difficult to stabilize the suspended particles. The cheaper iron particles widely available on

different market are carbonyl iron; they are usually inhibited to sizes bigger than 1 or 2 microns. Smaller size particles provide an easy suspension. However, the manufacture process of such particles remains complex. Important smaller sized iron particles available on the market are usually oxides only, like pigments popular used in magnetic recording media[18]. In initial application where there is no presence of magnetic field MR fluids are estimated as Newtonian fluid[19]. Due to low voltage power supplies for MR fluids and relative temperature stability between -40°C and +150 °C, MR fluid present a great advantages more attractive smart materials than Electro Rheological fluids. MR fluids do not show yield stress, but show a variation of viscosity.

## 2.2 Application of MR fluid

Important use of MR fluids are in devices which require rapid continuity and reversible variation in rheological characteristics. Magneto-rheological devices showed a significant advantage during the last decade, since MR fluid links mechanical parts indirectly with electronic embedded controller where the control strategies are incorporated on it, thus determine continuous mechanical characteristics of device. The use of magneto-rheological fluids is advanced of dampers, clutches, brake, control valves, vehicle power steering devices, artificial joints, alternators, sound propagation, chemicals sensing applications and other application. Especially shock absorber are the commonly device which utilizes MR fluid[20].

**Valves:** When the magneto-rheological fluid flows into the valve and magnetic field is subjected to the fluid provoke the increment fluid viscosity. This variation of viscosity generates resistance against flow of fluid in the valve. Thereby the pressure is raised and flow reduces the speed considerably or stops completely. Rosenfeld et al investigated structure and performance of magneto-rheological and electro-rheological valves and the result showed that performance of the MR fluid significantly depends on driving force and active volume of the fluid[22].

**Polishing:** Optical polishing, it is a good application of MR fluid. In working operation when a magnetic field is available, magnetic particles make chain-like structure and provoke abrasive particles to increase the polishing work. The ability of abrasive to keep power and stiffness of a MR fluid is greatly dependent on the size of induced particle. Type of abrasive and concentration are the other parameters which increase the quality of piece surface.

**Brakes:** Magneto-rheological brake is an element which is mainly used in torque transmission. The torque of rotation MR fluids brake is changed quickly according to the magnetic field applied on it. Based on its simplicity design, ease control, the use of MR fluid remain a best choice for braking systems[23].

**Dampers:** Damper is an apparatus which is used to attenuate shock vibration, in addition, to mitigate vibration motion, and to minimize the kinetic force. A damper is called magneto-rheological damper when it contains magneto-rheological fluids and monitored by with variation of magnetic field. They have been designed and developed to provide damping force necessary to the suspension to mitigate any kind of unwanted vibration which occurs in many systems such as seismic, wind induced frequency,

prosthesis control, washing machine, vehicle suspension. Whenever a problem happens in the system, the magneto-rheological damper has the ability to react as a passive damping and lithium stearate. These three components of an MR fluid ensure its magneto rheological characteristics. Modifying any one component will lead the variation of rheological and magneto rheological properties of the MR fluid. An important combination of all the three elements is important to reach the required properties of MR fluid.

### 2.3 Composition of MR fluid

The magneto rheological fluid is composed by three elements, base fluid, metal particle and additives.

Base fluid is a passive or non-magnetic carrier fluid in which the micro-sized iron particles are suspended. The base fluid must possess natural lubrication and damping specifications. In design and good application of MR fluid; base fluid should have a low viscosity and not change with temperature. It is very important that variations of viscosity caused by magnetic field become high compared to variation caused by natural physical parameters. According to the presence of suspended particles base fluid becomes dense. Famous utilized base fluids are hydrocarbon oils, mineral oils and Silicon oils[24].

Metal particle for the best used of this technology a type of metal particles which can provides a fast and easy response of magnetization is needed. Metal particles used in the MR- technology are very small. Size of the particle is around range of 1micrometer ( $\mu\text{m}$ ) to  $7\mu\text{m}$ . The most used and available on market metal particles are carbonyl iron, powder iron and iron cobalt alloys. The properties of these materials provide high magnetic saturation according to that they are is capable for, a good magnetizing chain structure. The concentration of magnetic particles in base fluid may reach to 50%.

Additives to have a better control of MR fluid properties some amounts of additives are required. It has the role of stabilization and control the viscosity. Additives are composed by stabilizers and surfactant; surfactants ensure the decrement rate of settling of the metal particles. While the functions of additives are to control and monitoring the viscosity of the fluid, keep friction between the iron metal particles and to minimize the rate of reduction of the fluid due to long period use of the fluid consequently additives avoid wear of fluid and increase it service life[25]. Most utilized additives are ferrous oleate

## 3. Magneto rheological dampers

Based on specific application, configuration, desired load MR damper have been designed and developed in different sizes. The configuration of a damper can be classified into three main categories based on operation mode, hydraulic housing (cylinder), piston (or MR control valve) structure. Damper is composed by cylinder housing filled with the MR fluid and a control valve (piston) which generates damping force while it is in motion. Generally the control valve is embedded with solenoid which is the magnetic circuit. According to the operating principle modes MR dampers are categorized into four fundamental types: flow-mode dampers, shear-mode dampers, squeeze-mode dampers and pinch-mode dampers. Dampers which are using more than one MR fluid operation mode are called hybrid or mixed mode devices.

Every type has brought particular interest, and it might use various objectives.

### 3.1 Mono tube damper

Mono-tube dampers represent the commonly used magneto rheological devices. Due to its simplicity design and less internal parts mono tube damper remain the best choice for different application. It is widely used in passenger vehicle suspensions. Based on the standpoint of design and implementation of MR dampers, vehicle suspension using MR dampers, mono-tube presents a significant benefit of no having electromechanical valve and minimum number of moving elements. The working principle, the design setting of a characteristically gas-charged MR damper is the same as that of a natural valve-based damper. The floating piston serves on separation of MR fluid from high pressure gas chamber. The role of main piston is to separate the quantity level of magneto rheological fluid into compression chamber and rebound the fluid volume between piston rod and main assembly. As it shown in Figure 6 the piston assembly embeds an annular gap (annulus) to allow the fluid to move between the chambers while in motion. The relative movement of the wheel (unsprung mass) and the body (sprung mass) conduct the fluid flow between the chambers through the annular gap in the piston. The big pressure gas in the chamber under the floating piston is needed for cavitation-free operation, but, it has an opponent effect on cylinder inner surface complete necessities, sealing and friction[3].

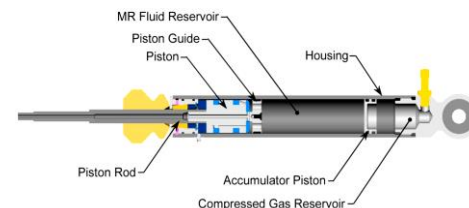


Figure 6. Mono tube MR damper

### 3.2 Twin-tube Damper

As it called the twin-tube MR damper is one of MR damper that possess two fluid reservoirs, one located inner the other one as it is indicated on the Figure7. In this type of setting, the damper possesses two housing an inner and outer housing[26]. The inner housing ensures the guidance of the piston rod assembly, in exactly the similar method as in a mono-tube damper. The volume stayed by the inner housing is assigned to as the inner reservoir. Equally, the volume that is determined by the space between the inner housing and the outer housing is assigned to as the outer reservoir. Hence no air pocket exit because inner reservoir is filled by magneto-rheological fluid[3].

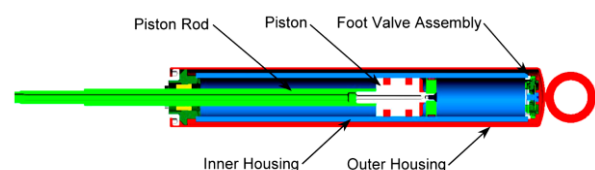


Figure 7 Twin tube MR damper

To arrange variations in volume caused by piston motion, the use of outer reservoir partially filled is necessary. For, the outer housing in a twin-tube damper shows the similar objective as the pneumatic accumulator system in mono-tube dampers. Practically, the valve assembly named foot valve is mounted to the bottom of the inner housing to control the flow of fluid between the two tubes. Whenever the piston rod, move into the damper MR fluid move from the inner tube to the outer tube through the compression of foot valve assembly. The quantity of fluid that flows from the inner reservoir into the outer reservoir is the same as the volume moved by the piston rod as it enters the inner housing. When the piston rod is returned from the damper, MR fluid flows from the outer reservoir into the inner housing tube through the return valve, which is also part of the foot valve assembly part.

system with known operational parameters depending on specifications of the magneto rheological fluid when a magnetic field is not exposed on it[21].

### 3.3 Double ended tube MR damper

The last type of MR damper is named a double-ended damper because a piston rod of equal diameter exceeds from both ends of the damper housing. Figure 8 indicates a cross section view of characteristically double ended MR damper. Because of no variations in volume exists; when the piston rod moves relatively to the damper body, in the other word the double-ended damper does not need an accumulator system. This kind of MR damper is applied in gun coil system, bicycles, seismic vibration avoidance, and wind drift[21].

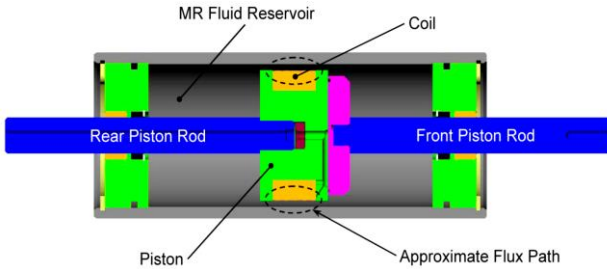


Figure 8 Double-end tube MR damper

## 4. MR damper fundamental models

The fundamental model of MR fluid is based on Bingham solid, which possess the variable yield strength (elasticity)[16]. In Bingham model, fluid flow is provided by Bingham's mathematical equations,

$$\tau = \tau_y(H) + \eta\dot{\gamma} \quad (2)$$

$$\tau < \tau_y$$

$\tau$  represents the fluid stress,  $\tau_y$  denoted the field dependent yield stress,  $H$  defines the magnetic field,  $\dot{\gamma}$  is defined as the fluid shear rate, and  $\eta$  denotes the plastic viscosity; it means, the viscosity if  $H=0$ . Under the fluid's yield stress (pre-yield state), the fluid displays visco elastic characteristics[27].

### 4.1 Flow mode

The working principle of this mode is based on fluid which moves through the two fixed surfaces and magnetic field is exposed perpendicularly to the direction of flow as shown in Figure 9. By adjusting the intensity of magnetic field, the viscosity of fluid is controlled. This mode of MR fluid technology is utilized in different categories of dampers and vibration absorbers and has wide application in automotive industry. In classic dampers, fluid moves from the inner reservoir (cylinder) to outer reservoir (cylinder) through the foot valves. The air and fluid is located in outer. When piston moves down, the fluid volume level in outer cylinder raises and free air behaves as a compressed medium and generates damping force. When the piston spread out, direction of flow gets reverse MR dampers are slightly opponent from the tradition dampers. This type technology does not have the valve like classical dampers. The most application of this mode is the suspension of highway vehicles. In this kind of damper there is an annular orifice passage, through which MR fluid can be transferred from one chamber to another. In normal operation mode ( in absence of magnetic field)condition, fluid can flow through the orifice but when suspension is needed, the solenoid is energized and current starts to pass through the coils windings, and generates the intensity of magnetic field necessary to provide a damping force[24].

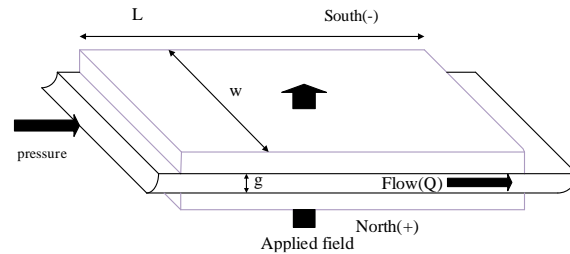


Figure 9 Flow mode

As it is shown in Figure 9 above, pressure variation in this mode is the calculated as sum of pressure generated due to fluid viscosity  $\Delta P$  and pressure developed due to the magnetic field  $\Delta P_\eta$ .

$$\Delta P = \Delta P_\eta + \Delta P_\tau = 12\eta QL/(g^3w) + c\tau_y L/g \quad (3)$$

Where  $\Delta P_\eta$  denoted viscous component of pressure drop,  $\Delta P_\tau$  field dependant of induced yield stress part of pressure drop,  $\eta$  plastic viscosity ( $H=0$ ),  $g$ , fluid gap,  $W$  defines Width of fluid flow orifice,  $Q$  pressure fluid,  $\tau_y$  defines Field dependant yield stress found in Magneto rheological fluid,  $c$ , constant,  $L$  length of fluid flow orifice.

### 4.2 Shear mode

The operation of this mode is based on the fluid which moves between surfaces having same motion and a magnetic field is subjected perpendicular to the direction of flow as shown in Figure 10 [28]. Shear mode of MR fluid technology is utilized in different type of brakes and clutches of automotive. In this mode, the total shear force generated is a summation of the force generated based on viscosity of the fluid ( $F_v$ ) and the force generated based on the magnetic field ( $F_m$ ).

$$\sum F = F_v + F_m \quad (4)$$

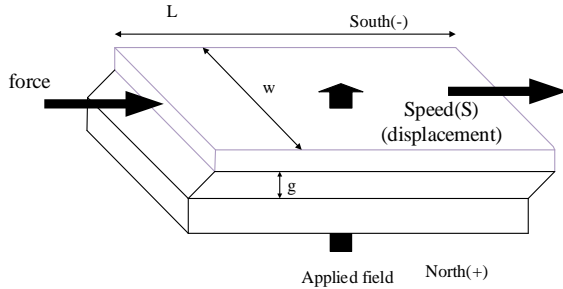


Figure 10 shear mode

The design of squeeze mode Figure 11 is simple and possesses the minimum moving elements hence, less maintenance is desired, and service life is increased. The main disadvantage of MR fluid technology is that the MR fluid becomes dense after elongated use and needs to be changed, also the weight of MR fluid is high caused based the high density of iron metal particles. Presently automotive industries are applying this system. The application of this technology is wide such as, medical engineering, aerospace and polishing. There is a large range of research in MR fluid technology. MRF systems have to be designed more delicate, probably by introducing the uses of sensors and feedback technology i.e. closed loop systems. The life range of MR fluid devices in terms of the total energy dissipated from the equipment need to be increased. An improved MRF technology would make it the smart technology of future[28].

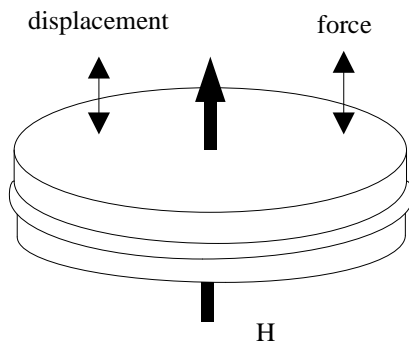


Figure 11 Squeeze mode

## 5. Mechanical model of MR damper

MR dampers are called semi-active elements of suspension systems whose damping specifications may be changed in real time based on the ability to change the viscosity of MR fluid as well its resistance to circulate by using of magnetic field. The benefit of MR fluid is that can permit the changes in the damping force by varying the current subjected to the damper. Thereby the hysteretic model characteristics of MR damper are based on current dependent and a function of excitation amplitude. It is important to analyze and model the MR damper with appropriate methods in order to predict its behavior in various magnetic fields or excitations. This approach becomes an important aspect because before the production of a MR damper it is significant to design

and choose the right parameters that will reach the behavior of the damper[29].

### 5.1 Bingham model

This Bingham model investigates and study plastic characteristic and the behavior of magneto-rheological and electro-rheological fluids. Bingham model ensure that a body remain as solid till a little yield stress is surpassed then after it shows a linear relationship between the stress and the rate of shear deformation[30]. Some researchers like Stanway et al. investigated a mechanical model based on the Bingham plastic model to exhibits the ER damping system. As it indicated in Figure 12 the model is based on a combination between coulomb friction and viscous dashpot. and is always utilized to analyze the characteristic or behavior of MR dampers[31].

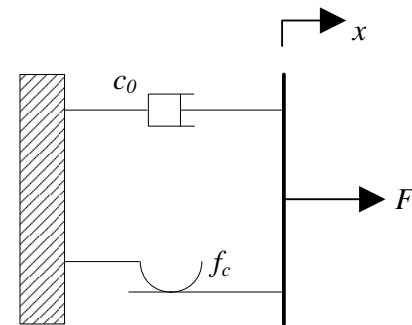


Figure 12 Bingham model

The force provided by mechanical element setting is coming from equilibrium concepts; it is expressed in the equation below:

$$F(t) = c_0 \dot{x} + f_c \text{sgn}(\dot{x}) + f_0 \quad (5)$$

Where,  $c_0$  denoted as constant of damping coefficient,  $\dot{x}$  defines the velocity of the external excitation  $f_c$  denoted the frictional force and  $f_0$  is the force offset related with the availability of an accumulator considering that this element has linear behavior and low stiffness. To investigate the flow of fluid, this mathematic expression model can be derived.

### 5.2 Bouc-Wen model

The hysteresis Bouc-Wen equation is among different models and the most used to study and simulate various method of expanding the damping system by changing the hysteresis. It has been invented by Bouc in 1971[32] and later developed by Wen in 1976[33] who has showed different methodologies of this model to show a wide kind of hysteretic patterns. According to this interesting behavior, the model was utilized to analyze different nonlinear hysteretic systems like MR damper and hysteretic isolators. However, MR dampers show a good typical behavior, the final hysteretic setting relies on certain particular specification features related to accumulator, damper geometry and so, on. So, the model should be suitable to have the real MR damper characteristic and several changes of the Bouc-wen model were designed and developed to simulate properly MR damper. Based on Bouc-Wen model different procedure to study the simulation the MR damper has been proposed; these models are: Classic or simple Bouc-Wen model;

- ① Advanced Bouc–Wen model or Spencer model;
- ② Shear model Bouc–Wen model
- ③ Bouc–Wen model for wide scale MR dampers;
- ④ Inverse Bouc–Wen model which is current dependant;
- ⑤ Current–frequency–amplitude-dependent;
- ⑥ Asymmetrical Bouc–Wen model.

As, it is indicated in the Figure13, the simple Bouc–Wen model is composed by three elements: a spring, a Bouc–Wen block and dashpot, mounted a parallel setting. In my project the simple model of Bouc–Wen will be used to simulate the MR damper behaviors. In this figure nonlinearity of the system is situated in the Bouc–Wen block, which is able to track the behavior of MR damper:

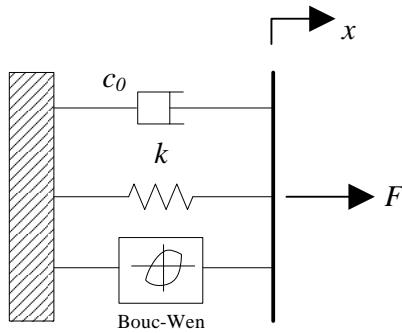


Figure 13 Bouc-wen model

The model investigates different characteristics of MR damper by comparing the performance of this model with other parametric models. Based to mechanical setting indicated in Figure13, the equation below express the damping force.

$$F(t) = c_0 \dot{x} + k(x - x_0) + \alpha z \quad (6)$$

Where  $c_0$  denoted the constant of viscous coefficient,  $k$  denoted the constant of stiffness coefficient and  $z$  is an evolutionary related variable with Bouc–Wen block and it ruled by:

$$\dot{z} = -\gamma |\dot{x}| z |z|^{n-1} - \beta \dot{x} |z|^n + A \dot{x} \quad (7)$$

$x_0$  is denoted the displacement at initial state, which permit the presence accumulator in the mechanism system. Constant  $c_0$ ,  $k$ ,  $\alpha$ ,  $\beta$ ,  $\gamma$ ,  $A$  and  $n$  are generally and the Bouc–Wen shape parameters or behaviors. They are the functions of the current subjected to the MR damper, frequency of vibration and amplitude. Nonlinear shape hysteretic curve can be controlled by varying the amounts of the Bouc–Wen block parameters permitting to monitor the smoothness in the state of transition between pre yield and post yield. Based to the ability to take the hysteretic element of the MR damper characteristics, the classic Bouc–Wen model is considered a best rational model of mathematical and numerical simulation compare to Bingham model. It is better in analysis of hysteric behavior. The use of Bouc–Wen hysteric model, lead on a good simulation of MR damper, test and implementation of its parties[35].

## 6. Semi-active vehicle suspension control strategies

Semi-active suspension is considered as the union of active and passive suspension. Since its invention, the damping force was adjusted by the variation of orifice area which leads on the change of flow resistance. MR damper is a kind of semi-active damper where the motion of MR fluid is adjusted by changing the value of current applied and thereby varies the level of damping force. As other control strategies of semi-active suspension dampers the MR damper is capable to provide a damping system even if the current become zero. The damper is able of generating huge control forces by changing behaviors like stiffness and damping coefficient through the variation of magnetic field and thus controls the response of large scaled structures like big buildings [36]. Control strategies of this system are to give a good stability handling and a smooth riding. Many studies and researches have been conducted to optimize the trade-off between road handling and ride comfort. These control strategies are categorized into techniques based on, nonlinear, linear and intelligent control methodologies.

### 6.1 Skyhook control

Skyhook control strategy is among the semi-active control strategies and the most commonly utilized that changes the damping force to imitate the damping effect of a passive damper in its optimal setting, mounted between the fixed reference and sprung mass (vehicle body) as showed in Figure 14 [58].

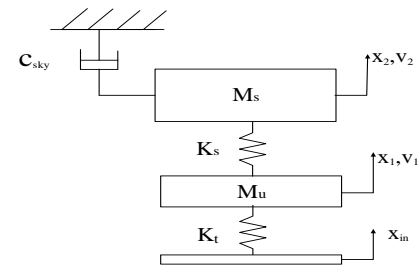


Figure14 skyhook control strategy

It is characteristically categorized as continuous control skyhook and on-off skyhook system. On-off Skyhook controller is always easier designed and well appropriated for the industrial era [37]. To implement the control strategies of On-off law equation below should be governed.

$$c_{sky} = \begin{cases} c_{max} & \text{if } V_r V_2 \geq 0 \\ c_{min} & \text{otherwise} \end{cases} \quad (8)$$

Where,  $V_2$  is defined the absolute velocity of the body, and  $V_r$  denoted as the relative velocity of the sprung mass (body) and unsprung mass (wheel) across the suspension. It is explained that if relative velocity of sprung mass (body) and the wheel have the similar direction, Hence, the maximum damping force must be subjected to mitigate the body acceleration. Meanwhile, if the two velocities (sprung velocity and unsprung velocity) are in the odd directions, the damping force must be set at low level to mitigate body acceleration. To achieve the skyhook controller strategy, absolute velocity of the body should be measured. Skyhook strategy

has been proven the optimization of ride behavior by minimizing vertical body acceleration. Skyhook control is good approach to minimize the vertical vehicle dynamic. But, according to its emphasis on optimizing a smooth ride, the road handling performance is very small. To prevent this issue ground-hook control strategy has been designed and proposed to optimize road handling abilities for controllable suspensions. The theory is based on the virtual damper which mounted on a fixed ground instead of sky which will give consideration to road holding ability to suspension mechanism[38].By comparing the skyhook semi active controller with passive suspension; models are simulated using a square bump as road profile, results show that the skyhook presents a great contribution to comfort of vehicle occupants as it is shown to the figure. 15 Where minimum body acceleration is indicating ride comfort

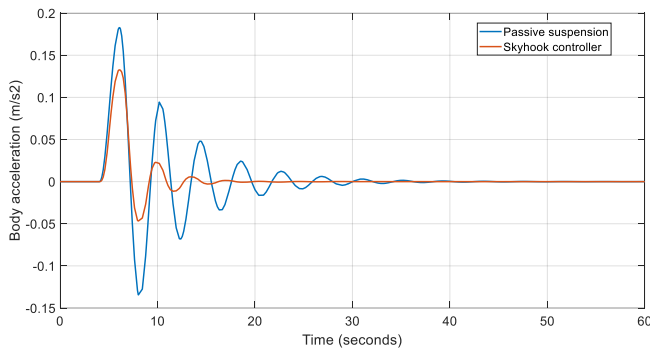


Fig: 15. Body acceleration comparison skyhook vs Passive

## 6.2. Ground hook control

As it is indicated in the Figure 16, the ground hook strategy is opposite from the skyhook model. In this model, the damper is mounted to the wheel rather than the body. Under the ground hook setting, the focus changes from the sprung-mass to the unsprung-mass [60].

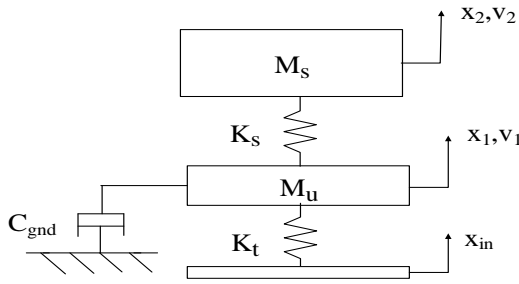


Figure 16. Ground hook strategies

As it indicated in this Figure16, in this setting the focus shifts from the sprung mass to unsprung mass. While skyhook work well in controlling the vertical body mass, ground hook is good in controlling the unsprung mass frequencies. The idea of ground hook is the same as the skyhook strategy, the difference is that it is ground hook control the wheel vibration [39].

$$\begin{cases} -V_1 V_2 \geq 0 \\ -V_1 V_2 < 0 \end{cases} \quad \begin{cases} F_{sa} = C_{gnd} V_1 \\ F_{sa} = 0 \end{cases} \quad (9)$$

## 6.3. Sliding control mode

Sliding control mode is a strong control strategy with various significant functionalities like insensitivity to linked behavior changes and disturbance isolation. Depending on its applications, sliding mode controller design showed a great potential in keeping the stability and optimization of in modeling and simulation the uncertainties. Sliding controller is constituted by of a nominal part, the same closed loop theorem, and additional conditions objected to face with uncertainty model. Reference model of Sliding Model Control is consist on forming a 'sliding surface' to track errors, the tracking should be equivalent all time[40].

Sliding-mode design has various functionalities that make it an advantageous option to remove nonlinearity tracking process, however; it presents a great importance in designing and modeling of uncertainties systems. It can be explained in many ways[41]. The first way is to consider that the system to process has two step procedures. Primo is the sliding surface which the desired state of the system. Secondly, a control system to conduct toward a sliding surface in the other word a system to track the sliding surface system, then after switching on that surface. In theory sliding mode will effectively approach the control purpose, the cause of phase surface[42]. The control action design can be pretended according on various strategies, a straightforward one which is based on determining a Lyapunov-like condition that make the sliding surface to be an attractive region for the state vector trajectories[43].

Reference: the idea of reference is based on development of control algorithm necessary to force the plant to virtual dynamic model. So, to consider a reference model is very useful. In model reference control for instance a set point regulation problem is changed into a tracking problem by immersing a reference model to filter the given configuration point value and to provide output which is variable with time as virtual response of tracking control mechanism[42].

Based to the sliding mode control (SMC) regulation, as it is indicated on the Figure17a and b, an asymptotically fixed sliding mode state can be derived from dynamic errors between the MR quarter suspension of vehicle dynamic system and the transformed skyhook reference model approach[44].

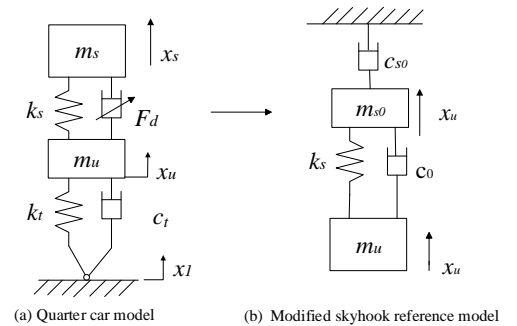


Figure 17. Sliding control mode

According to skyhook reference model wheel (unsprung mass), the displacement  $x_u$  of MR quarter-vehicle suspension can be directly utilized as road variation input of the skyhook reference model system, because the real tire stiffness is typically 5 times of the suspension spring stiffness. Based on hypothesis

above the dynamic equation of skyhook reference is expressed as[45]:

$$m_{s0}\ddot{x}_{s0} + c_0(\dot{x}_{s0} - \dot{x}_u) + c_{s0}\dot{x}_{s0} + k_s(x_{s0} - x_u) = 0 \quad (10)$$

Where  $m_{s0}$  denoted as reference model sprung mass, which is equivalent to unloaded sprung mass of the semi-active quarter-vehicle suspension,  $c_{s0}$  denotes skyhook damping constant, and  $x_{s0}$  are defined as body mass displacement of reference model,  $k_s$  and  $c_0$  defined as spring stiffness of the passive quarter-vehicle suspension and damping constant coefficient, respectively. The sliding mode  $s$  of MR quarter-vehicle system is expressed as this equation below:

$$s = \dot{e}_s(t) + \lambda e_s(t) \quad (11)$$

where  $\lambda > 0$  defines the convergence rate of sliding mode surface,  $e_s(t) = x_s(t) - x_{s0}(t)$  defines the errors between body mass displacement of MR suspension quarter car dynamic and dynamic system of skyhook reference and  $e(t)$  become 0 if  $t$  tends to infinite. Moreover, Lyapunov function is expressed as  $V = s^2/2$ . To make sure that the system state asymptotically adjusts to the sliding surface mode, it is denoted that

$$\dot{V} = \dot{s}s \leq -\phi|s| \quad (12)$$

Where  $\phi$ , is denoted as positive constant. If the effect of gravity is neglected, the equation (13), is gotten

$$\begin{cases} m_s\ddot{x}_s + k_s(x_s - x_u) + F_d - m_s g = 0 \\ m_u\ddot{x}_u + F_t - k_s(x_s - x_u) - F_d - m_u g = 0 \end{cases} \quad (13)$$

We get

$$\ddot{x}_s = [-k_s(x_s - x_u) - F_d]/m_s \quad (14)$$

By combining Eq. (13) and Eq. (14), equation (15) is obtained

$$\dot{s} = [-k_s(x_s - x_u) - F_d]/m_s - \ddot{x}_{s0} + \lambda \dot{e}_s(t) \quad (15)$$

Base on the stability functionality of sliding mode control strategy,  $\dot{s} = 0$ , the virtual control damping force  $F_{d0}$  of MR quarter car suspension can be derived from Eq. (15)

$$F_{d0} = -k_s(x_s - x_u) - m_{s0}\ddot{x}_{s0} + m_{s0}\lambda \dot{e}_s \quad (16)$$

To guarantee that yielded damping force  $F_d$  of the MR damper can quickly track its virtual control damping forces  $F_{d0}$ , by using switch control law, the damping control force is denoted

$$F_c = F_{d0} - K \cdot \text{sgn}(s) \quad (17)$$

Where  $K$  defines the constant gain of SMC which will be derived later and  $\text{sgn}(s)$  is limit function which vary between -1 and 1, If  $s \leq 0$  and  $s > 0$ , respectively. Based on  $V = \dot{s}s$ ,  $F_c$  to replace  $F_d$  in Eq. (15) integrate it into  $V = \dot{s}s$  and therefore, obtain  $\dot{V}$  is gotten

$$\dot{V} = (-k_s x_s/m_s + k_s x_u/m_s - F_c/m_s - \ddot{x}_{s0} + \lambda \dot{e}_s)s \quad (18)$$

Combining Eq. (16) and (18)  $\dot{V}$ , is obtained

$$\dot{V} = [(1/m_s - 1/m_{s0})(-k_s x_s + k_s x_u - F_{d0}) + K \cdot \text{sgn}(s)/m_s] \quad (19)$$

Based on the Lyapunov stability of Sliding control mode, Eq. (19) is integrated into Eq. (14) and obtain

$$\left[ \begin{aligned} & \left( \frac{1}{m_s} - \frac{1}{m_{s0}} \right) (-k_s x_s + k_s x_u - F_{d0}) \\ & + K \cdot \text{sgn}(s)/m_s \end{aligned} \right] s \leq -\phi|s| \quad (20)$$

As considering  $s = s \cdot \text{sgn}(s)$ , Hence Eq. (20) is governed as

$$\left[ \begin{aligned} & \left( \frac{1}{m_s} - \frac{1}{m_{s0}} \right) (-k_s x_s + k_s x_u - F_{d0}) \\ & + K \cdot \text{sgn}(s)/m_s \end{aligned} \right] s \leq -\phi \cdot s \cdot \text{sgn}(s) \quad (21)$$

for  $s \geq 0$ , Eq. (21) can be simplified as

$$K \leq -m_s \phi + (1 - m_s/m_{s0})(k_s x_s - k_s x_u + F_{d0}) \quad (22)$$

for  $s < 0$ , Eq. (21) can be simplified as

$$K \leq -m_s \phi + (1 - m_s/m_{s0})(-k_s x_s + k_s x_u - F_{d0}) \quad (23)$$

If the real load of vehicle is considered as usually variable  $\eta$  is expressed as the change rate of vehicle body mass (sprung mass)  $m_s$  to its unloaded sprung mass  $m_{s0}$ , in the other word  $s = m_s/m_{s0} \geq 1$ . By using Eq. (22) and (23),  $K$  of sliding control mode is obtained

$$K = -m_{s0}\eta\phi - (\eta - 1)(|F_{d0}| + k_s|x_s| + k_s|x_u|) \quad (24)$$

Therefore, the saturation function  $\text{sat}(s)$  is used to replace the sign function  $\text{sgn}(s)$  in Eq. (20) for limiting chattering frequency which may happen in the system, and takes  $s/\varepsilon$  and  $\text{sgn}(s)$  when  $s \leq \varepsilon$  and  $s > \varepsilon$ , accordingly. Eq. (20) can be shown as

$$F_c = F_{d0} - K \text{sat}(s) \quad (25)$$

Where  $\varepsilon$  denotes positive constant. Fig18, indicates the ride comfort between passive suspension and semi active suspension in sliding mode control strategy. The improvement is more than 35% compare to passive suspension.

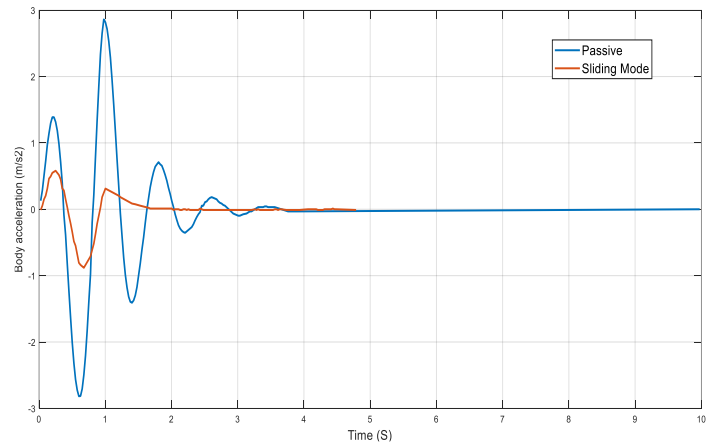


Figure18. Body acceleration comparison of sliding mode and passive

### 3.4 Fuzzy logic control strategy

Fuzzy logic control strategy is a type of many values of logic. In many applications of control of nonlinear systems, this approach developed by mathematicians has been appreciated and successful used. Since the last decades the implementation of fuzzy logic has been growth due to the various researches which showed its potential on controlling the nonlinearities systems,

Fuzzy logic has been invented by Zadeh [46] in 1965, ten years after its invention, Mamdani [47] developed and showed the utility of Fuzzy Logic Control (FLC) in modeling and control of small steam engine's suspension to replace the traditional suspension of damper and spring of vehicle by active suspension. The result of Fuzzy logic model demonstrated a big improvement of riding comfort and road handling in various conditions [1]. Presently fuzzy logic is applied in many areas such as dynamic process, washing machine and in automation industries. The theory of fuzzy control is based on operations rules that are human can read and represent human's knowledge about how to control and monitoring the process. The rules are defined in terms of fuzzy involvement. It is composed by three main elements namely input, process output and a reference signal. For the suspension vertical dynamics application, input is the suspension damping control and process output is a rate of velocities between sprung and unsprung masses [49].

Generally, input is supplied to Fuzzifier which changes crisp data input into fuzzified data which is then analyzed processed in Fuzzy inference function block using fuzzy rules. This fuzzy output is then converted to crisp output using Defuzzifier. Fig 19 indicates schematic of Fuzzy control methodology which is the flowchart of control strategy. Fuzzy logic approach control has many features that make it attractive for semi-active suspension. There are many nonlinear devices like tires shock absorbers springs and many rubber components. All these non-linearities can be made linear having significant impact on the precision of model.

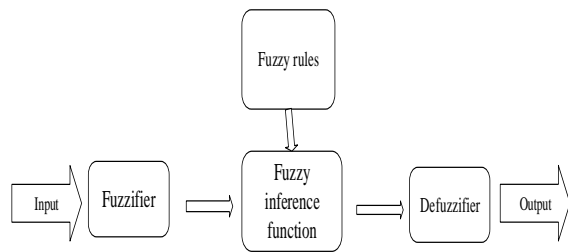


Figure 19 fuzzy control methodology

Fuzzy logic algorithm controls many loops variation in various non-linear systems. It has two inputs, namely suspension deflection and suspension velocity. The controller calculates those inputs and generate the desired damping force based on inference rules subjected on it. These control systems embed the human as thinking through the application of fuzzy configurations and linguistic variables related by a configuration of IF-THEN fuzzy rules. The results show figure 20 and 21 that fuzzy logic can dramatically reduce the tradeoff between road handling and ride comfort. However, it can't completely mitigate this odd.

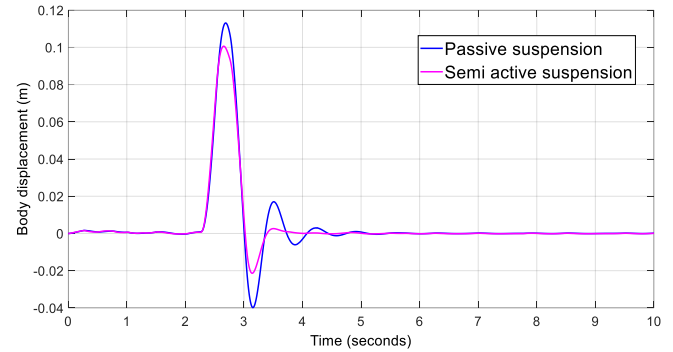


Figure 20 Body acceleration comparison of semi active and passive

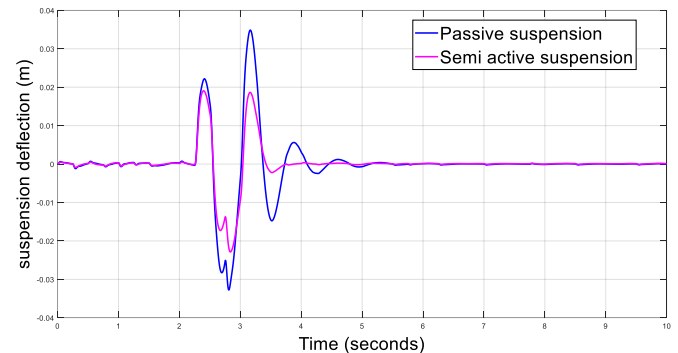


Figure 21 Suspension deflection comparison of semi active and passive

### 3.5 Linear Quadratic Gaussian

Linear-Quadratic-Gaussian (LQG) control is a robust strategy which is based on an advanced state-space algorithm to design optimal dynamic regulators. It is based on noise measurement of the process and requires a state-space model of the plant [50]. This control algorithm was less used in control of semi-active vehicle suspension based on MR dampers, thus it was largely applied in control and monitoring of active suspension to mitigate the vibrations. To examine the effectiveness of semi active suspension controller, the LQG control strategy is utilized to calculate the desired damping force  $f_d$  necessary to generate a smooth ride and comfort. LQG is composed by Kalman filter gain  $K_f$  and of an optimal state-feedback, gain  $K$  named Linear-Quadratic-Regulator (LQR). The optimal control has been designed to find a controller which may perform better. The optimal controller LQR for the vehicle suspension control is the most utilized in background of various researches of vehicle suspension control. The strength of LQR method is that in using it the factors of the optimization index can be weighted based to the designer's wish or other constraints. The LQR approach is utilized to optimize the road holding and the drive comfort for vehicle suspension. LQR control approach remain better in control of linear active suspension mechanism [50].

In modeling and control of linear active suspension, the equation below denoted the system

$$\dot{x}(t) = Ax(t) + Bu(t) + f(t) \quad (26)$$

A state variable of feedback regulator of the system is considered as

$$u(t) = -Kx(t) \quad (27)$$

$K$  denotes the state feedback constant gain matrix (controller). Hence, a new system is obtained as

$$\dot{x}(t) = (A - BK)x(t) + f(t) \quad (28)$$

The perform procedure serves on defining input of control  $U$ , which reduce the performance index.  $J$  is performance index show the optimization required behavior as well as the controller input mitigation. The LQR optimal controller of provided system is defined as controller design which reduces the performance index below.

$$J = \int_0^{\infty} (X(t)^T Q X(t) + u(t)^T R u(t)) dt \quad (29)$$

Where  $u$  defines state input,  $R$  and  $Q$  denoted the positive weighting matrices.

Controller gain  $K$  is defined by:

$$K = R^{-1} B^T P \quad (30)$$

Where  $P$ , is denoted as the matrix which is studied as solution of the Algebraic Riccati Equation (ARE) as follow as

$$PA + A^T P - PBR^{-1}B^T P + Q = 0 \quad (31)$$

To evaluate the Kalman filter gain  $K_f$ , the solution of the following Algebraic Riccati Equation is obtained as  $S$

$$AS + SA^T + G W G^T - S C^T V^{-1} C S + Q = 0 \quad (32)$$

Then, calculating  $K_f$  like that,

$$K_f = S C^T V^{-1} \quad (33)$$

The Kalman filter for the LQR controller becomes

$$\dot{\hat{x}}(t) = A \hat{x}(t) + B u(t) + K_f [y(t) - C \hat{x}(t) - D u(t)] \quad (34)$$

The equation below is considered as system

$$\dot{x} = Ax + B f_a + G w \quad (35)$$

Where  $w(t)$  is defines as a fixed Gaussian white noise process. Then, system (29) is denotes as linear system applied to a Gaussian noise. By solving stochastic equation of optimal control issue, and measuring the feedback system the equation (36) is gotten.

$$Y = Cx(t) + Du(t) + v(t) \quad (36)$$

Where  $v(t)$  defines a random signal which defines the measurement noise. The plant and measurement noise are remained both white noise and simultaneous. As it is shown below,

$$E\{ww^t\} = W, \quad E\{vv^t\} = V, \quad E\{wv^t\} = 0 \quad (37)$$

The LQR gain  $K$  defined above are utilized with a Kalman filter gain  $K_f$  to get state estimator. It was determined that the body acceleration  $\ddot{x}_b$  and the wheel acceleration  $\ddot{x}_w$  measurements are available in addition to the suspension working space  $x$ . In other words, the output vector is assumed to be  $Y = [x_b - x_w, \ddot{x}_b, \ddot{x}_w]$ . The measured parameters are utilized to optimize LQG controller of suspension because the cost accelerometers are relatively low, and LQ was not robust enough to perform a better control.

#### 4. Conclusion

Semi active control strategies based on Magneto-rheological damper are studied and reviewed in details, through the Bouc-wen model for MR damper, the simulation was conducted based on quarter car model passing on trapezoidal bump, the control improvements are just subjective and controllers should act with a compromise between odds behaviors which is ride comfort and vehicle stability. Simulation results for various control strategies like skyhook, groundhook, slide mode controller, fuzzy logic and Linear quadratic Gaussian for Bouc-Wen magneto-rheological damper, showed that the semi active suspension acts well on the reduction of compromise between comfort and stability, however it can't mitigate this compromise at 100% this odd. The authors suggest that combining more than two control strategies could dramatically reduce this compromise issue between comfort and vehicle stability. For the future scope the use of artificial neural networks in control strategy could bring lower odd between ride comfort and road handling.

#### Conflict of Interest Statement

The authors declare that there is no conflict of interest.

#### CRedit Author Statement

**Musabyimana Josee:** Supervision, Methodology, article editing, **Kazima Sosthene:**, Writing original draft and revision, **Turabimana Pacifique:** Writing original draft and revision

#### References

1. Aly, A. A., & Salem, F. A. (2013). Vehicle suspension systems control: a review. *International journal of control, automation and systems*, 2(2), 46-54.
2. Rao, T. R. M. R., Mohan, R., Rao, G. V., Rao, K. S., & Purushottam, A. (2010). Analysis of passive and semi active controlled suspension systems for ride comfort in an omnibus passing over a speed bump. *International Journal of Research and Reviews in Applied Sciences*, 5(1).
3. Ahmadian, M. (2014). Integrating electromechanical systems in commercial vehicles for improved handling, stability, and comfort. *SAE International Journal of Commercial Vehicles*, 7(2014-01-2408), 535-587.
4. Fialho, I., & Balas, G. J. (2002). Road adaptive active suspension design using linear parameter-varying gain-scheduling. *IEEE transactions on control systems technology*, 10(1), 43-54.
5. Mulla, A. A., & Unaune, D. R. (2013, March). Active suspensions future trend of automotive suspensions. In *International Conference on Emerging Trends in Technology&Its Applications, ICETTA*.
6. Gysen, B. L., Paulides, J. J., Janssen, J. L., & Lomonova, E. A. (2009). Active electromagnetic suspension system for improved vehicle dynamics. *IEEE Transactions on Vehicular Technology*, 59(3), 1156-1163.
7. Rashid, M. M., Hussain, M. A., Rahim, A. N., & Momoh, M. J. E. (2007). Development of a semi-active car suspension control system using magneto-rheological damper model.
8. Félix-Herrán, L. C., de Jesús Rodríguez-Ortiz, J., Soto, R., & Ramírez-Mendoza, R. (2008, October). Modeling and control for a

- semi-active suspension with a magnetorheological damper including the actuator dynamics. In 2008 Electronics, Robotics and Automotive Mechanics Conference (CERMA'08) (pp. 338-343). IEEE.
9. Rabinow, J. (1948). The magnetic fluid clutch. *Electrical Engineering*, 67(12), 1167-1167.
  10. Kim, J. H., Kang, B. W., Park, K. M., Choi, S. B., & Kim, K. S. (2002). MR inserts for shock wave reduction in warship structures. *Journal of intelligent material systems and structures*, 13(10), 661-665.
  11. Seong, M. S., Choi, S. B., & Sung, K. G. (2011). Control strategies for vehicle suspension system featuring magnetorheological (MR) damper. *Vibration Analysis and Control: New Trends and Developments*; InTech: London, UK, 97-114.
  12. Sosthene, K., Josee, M., & Xiong, H. U. Í. (2018). Fuzzy logic controller for semi active suspension based on magneto-rheological damper. *International Journal of Automotive Engineering and Technologies*, 7(1), 38-47.
  13. Carlson, J. D., Catanzarite, D. M., & St. Clair, K. A. (1996). Commercial magneto-rheological fluid devices. *International Journal of Modern Physics B*, 10(23n24), 2857-2865.
  14. Ashtiani, M., Hashemabadi, S. H., & Ghaffari, A. (2015). A review on the magnetorheological fluid preparation and stabilization. *Journal of magnetism and Magnetic Materials*, 374, 716-730.
  15. Muhammad, A., Yao, X. L., & Deng, Z. C. (2006). Review of magnetorheological (MR) fluids and its applications in vibration control. *Journal of Marine Science and Application*, 5(3), 17-29.
  16. Jolly, M. R., Bender, J. W., & Carlson, J. D. (1999). Properties and applications of commercial magnetorheological fluids. *Journal of intelligent material systems and structures*, 10(1), 5-13.
  17. Gołdasz, J., & Sapiński, B. (2015). *Insight into magnetorheological shock absorbers* (pp. 1-224). Switzerland: Springer International Publishing.
  18. Goncalves, F. D., Koo, J. H., & Ahmadian, M. (2006). A review of the state of the art in magnetorheological fluid technologies--Part I: MR fluid and MR fluid models. *The Shock and Vibration Digest*, 38(3), 203-220.
  19. Kciuk, M., & Turczyn, R. (2006). Properties and application of magnetorheological fluids. *Journal of Achievements in Materials and Manufacturing Engineering*, 18(1-2), 127-130.
  20. Hajalilou, A., Mazlan, S. A., Lavvafi, H., & Shamel, K. (2016). Magnetorheological fluid applications. In *Field Responsive Fluids as Smart Materials* (pp. 67-81). Springer, Singapore.
  21. Yao, G. Z., Yap, F. F., Chen, G., Li, W., & Yeo, S. H. (2002). MR damper and its application for semi-active control of vehicle suspension system. *Mechatronics*, 12(7), 963-973.
  22. Olabi, A. G., & Grunwald, A. (2007). Design and application of magneto-rheological fluid. *Materials & design*, 28(10), 2658-2664.
  23. Gudmundsson, K. H., Jonsdottir, F., & Thorsteinsson, F. (2010). A geometrical optimization of a magneto-rheological rotary brake in a prosthetic knee. *Smart materials and Structures*, 19(3), 035023.
  24. Baranwal, D., & Deshmukh, T. S. (2012). MR-fluid technology and its application-a review. *International Journal of Emerging Technology and Advanced Engineering*, 2(12), 563-569.
  25. De Vicente, J., Klingenberg, D. J., & Hidalgo-Alvarez, R. (2011). Magnetorheological fluids: a review. *Soft matter*, 7(8), 3701-3710.
  26. Dyke, S. J., Spencer Jr, B. F., Sain, M. K., & Carlson, J. D. (1996). Modeling and control of magnetorheological dampers for seismic response reduction. *Smart materials and structures*, 5(5), 565.
  27. Carlson, J. D., & Jolly, M. R. (2000). MR fluid, foam and elastomer devices. *mechatronics*, 10(4-5), 555-569.
  28. Gong, X., Ruan, X., Xuan, S., Yan, Q., & Deng, H. (2014). Magnetorheological damper working in squeeze mode. *Advances in Mechanical Engineering*, 6, 410158.
  29. Braz-César, M. T., & Barros, R. (2012). Properties and numerical modeling of MR dampers. *Proceedings of the ICEM15-Experimental Mechanics: New trends and Perspectives*, 1199-1200.
  30. Stanway, R. S. J. L., Sproston, J. L., & Stevens, N. G. (1987). Non-linear modelling of an electro-rheological vibration damper. *Journal of Electrostatics*, 20(2), 167-184.
  31. Guo, S., Yang, S., & Pan, C. (2006). Dynamic modeling of magnetorheological damper behaviors. *Journal of Intelligent material systems and structures*, 17(1), 3-14.
  32. Bouc, R. (1971). A mathematical model for hysteresis. *Acta Acustica united with Acustica*, 24(1), 16-25.
  33. Wen, Y. K. (1976). Method for random vibration of hysteretic systems. *Journal of the engineering mechanics division*, 102(2), 249-263.
  34. Spencer Jr, B., Dyke, S. J., Sain, M. K., & Carlson, J. (1997). Phenomenological model for magnetorheological dampers. *Journal of engineering mechanics*, 123(3), 230-238.
  35. Sosthene, K., JOSEE, M., & EMMANUEL, K. (2018). Vehicle ride comfort optimization based on Magneto-rheological damper. *International Journal of Automotive Science And Technology*, 2(4), 1-8.
  36. Y. Iskandarani and H. Karimi, "Hysteresis modeling for the rotational magnetorheological damper," in *Proceedings of the 4th WSEAS International Conference on Energy and Development-environment-biomedicine*, 2011, pp. 479-485.
  37. Zhang, H., Winner, H., & Li, W. (2009). Comparison between skyhook and minimax control strategies for semi-active suspension system. *World Academy of Science, Engineering and Technology*, 55(5), 618-621.
  38. Choi, S. B., Seong, M. S., & Kim, K. S. (2009). Vibration control of an electrorheological fluid-based suspension system with an energy regenerative mechanism. *Proceedings of the Institution of Mechanical Engineers, Part D: Journal of Automobile Engineering*, 223(4), 459-469.
  39. Mulla, A., Jalwadi, S., & Unaune, D. (2014). Performance analysis of skyhook, groundhook and hybrid control strategies on semiactive suspension system. *International Journal of Current Engineering and Technology*, 3, 265-269.
  40. Assadsangabi, B., Eghtesad, M., Daneshmand, F., & Vahdati, N. (2009). Hybrid sliding mode control of semi-active suspension systems. *Smart Materials and Structures*, 18(12), 125027.
  41. Yokoyama, M., Hedrick, J. K., & Toyama, S. (2001, June). A model following sliding mode controller for semi-active suspension systems with MR dampers. In *Proceedings of the 2001 American Control Conference*. (Cat. No. 01CH37148) (Vol. 4, pp. 2652-2657). IEEE.
  42. Singla, U. L., & Singh, S. P. (2004). Semi-active control of automotive vehicle suspension system using magnetorheological damper-a review.
  43. Perruquetti, W., & Barbot, J. P. (2002). *Sliding mode control in engineering*. CRC press.
  44. Zhang, H., Wang, E., Zhang, N., Min, F., Subash, R., & Su, C. (2015).

- Semi-active sliding mode control of vehicle suspension with magneto-rheological damper. *Chinese Journal of Mechanical Engineering*, 28(1), 63-75.
45. J. Liu and X. Wang, *Advanced sliding mode control for mechanical systems: design, analysis and MATLAB simulation*: Springer Science & Business Media, 2012.
  46. L. A. Zadeh, "Fuzzy sets," *Information and control*, vol. 8, pp. 338-353, 1965.
  47. Mamdani, E. H. (1977). Application of fuzzy logic to approximate reasoning using linguistic synthesis. *IEEE transactions on computers*, 26(12), 1182-1191.
  48. Rasal, S., Jaganmohan, J., Agashe, S., & Wani, K. P. (2016). Implementation of fuzzy logic control in semiactive suspension for a vehicle using MATLAB SIMULINK (No. 2016-28-0035). SAE Technical Paper.
  49. Speyer, J. (1979). Computation and transmission requirements for a decentralized linear-quadratic-Gaussian control problem. *IEEE Transactions on Automatic Control*, 24(2), 266-269.
  50. ElMadany, M. M., & Abduljabbar, Z. S. (1999). Linear quadratic Gaussian control of a quarter-car suspension. *Vehicle System Dynamics*, 32(6), 479-497.



## Modeling of an Electric Bus Using MATLAB/Simulink and Determining Cost Saving for a Realistic City Bus Line Driving Cycle

Oğuzhan Karakaş<sup>1\*</sup>, Umut Buğra Şeker<sup>1</sup>, Hamit Solmaz<sup>1</sup>

<sup>1</sup> Automotive Engineering Department, Faculty of Technology, Gazi University, Ankara, 06500, Turkey

### ABSTRACT

Since the discovery of the internal combustion engine in the 19th century, petroleum and its derivatives are used in most of the vehicles which is using for transportation on the Earth. The environmental pollution caused by petroleum, the largest energy source used worldwide for over 100 years, the danger of depletion of the reserves and the increase in the price of the barrels have encouraged scientists to develop cleaner and more efficient clean energy sources. Electric vehicles, according to conventional vehicles with internal combustion engine; has advantages such as noiselessness, high efficiency, low fuel consumption and low maintenance costs. In this paper, city buses, which are frequently used worldwide and in our country, have been handled to find out what advantages will be provided when the electric motor is switched to use, to calculate what the costs will be and to show how this change can be applied were carried out. Considering the concepts such as emission, fuel-maintenance costs and noise pollution caused by the use of city buses, a 12-meter bus is modeled in MATLAB/Simulink environment for full electrical urban use. The "HV SUMO HD HV3500" model of TM4 was chosen as the electric motor for the modeled vehicle. For the simulation process, driving cycle has generated in 541 Eryaman-Kızılay line which is one of the urban bus lines and simulations were applied on this cycle. As a result of the simulations performed, total range, remaining range and energy consumptions were examined and comparisons were made for the different weights of the bus. The effects of regenerative braking on battery status were investigated. Simulations were repeated by changing the resistance values and the effects on battery usage and range were investigated.

**Keywords:** electric engine, modelling of an electric vehicle, simulation, Matlab/Simulink, NEDC, electric vehicle, electrical bus

#### History

Received: 16.04.2021

Accepted: 24.06.2021

#### Author Contacts

\*Corresponding Author

e-mail addresses : [oguzkarakas08@gmail.com](mailto:oguzkarakas08@gmail.com), [sekerumutbugra@gmail.com](mailto:sekerumutbugra@gmail.com), [hsolmaz@gazi.edu.tr](mailto:hsolmaz@gazi.edu.tr)

Orcid numbers : 0000-0001-9028-1579, 0000-0001-5020-5061, 0000-0003-0689-6824

<http://dx.doi.org/10.29228/eng.pers.51422>

### 1. Introduction

Electric vehicles have advantages compared to conventional vehicles with internal combustion engine; such as silence, high efficiency, low fuel consumption and low maintenance costs [1,2,3].

In this study, city buses that are frequently used in our country are discussed. It was made to learn how to gain advantage in the use of electric motors in buses, to calculate what the costs would be, and to examine how applicable this change would be. Considering the concepts such as emissions, fuel-maintenance costs and noise pollution caused by the use of city buses, a 12-meter fully electrical bus for urban use was modeled in MATLAB / Simulink.

Many researchers have been studied on electric vehicle modeling to examine motor choices and the advantages of electric vehicles. S. Çağlar Başlamış, Bayramcan İnce, Mertcan Koçak, Hasan H. Saygılı (2016) studied the fuel consumption and saving

methods of a hybrid electric city bus by using Istanbul and Konya driving cycles. In their study, they modeled the system algorithm according to the torque demand of the engine by using two different strategies, which they called the limited thermostat strategy and the maximum battery charge strategy [23]. Vyas Singh Chauhan (2017) modeled 10 different electric, hybrid electric and fuel cell vehicles on Matlab / Simulink in order to observe the data of vehicles known in the market under different driving conditions and analyzed these vehicles for 7 different driving cycles [16]. X. D. Xue, K. W. E. Cheng, N. C. Cheung (2008) aimed to find the most suitable engine for electric vehicles in their thesis study. They made comparisons between electric motors on criteria such as efficiency, weight, cost, cooling, maximum speed and fault tolerance. As a result of these comparisons, they determined the "Permanent Magnet Synchronous Motor" as the most efficient motor [9]. Ekrem Başer

(2016) made a comparison of asynchronous motor and permanent magnet synchronous motor in urban use in his master's thesis. Başer, who modeled both engines on Matlab/Simulink in his study, examined which engine was more efficient under equal speed conditions. Comparison of motors was made on efficiency, cost, performance and energy consumption parameters [11].

According to the data obtained from the EGO organization to which Ankara city buses are affiliated; In January 2018, a total of 8454114 km was traveled and 5506700 liters of natural gas and 768520 liters of diesel were used in the same month. In the same month, a total of 17611336 people used EGO's inner city bus lines. This number of passengers is just one of the proofs showing the place of city buses in our lives.

In January 2018, 1 liter of diesel was sold for 1,36 USD and 1 m<sup>3</sup> of CNG for 0,89 USD. Based on these data, January EGO buses used a total of 1.054.013,61 USD of fuel. During January, 34739 vehicles were put into service, on average, 1121 vehicles served the public on the streets of Ankara on a daily basis [4].

In order to provide real driving conditions in modeling, a test drive cycle has been created on the line 541 of the EGO organization Eryaman-Kızılay of Ankara Metropolitan Municipality.

In this study; Electric motor, drivetrain and bus body data from various companies were used. A transfer function has been created for the powertrain of the electric vehicle. By this way, the angular velocity of the electric motor that drives the vehicle has been calculated. As a result of this calculation, an electric motor model was created by using angular velocity.

A model was created for the resistance forces affecting the vehicle in dynamic driving conditions and added to the main model. By creating a battery and energy consumption model, measurements such as the amount of energy consumed by the vehicle during the driving cycle, battery capacity and remaining range data were obtained. In addition, a brake model was added to the Simulink model, allowing the energy gained by regenerative braking to be used in battery charging.

The "SUMO HD HV3500" model of DANA TM4 company was chosen as the electrical motor for the modeled bus. The selected electrical motor can produce maximum 3500 Nm of torque and 350 kW of power. For the Drivetrain, ZF Company's "Rear Axle System AV 133" model was selected. While choosing the reference vehicle information, the buses currently produced by Mercedes-Benz, Güleryüz and BMC companies were used.

### 1.1 Electrical Vehicles

Electric vehicles contain a main power source and auxiliary power sources, motor inverter and electric motor. The motor inverter is responsible for the parameters such as the conversion and control of the electrical energy stored in the batteries of full electric vehicles. The motor inverter provides this control according to the accelerator pedal position, and provides adjustment of the power to the electric motor. Although it varies according to the motor and inverter used in vehicle, some motor inverters can convert the DC taken from the battery to AC [5,6].

The electrical motors provides the main power that necessary to drive from the batteries; In addition to this, auxiliary power supplies are used for sudden acceleration and loads. These auxiliary sources are super capacitors and secondary batteries. Their purpose is to

power the electric motor under peak operating conditions for short periods [7]. The fully electrical vehicle scheme is shown in Figure 1.

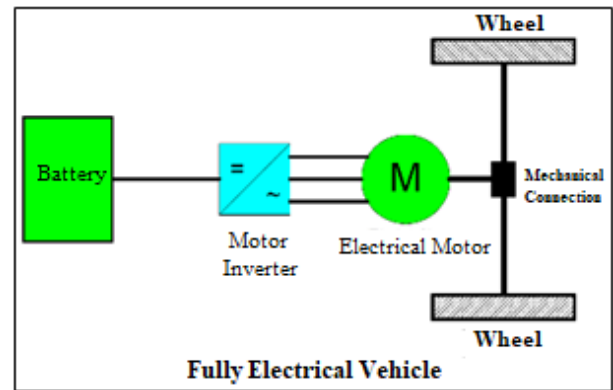


Figure 1. Fully Electrical Vehicle

Fully electrical vehicles are more efficient than conventional internal combustion engine vehicles. In a vehicle with an electric motor and battery, %46 of the energy taken from the plug is converted into usable work. On the other hand, only 18-25% of the energy that a conventional internal combustion engine generates from fuel is used [8].

## 2. Material-Method

### 2.1 Electric motor model

In order to meet the required values, the electric motor "SUMO HD HV3500" from DANA TM4 was selected for the modelled vehicle [9,10]. This motor is designed for heavy duty vehicles and 6 - 18 meters buses [11]. The features of the electric motor are given in Table 1 and Figure 2.

Table 1. Features of The Electric Motor [12]

Features	SUMO HD HV3500
Used Inverter	TM4 Reflex CO300-HV
Maximum Power (kW)	350
Continuous Power (kW)	260
RPM Range (rpm)	0 – 3400
Peak Torque (Nm)	3500
Continuous Torque (Nm)	1830
Number of Phase	9
Mass (kg)	340+36

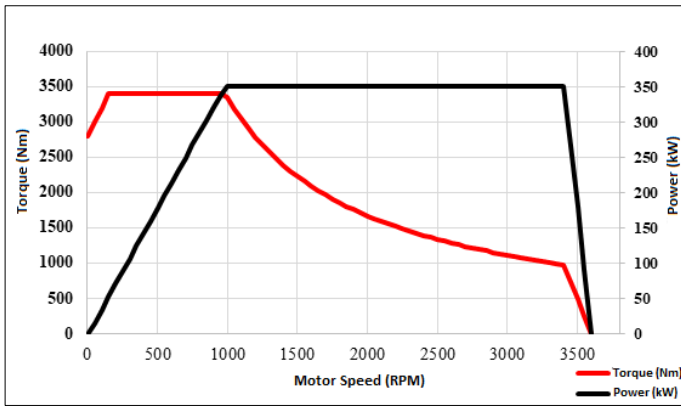


Figure 2. Electric Motor Performance Curve [4]

Simulink model of the electric motor is shown in Figure 3. In this model, the revolution of the electric motor is applied, the maximum torque value produced by the motor at that revolution is calculated. The torque value calculated here will be included in the dynamic model with the accelerator pedal control. Since the efficiency map of the electric motor could not be reached, the electric motors in the market were examined and 90% efficiency value was used.

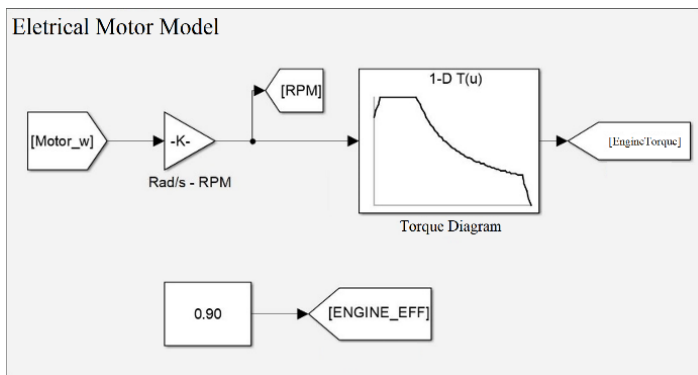


Figure 3. Electric Motor Simulink Model

### 2.2 Model of total resistance torque affecting the vehicle

Vehicles are exposed to some resistance forces while in motion, and these resistances must be overcome by engine power. While the reduction of these resistances causes a decrease in fuel consumption in vehicles with conventional internal combustion engines, decreasing the resistances causes energy savings in electric motor vehicles and increases the range. For this reason, it is very important to reduce resistances in electrical vehicles.

There are four different resistance forces acting on the vehicle. These are called aerodynamic resistance, rolling resistance, hill resistance and acceleration resistance. Real working conditions are created by applying these resistances that the vehicle is exposed to while driving. These resistances are shown in Figure 4.

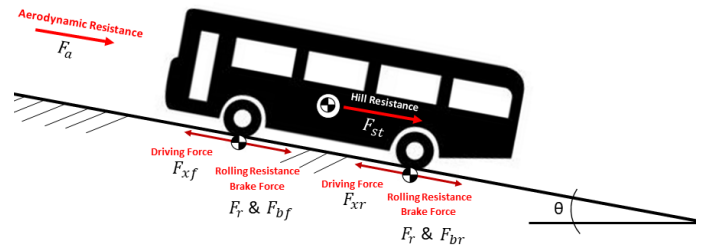


Figure 4. Resistance Forces Acting on Vehicle

#### 2.2.1 Aerodynamic Resistance

The aerodynamic resistance force is calculated by the following equation [13].

$$F_a = 0.5\rho C_d A_f (V + V_0)^2 \tag{1}$$

In the last equation;

- $C_d$ : Aerodynamic drag coefficient,
- $A_f$ : Front projection area of the vehicle,  $m^2$
- $V$ : Vehicle speed, m/s
- $V_0$ : Wind speed opposite to the direction of movement, m/s
- $\rho$ : Air density,  $\frac{kg}{m^3}$

Aerodynamic drag force model is given in Figure 5.

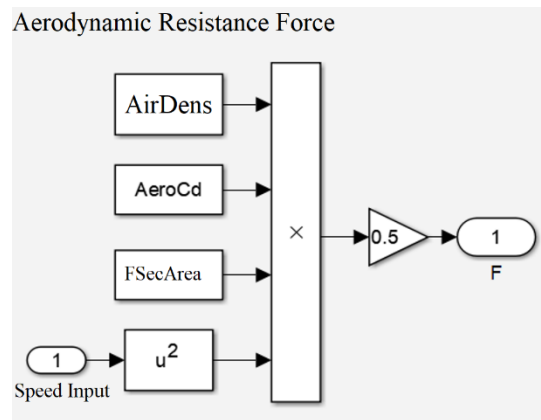


Figure 5. Aerodynamic Resistance Force Model

#### 2.2.2 Rolling resistance

Rolling resistance is affected by parameters such as vehicle mass, tire type, tire air pressure and road conditions.

Rolling resistance force:

$$F_r = m g f_{ro} \tag{2}$$

is calculated by this equation. In this equation, “ $f_{ro}$ ” refers to the rolling resistance coefficient [13]. Rolling resistance coefficients for different road conditions are given in Table 2. The rolling resistance force model is given in Figure 6.

Table 2. Rolling resistance coefficients for different road conditions [13]

Road Conditions	$f_{ro}$
Smooth asphalt, concrete	0.013
Small stone road	0.015
Cobblestone road	0.015
Macadamized road	0.02
Muddy road	0.05
Loose soil, sand	0.1...0.35

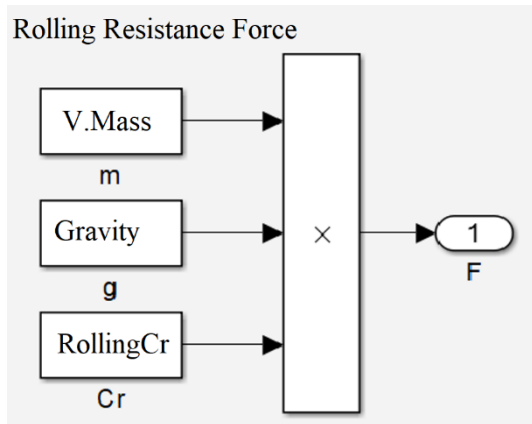


Figure 6. Rolling Resistance Force Model

**2.2.3 Acceleration resistance**

According to Newton's 2nd law of motion, during the acceleration and deceleration of an object, an inertial force occurs in the opposite direction to this motion. This force encountered during positive and negative acceleration of the vehicle is called the acceleration resistance. This resistance;

$$F_i = ma \tag{3}$$

is calculated by this equality [13]. Acceleration Resistance Force Model is given in Figure 7.

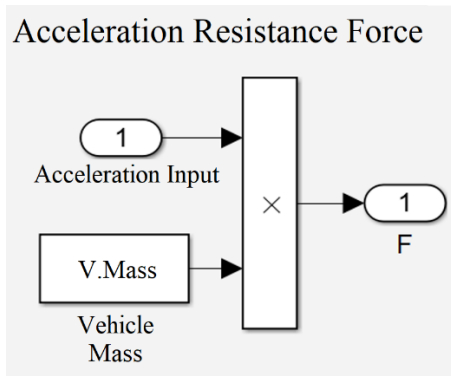


Figure 7. Acceleration Resistance Force Model

**2.2.4 Gradient resistance**

Gradient resistance is a resistance force that occurs due to the component of the Mass force during the movement of the vehicle on an inclined road and is opposite to the direction of movement of the vehicle. This resistance directly affects the mass of the vehicle and the slope of the hill. Gradient resistance;

$$F_{st} = mg \sin \alpha \tag{4}$$

is calculated by the equation 3. With “ $\alpha$ ”, the slope of the road is expressed in angle [13].

The model assumes that the vehicle is traveling on a straight road and has no hill resistance effect.

**2.2.5 Total Resistance Force:**

Total resistance force is the sum of aerodynamic, rolling, hill and acceleration resistances.

$$F_{Load} = F_i + F_{st} + F_r + F_a \tag{5}$$

is calculated by this equality. Torque force in the powertrain due to vehicle resistance forces,

$$T_{Load} = F_{Load} \times r_w \tag{6}$$

It is aimed to obtain more realistic data on modeling. Resistors acting on the vehicle are applied to the model as in Figure 8.

The total torque generated by multiplying the total resistance forces acting on the vehicle by the wheel radius and the total brake torque applied to the system by the brake model constitute the total resistance torque.

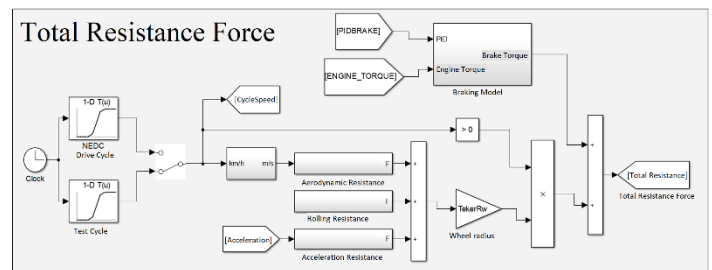


Figure 8. Total Resistance Force Model

A "Compare to Zero" block has been added to the model in order to prevent the application of a formula-induced torque to the powertrain while the vehicle is at a standstill. In this way, when the cycle speed is zero, the resistance forces affecting the vehicle are zeroed. After the total resistance torque affecting the vehicle is calculated, the power transmission system is used in the transfer function [14].

With the help of the "Manual Switch" added to the model, it is possible to choose between the two drive cycle in the model. In this way, the vehicle model can be controlled with a standard drive cycle or the model can be run by selecting the test drive cycle.

### 2.3. Speed control model (PID Controller)

Driving cycles are used as references in the simulation process and the model must be able to follow these cycles. For this reason, it is necessary to create a speed control model that can follow the reference. A PID controller is used for speed control in the model. The block that matches the speed values with the values coming from the driving cycle ensures that the output values and the torque value of the electric motor are formed. For this process, the output values of the PID controller are limited between "1" and "-1" values. For pedal control, "0-1" range is selected as accelerator pedal, "0 - (-1)" range is selected as brake pedal. In this way, it helped the braking model to control the brakes [15].

The Ziegler-Nichols method was used to find the PID controller parameters. According to this method, P (proportional value) value was increased, I (integral value) and D (derivative value) values were accepted as 0. After that, the parameters were adjusted with the "PID Tuner" in the PID controller block. Thus, the tracking process is provided with the lowest error and oscillation. Speed control model is shown in Figure 9.

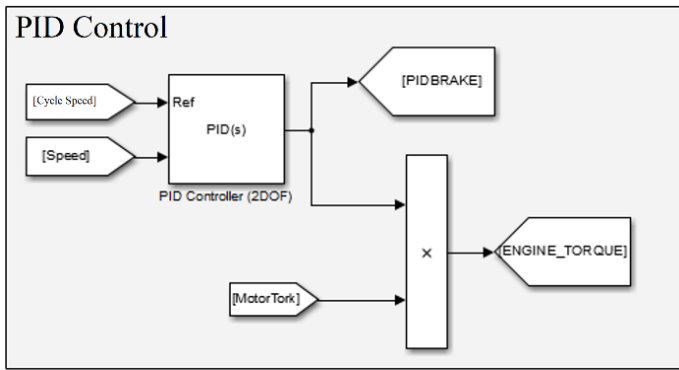


Figure 9. PID Control Model

### 2.4. Powertrain system model

The power transmission system transmits the motion energy obtained from the engine to the wheels [16]. "Rear Axle System AV 133" axle and differential system of ZF company was taken as a reference to be used in the designed bus and the differential reduction ratio was obtained from here. Figure 10 shows a schematic of a direct drive electrical vehicle.

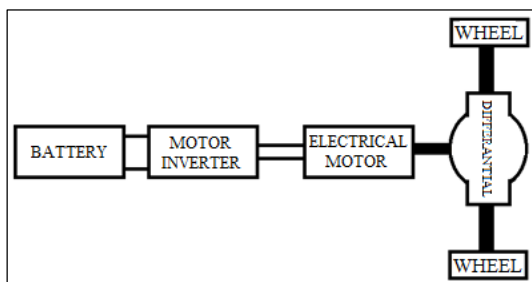


Figure 10. Schematic Of A Direct Drive Electrical Vehicle

In order to create the transfer function, some mathematical calculations must be done first. The moment of inertia occurs in the components that make the rotational motion due to their mass. It is known that the net torque value at the motor output is equal to the product of the total moment of inertia times the angular acceleration. As a result of this transfer function, it is desired to reach the speed information of the vehicle. For this reason, the net torque value at the output of the motor should be calculated first, then this torque value should be divided by the total inertia forces and the angular acceleration of the motor should be calculated. By integrating the angular acceleration value, the angular velocity of the motor is calculated. The angular velocity of the motor is the angular velocity at the differential input. It must therefore be divided by the differential reduction ratio. Thus, the speed at the differential output is calculated. The vehicle speed is calculated by multiplying this value by the wheel radius.

The mathematical operations of the power transfer transfer function used in the modeling process are performed as follows:

$$M_{net} = M_{motor} \times \eta_{motor} \quad (7)$$

$$M_{net} = \dot{w} \times I \quad (8)$$

$$M_{d_{in}} = M_{net} \quad (9)$$

$$M_{d_{out}} = M_{d_{in}} \times i_{diff} \times \eta_{diff} \quad (10)$$

$$M_{axle} = M_{d_{out}} - 2 \times I_{axle} \times \dot{w}_{axle} \quad (11)$$

$$M_{d_{out}} = M_{axle} + 2 \times I_{axle} \times \dot{w}_{axle} \quad (12)$$

$$M_{wheel} = M_{axle} - 6 \times I_{wheel} \times \dot{w}_{wheel} \quad (13)$$

$$M_{axle} = M_{wheel} + 6 \times I_{wheel} \times \dot{w}_{wheel} \quad (14)$$

The net torque will be calculated with the engine torque and the resistance torque generated in the wheels.

$$M_{net} = M_{d_{in}} \quad (15)$$

$$M_{net} = \frac{M_{d_{out}}}{i_{diff} \times \eta_{diff}} \quad (16)$$

$$M_{net} = \frac{M_{axle} + 2 \times I_{axle} \times \dot{w}_{axle}}{i_{diff} \times \eta_{diff}} \quad (17)$$

$$M_{net} = \frac{M_{wheel} + 6 \times I_{wheel} \times \dot{w}_{wheel} + 2 \times I_{axle} \times \dot{w}_{axle}}{i_{diff} \times \eta_{diff}} \quad (18)$$

$$M_{wheel} = M_{Load}, \quad \dot{w}_{axle} = \dot{w}_{wheel} = \frac{\dot{w}_{motor}}{i_{diff}} \quad (19)$$

is known. By arrange these equations;

$$M_{net} - \left( \frac{M_{Load}}{i_{diff} \times \eta_{diff}} \right) = \frac{6 \times I_{wheel} + 2 \times I_{axle}}{i_{diff} \times \eta_{diff}} \times \frac{\dot{w}_{motor}}{i_{diff}} \quad (20)$$

$$M_{net} - \left( \frac{M_{Load}}{i_{diff} \times \eta_{diff}} \right) = \frac{6 \times I_{wheel} + 2 \times I_{axle}}{i^2_{diff} \times \eta_{diff}} \times \dot{w}_{motor} \quad (21)$$

$$\dot{w}_{motor} = \frac{M_{net} - \frac{M_{Load}}{i_{diff} \times \eta_{diff}}}{\frac{6 \times I_{wheel} + 2 \times I_{axle}}{i^2_{diff} \times \eta_{diff}}} \quad (22)$$

By integrating the last equation;

$$w_{motor} = \int \left( \frac{M_{net} - \frac{M_{Load}}{i_{diff} \times \eta_{diff}}}{\frac{6 \times I_{wheel} + 2 \times I_{axle}}{i^2_{diff} \times \eta_{diff}}} \right) dt \quad (23)$$

the angular velocity of the motor is calculated [17]. Figure 11 is shown the Simulink powertrain model.

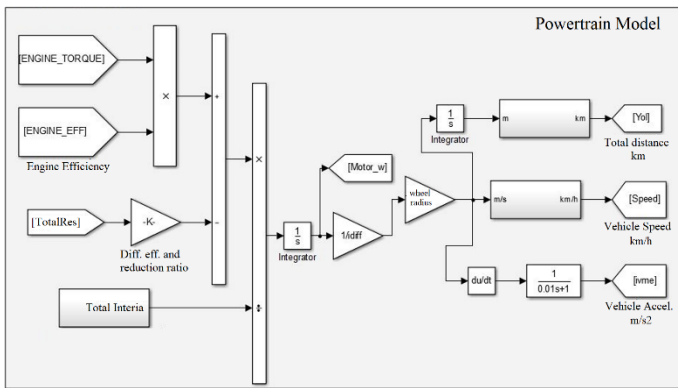


Figure 11. Powertrain Model

### 2.5. Regenerative brake model

The designed bus is required to recover energy by regenerative braking. For this reason, a regenerative braking system has been modeled and regenerative brake recovery has been assumed to be 30%. In the modeling process, the motor torque values formed by the values in the range of 1 - (-1) coming from the output of the PID controller were put into an 'if' loop and regenerative braking was provided with the values occurring in the 0 - (-1) range [18,19]. Brake model is shown in Figure 12.

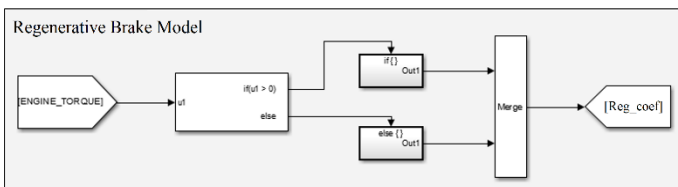


Figure 12. Regenerative Brake Model

### 2.6. Energy Consumption Model

The "SOC" method was used for the energy consumption model [20]. By using "SOC", the method of learning the current state of charge of the battery, the percentage of the battery consumed by the vehicle throughout the cycle was printed out and recorded. With this output, it is aimed to calculate the maximum range that the battery can achieve with 100% charge, and the capacity of the battery consumed per 100 km.

In the model, the efficiency and torque of the electrical motor are taken as input, so it is determined whether the electric motor operates in the drive mode or regenerative mode. Afterwards, the instantaneous power of the electrical motor was calculated by dividing the motor torque by the efficiency. If the electric motor is operating in regenerative mode, the battery is charged by gaining 30% from the kinetic energy of the vehicle.

The energy consumed by high and low voltage accessories is considered constant in all cases. The efficiency of the converter is taken into calculation when calculating the power amount of low voltage accessories. The total power consumed by the electric motor, low and high voltage accessories has been calculated. Then this value is integrated and the total amount of energy consumed by the vehicle during one cycle is calculated. The energy consumption model is shown in Figure 13.

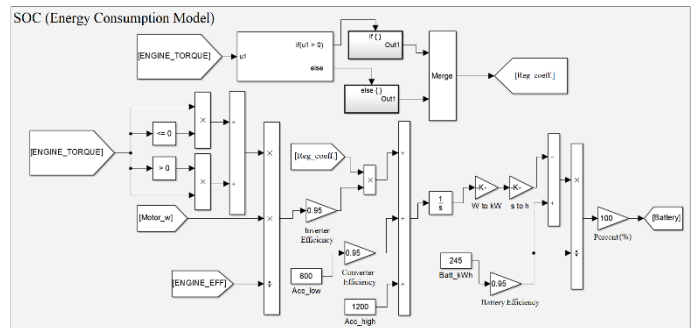


Figure 13. "State of Charge" Energy Consumption Model

### 2.7. Test drive cycle

A realistic driving cycle has been created and included in the vehicle model so that the vehicle modeled in Matlab / Simulink can be modeled in a more realistic way and compared with the buses available on the market. This test drive cycle was created on Eryaman-Kızılay 541 line of EGO organization affiliated to Ankara Metropolitan Municipality. An application specially made for this study is used to create a cycle. Vehicle speed information is received via GPS and recorded over time. The data taken from the application has been arranged and transferred to the model. Test driving cycle is shown in Figure 14 and its features are shown in Table 3.

Table 3. Test Drive Cycle Features

Time (s)	3190
Distance (km)	31.16
Maximum Speed (km/h)	87
Average Speed (km/h)	36
Conversion Sensitivity (m)	7

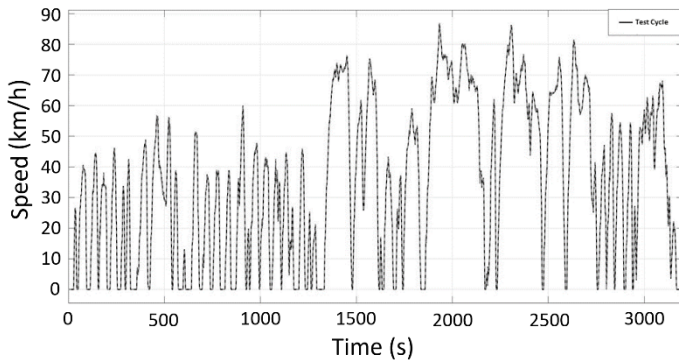


Figure 14. Test Drive Cycle

2.8. Simulation result model

Figure 15 is shown the output from the electricity consumption model and the remaining range, total range, battery capacity consumed per 100 km, the data obtained from the torque output of the engine and the result model where the engine power is calculated [21].

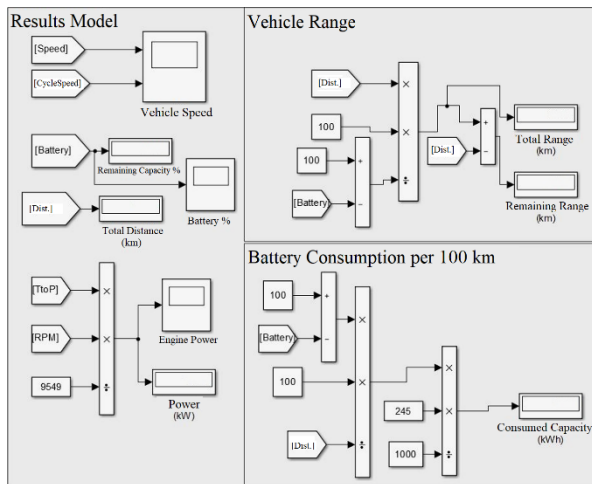


Figure 15. Simulation Result Model

3. Simulation results

After modeling, values such as energy consumption in the test drive cycle, remaining range, battery capacity consumed per 100 km were obtained according to vehicle parameters. According to this drive cycle, benefits from regenerative braking, fuel costs, effects of vehicle resistance force parameters on battery-range were examined for different vehicle status' which are simulated empty, half-full and full.

Results graphics of the electric bus model have been obtained. These graphics were created by following the test drive cycle. Figure 16 is shown the graph of the test driving cycle versus vehicle speed.

According to the simulation results including test driving cycles, vehicle speed follows the cycle speed. Thus, it is concluded that the energy consumption values obtained from the simulation applied are correct. In Figures 17 and 18, electric motor torque and speed can be seen in the test drive cycle.

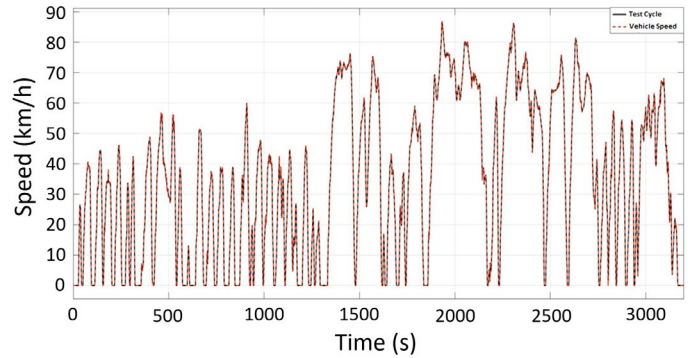


Figure 16. Driving Cycle and Vehicle Speed

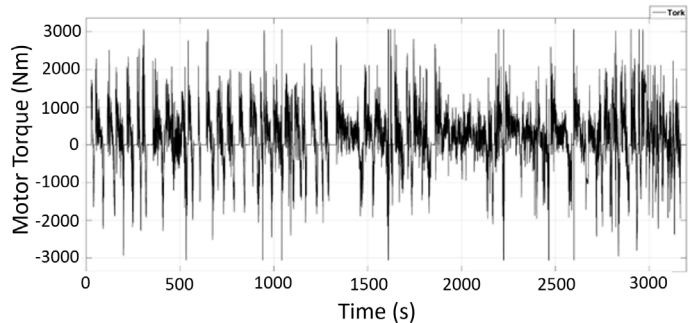


Figure 17. Electric Motor Torque Graph

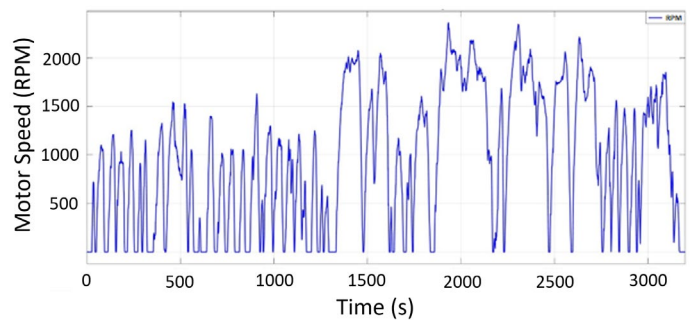


Figure 18. Electric Motor Revolution Graph

The acceleration and velocity graphs of the vehicle during the test driving cycle are shown in Figures 19 and 20. The acceleration of the modeled vehicle increases to 2.7 m / s<sup>2</sup> in the case of acceleration and up to -6.8 m / s<sup>2</sup> in the case of deceleration.

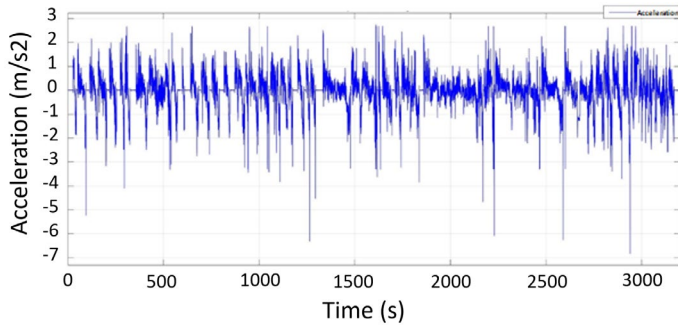


Figure 19. Vehicle Acceleration Graph

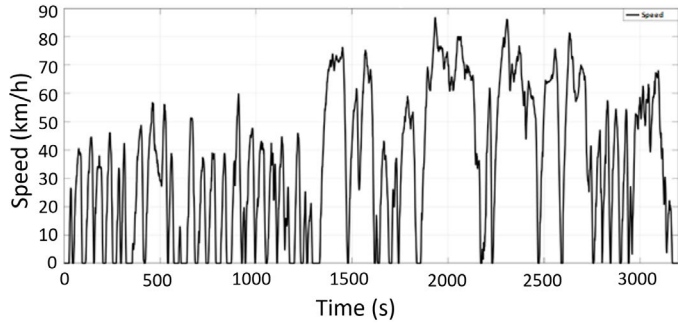


Figure 20. Vehicle Speed Graph

In the Simulink model, the vehicle mass has been changed according to the status of the vehicle being empty, half-full, full; and for these values remaining battery conditions, total distance, remaining range, 100 km-spent battery-capacity are shown in Table 4. The results obtained are shown in the graph in Figure 21. A more realistic energy consumption model was created by including low and high voltage accessories in the vehicle model, and energy consumption was upheld even when the vehicle was on steady state.

Table 4. Battery Consumption by Vehicle Mass

Vehicle Mass (kg)	10500	14000	17000
Total Distance (km)	335.2	226.6	114.6
Remaining Distance (km)	304	195.4	83.42
Battery Capacity Spent per 100 Km (kWh)	73.09	108.1	213.8
Battery Charge Status (%)	90.7	86.25	72.8

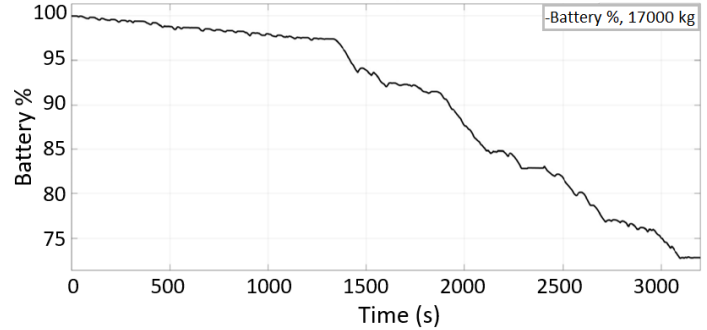
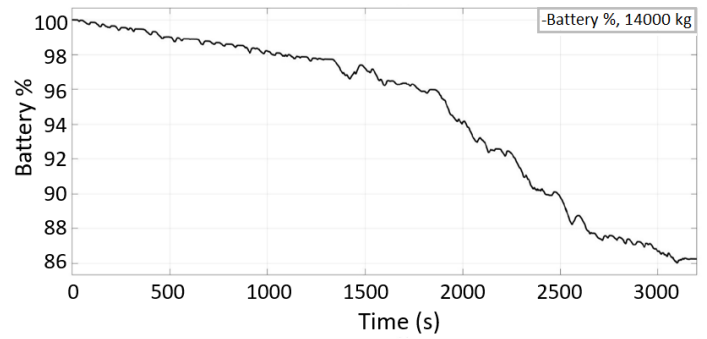
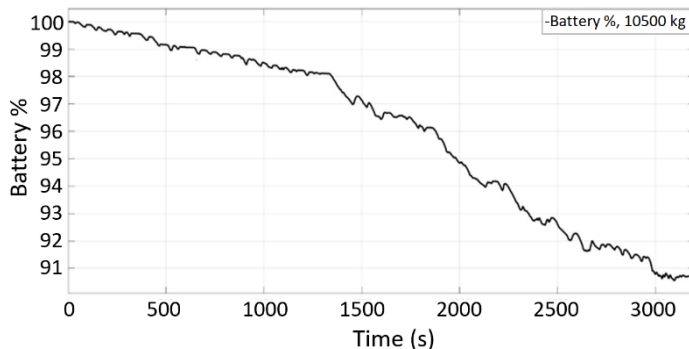


Figure 21. Battery Consumption Graph

The simulation was repeated for each mass on the Test Driving Cycle and the battery consumption results were obtained. According to this situation, it was observed that %9.3 battery capacity was consumed for 10500 kg vehicle mass, %13.75 battery capacity for 14000 kg vehicle mass, %27.2 battery capacity for 17000 kg vehicle mass during the 31.16 km driving cycle. Inner city buses vehicle mass varies continuously depending on the number of passengers. For this reason, based on half-full and full vehicle; When the vehicle is half full, an average of 7 full trips will be on the line, and when it is fully loaded, an average of 4 full trips will be able to go back and forth

### 3.1. Investigation of regenerative braking gain effect

Without changing the parameters on the model; Tests have been carried out for 10500, 14000 and 17000 kg vehicle conditions with the aim of observing the battery charge status and total range change while the regenerative braking system is activated and deactivated. The results according to these tests are shown in Table 5, Figure 22 and Figure 23.

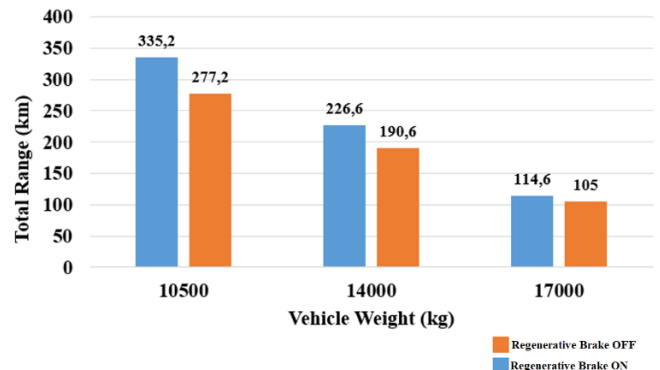


Figure 22. Effect of Regenerative Braking Gain on Total Range

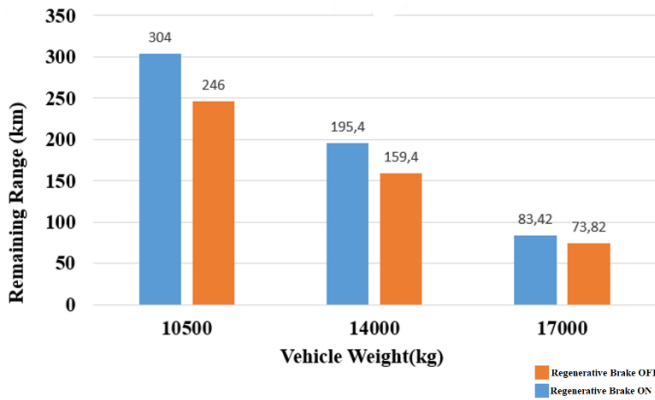


Figure 23. Effect of Regenerative Braking Gain on Remaining Range

Table 5. Regenerative Braking On/Off Results

Vehicle Mass (kg)	10500	14000	17000
Total Distance (km) (Regenerative Brake ON)	335.2	226.6	114.6
Total Distance (km) (Regenerative Brake OFF)	277.2	190.6	105
Remaining Distance (km) (Regenerative Brake ON)	304	195.4	83.42
Remaining Distance (km) (Regenerative Brake OFF)	246	159.4	73.82
Battery Capacity Spent per 100 Km (kWh) (Regenerative Brake ON)	73.09	108.1	213.8
Battery Capacity Spent per 100 Km (kWh) (Regenerative Brake OFF)	88.39	128.6	233.4
Battery Charge Status (%) (Regenerative Brake ON)	90.7	86.25	72.8
Battery Charge Status (%) (Regenerative Brake OFF)	88.76	83.65	70.31

Regenerative braking gain increased by 58 km for 10500 kg vehicle mass, 36 km for 14000 kg vehicle mass and 9.6 km for 17000 kg vehicle mass in total range. According to these results, it has been observed that there is a significant increase in the total range that can be traveled when regenerative braking gain is open.

### 3.2. The Effect of vehicle resistance parameters on range and battery consumption

The effect of vehicle resistance parameters on the modeled vehicle is examined in this section. Aerodynamic drag coefficient and rolling resistance coefficient were changed on the model and the simulation was repeated. As a result of the simulation, the effects of these two resistance parameters on the total range, remaining range, battery capacity and battery capacity spent per 100 km were examined. The results are shown in Tables 6 and 7.

Table 6. Effects of Aerodynamic Resistance

Aerodynamic Resistance Coefficient	0.6	0.65	0.7
Total Distance (km)	346.7	335.2	331.1
Remaining Distance (km)	315.6	304	300
Battery Capacity Spent per 100 Km (kWh)	70.66	73.09	73.99
Battery Charge Status (%)	91.01	90.7	90.59

Table 7. Rolling Resistance Effects

Rolling Resistance Coefficient ( <i>f<sub>ro</sub></i> )	0.01	0.015	0.02
Total Distance (km)	450.9	335.2	263.5
Remaining Distance (km)	419.7	304	232.4
Battery Capacity Spent per 100 Km (kWh)	54.34	73.09	92.96
Battery Charge Status (%)	93.09	90.7	88.18

As a result of the tests, the effects of the change in aerodynamic and rolling resistance coefficients on the modeled vehicle were examined. As a result, the effect of rolling resistance was %34.5 on ranges, while the effect of aerodynamic resistance was %3.43.

When the aerodynamic resistance coefficient, taken as 0.65, was changed to 0.6, the total range increased from 335.2 km to 346.7 km, and the battery usage decreased by %0.31. When the resistance value is taken as 0.70, the total range has decreased from 335.2 km to 331.1 km, and the battery usage has increased by %0.21. As can be seen from the values, the effect of aerodynamic resistance on the vehicle is very small. It did not have a significant effect on the capacity spent per 100 km.

When the rolling resistance coefficient, which was taken as 0.015, was changed to 0.010, the total range increased from 335.2 km to 450.9 km, and the battery usage decreased by %2.39. When the resistance value is taken as 0.020, the total range decreased from 335.2 km to 263.5 km, and battery usage increased by 2.52 percent. The spent capacity at 100 km decreased by 18.75 kWh for the resistance coefficient of 0.01, and increased by 19.87 kWh when the coefficient was made 0.02.

The values were obtained by changing the aerodynamic resistance and rolling resistance coefficients on the model. According to these, while the effect of aerodynamic resistance on the total and remaining range, battery capacity and battery capacity consumed per 100 km was minor, but rolling resistance majorly changed the values.

### 3.3. Fuel consumption vs emission comparison

Fuel consumption, fuel economy and accordingly emission status of the modeled city bus compared to its equivalents with an internal combustion engine will be examined under this title. Table 8 shows the fuel consumption of the modeled vehicle and the vehicle with ICE, the fuel liter price and the amount spent for the fuel consumed per 100 km.

Table 8. Fuel Consumption Values

	Modeled Bus	Diesel Bus	CNG Bus
Fuel consumption (100 km)	73.09 kWh	31 L	32 m <sup>3</sup>
Fuel Unit Price	0,12 USD/kWh	1,51 USD/L	0,89 USD/m <sup>3</sup>
Fuel Cost (for 100 km)	9,06 USD	46,81 USD	28,64 USD

According to the values given in the table, based on today's fuel unit prices for 100 km fuel consumption, the fuel cost of the modeled electrical bus; It is 37.74 USD more economical than a diesel bus and 19.57 USD more than a CNG bus. According to this information, it can be said that the electric bus is a better choice in terms of fuel costs.

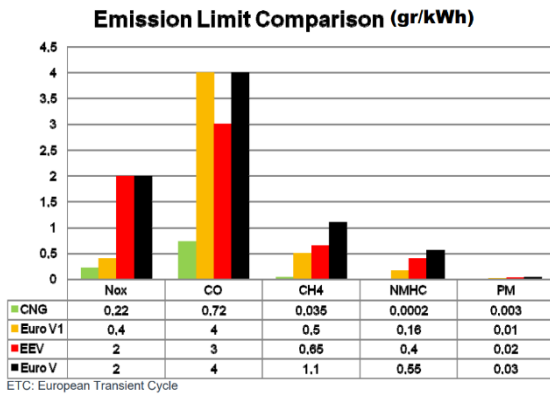


Figure 22. Emission Values [22]

In Figure 22, CNG, EuroV1, EEV and Euro V; Emission values are seen in terms of Nox, CO, CH<sub>4</sub>, NMHC, and PM. Electric energy used as fuel in vehicles has no emission value. This makes fully electrical vehicles one of the most environmentally friendly vehicles.

#### 4. Conclusions

In order to provide the real driving conditions for the electrical vehicle modeled in MATLAB/Simulink, a test drive cycle was created on the line 541 of the EGO organization of Ankara Metropolitan Municipality.

- When the electrical vehicle modeled in MATLAB/Simulink was simulated with reference to the test driving cycle, it was seen that it consumed 73.09 kWh of energy per 100 kilometers and offered a range of 335.2 kilometers with a fully charged battery.
- The fuel consumption and cost of the modeled electric bus compared to similar buses using Diesel and CNG fuel in the market were compared. Accordingly, a fuel cost of 37.74 USD in a diesel bus and 19.57 USD in a CNG bus is saved.
- It has been observed that the electric bus provides a great advantage in exhaust emissions and noise emissions compared to the buses using Diesel and CNG fuel. When reviewed only as a

vehicle, the noise emission is greatly reduced, while the exhaust emission is zeroed.

- Parameters such as aerodynamic drag coefficient, rolling resistance coefficient, regenerative braking gain and vehicle mass were changed on the modeled vehicle and as a result, the change of values such as range, energy consumption was examined.
- The regenerative braking gain in the electric vehicle model has increased by 58 km for 10500 kg vehicle mass, 36 km for 14000 kg vehicle mass and 9.6 km for 17000 kg vehicle mass in the total range. Based on these results, it is seen that regenerative braking is of great importance for the vehicle.
- The mass parameter was changed to be empty, half-full and full weight on the modeled vehicle. Accordingly, it was observed that %9.3 battery capacity was consumed for 10500 kg vehicle mass, %13.75 battery capacity for 14000 kg vehicle mass, %27.2 battery capacity for 17000 kg vehicle mass during the 31.16 km driving cycle. Based on half-full and full vehicle; When the vehicle is half full, it will be able to make an average of 7 full trips on the line, and an average of 4 full trips when fully loaded.

#### Conflict of Interest Statement

The authors declare that there is no conflict of interest.

#### CRedit Author Statement

**Oğuzhan Karakaş:** Methodology, article editing, Writing original draft and revision; **Umut Buğra Şeker:** Methodology, article editing, Writing original draft and revision; **Hamit Solmaz:** Supervision

#### References

1. Kocakulak, T., & Solmaz, H. (2020). "Heci Menzil Artirici Motor Kullanilan Seri Hibrit Bir Aracin Modellenmesi", Gazi Üniversitesi Fen Bilimleri Dergisi Part C: Tasarım ve Teknoloji, 8(2), 279-292.
2. Kerem, A., "Elektrikli Araç Teknolojisinin Gelişimi ve Gelecek Beklentileri", Mehmet Akif Ersoy Üniversitesi Fen Bilimleri Enstitüsü Dergisi, 5(1), 1-2 2014.
3. Emadi, A., Ehsani, M., Miller, J. M., 2004. "Vehicular Electric Power Systems Land, Air, And Space Vehicles", Marcel Dekker, New York.
4. Internet. "https://www.ego.gov.tr/tr/sayfa/61/istatistikler" [Online].
5. Chan, C. C., Wong, Y. S., 2004. "Electric Vehicles Charge Forward, Ieee Power Energy Mag", Vol.2, No.6, Pp.24-33.
6. School Of Public And Environmental Affairs At Indiana University, "Plugin Electric Vehicles: A Practical Plan For Progress", Indiana, 2011
7. Solmaz H., & Kocakulak T., "Determination of Lithium Ion Battery Characteristics for Hybrid Vehicle Models." International Journal of Automotive Science and Technology, 4(4), 264-271.
8. Ünlü N., Karahan Ş., Tür O., Uçarol H., Özsu E., Yazar A., Turhan L., Akgün F., Tırıs M., "Elektrikli Araçlar", TÜBİTAK – Marmara Araştırma Merkezi Enerji Sistemleri ve Çevre Araştırma Enstitüsü, Kocaeli, 6-10 (2003).
9. Xue, X. D., Cheng, K. W. E. And Cheung, N. C., "Selection Of Electric Motor Drives For Electric Vehicles", Australasian Universities Power Engineering Conference, Hong Kong, 170-175 2008.
10. Hurst, D. ve Wheelock, C., "Battery Electric And Plug-In Hybrid Electric

- Vehicles: Oem Strategies, Demand Drivers, Technology Issues, Key Industry Players, And Global Market Forecasts”, Pike Research, New York, 2010.
11. Başer E., “Elektrikli Araçlarda Yol Koşullarına Uygun Motor Seçimi Algoritması Geliştirme”, Düzce Üniversitesi Fen Bilimleri Enstitüsü, Düzce, 2016.
  12. Internet. “<https://www.tm4.com/products/direct-driveelectricpowertrain/sumo-hd>” [Online].
  13. S. Çetinkaya, Taşıt Mekaniği Geliştirilmiş 8. Basım, 2017
  14. Fan B. S., “Modeling and Simulation of A Hybrid Electric Vehicle Using MATLAB/ Simulink and ADAMS”, University of Waterloo, Mechanical Engineering thesis, Canada 2007.
  15. Gökçe, C., “Modeling And Simulation Of A Series Parallel Hybrid Electrical Vehicle”, Master Thesis, İstanbul Technical University Institute Of Science And Technology, Istanbul (2005).
  16. Chauhan V. S., “Simulation of Electric Vehicle Including Different Power Train Components”, Master Thesis, Czech Technical University, Prague, 2017.
  17. Kiyakli, A. O., & Solmaz, H. (2018). “Modeling of an electric vehicle with MATLAB/Simulink”. *International journal of automotive science and technology*, 2(4), 9-15.
  18. Yurdaer, E., & Kocakulak, T. (2021). “Comparison of Energy Consumption of Different Electric Vehicle Power Systems Using Fuzzy Logic-Based Regenerative Braking.”, *Eng. Perspect*, 1(1), 11-21.
  19. Şahin Y., Güneş U., Umman F., Ceceloğlu A. C., Güner H. E., Ertunç H. M., “Bulanık Mantık Kontrollü Rejeneratif Frenleme Sistemi Regenerative Braking System using Fuzzy Logic Controller”, Kocaeli Üniversitesi Mekatronik Mühendisliği, 2015
  20. Mastanamma Y., Bharathi M. A., “Electric Vheicle Mathematical Modelling an Simulation Using MATLAB-Simulink”, *Journal of Electrical and Electronics Engineering*, 47-53 (2017)
  21. Park C., Kwon M., Jeong N., Lee S., Suh M., Kim H., Hwang S., “Development of Electric Vehicle Simulator for Performance Analysis”, *Universal Journal of Mechanical Engineering* 2 (7), 231-239 2014.
  22. Internet. “[https://www.grazerea.at/cms/upload/gashigh/staimer\\_man\\_cng\\_buses.pdf](https://www.grazerea.at/cms/upload/gashigh/staimer_man_cng_buses.pdf)” [Online].
  23. Çağlar S., İnce B., Koçak M., Saygılı H. H., “Hibrit-Elektrikli Şehir İçi Otobüslerde Yakıt Ekonomisinin İyileştirilmesine Yönelik Enerji Yönetim Sistemi Algoritmalarının Tasarımı”, 8. Otomotiv Teknolojileri Kongresi, OTEKON, 2016



## Experimental investigation and optimization of HCCI engine fueled by isopropanol and heptane mixture

Seyed Mohammad Safieddin Ardebili<sup>1\*</sup>, Çağatay Nacak<sup>2</sup>, Tolga Kocakulak<sup>3</sup>, Mustafa Babagiray<sup>4</sup>

<sup>1</sup> Turkey Department of Biosystems Engineering, Shahid Chamran University of Ahvaz, Ahvaz, Iran

<sup>2</sup>Automotive Engineering Department, Faculty of Technology, Gazi University, Ankara, 06500

<sup>3</sup>Electricity and Energy Department, Vocational High School of Technical Sciences, Burdur Mehmet Akif Ersoy University, Burdur, 15030, Turkey

<sup>4</sup>Automotive Engineering Department, Faculty of Technology, Afyon Kocatepe University, Afyonkarahisar, 03200, Turkey

### ABSTRACT

Nowadays optimization is increasing in experiments on the engine tests studies. In this study, the test fuel obtained by mixing isopropanol with n-heptane fuel under various engine conditions in HCCI mode was examined combustion, performance and emissions. The study was carried out both experimentally and statistically. Set as engine parameters, different engine speed, test fuel with isopropanol (IP20-IP40) and excess air ratio for experimental study. Engine speed is 800 rpm - 1200 rpm, excess air ratio is 1.6 and 2.8, and isopropanol ratio in test fuel of 20% and 40%. From the experiment, investigations were made on effective torque, indicated mean effective pressure, indicated thermal efficiency, maximum pressure increase rate, start of combustion (SOC), combustion duration, COVIMEP, HC, CO and NOx. Before the experiments, experimental series were determined with Response Surface Method, Central Compound Design matrix. Experiments were carried out with the experimental series obtained and the data were analysed. Counter charts, ANOVA results and quartic models were obtained by entering the combustion, performance and output of the HCCI engine into the RSM interface. Then, the targeted response parameters were entered and optimization was made to determine the optimum input parameter. Response parameters under optimum operating conditions Effective Torque 11.438 Nm, IMEP 4.366 bar, MPRR 2.747 bar/°CA, COVIMEP 4.364%, CA10 2.315 °CA, CA50 7 °CA, CA10-CA90 36.245 °CA, UHCs 324.562 ppm, CO 0.0118% and NOx 2.549 ppm were determined.

**Keywords:** HCCI engine, Isopropanol, Response surface method, Design of experiments

History	Author Contacts	<a href="http://dx.doi.org/10.29228/eng.pers.51253">http://dx.doi.org/10.29228/eng.pers.51253</a>
Received:	*Corresponding Author	
Accepted:	e-mail addresses :	<a href="mailto:m.safieddin@scu.ac.ir">m.safieddin@scu.ac.ir</a> , <a href="mailto:nacakcagatay@gazi.edu.tr">nacakcagatay@gazi.edu.tr</a> , <a href="mailto:tkocakulak@mehmetakif.edu.tr">tkocakulak@mehmetakif.edu.tr</a> , <a href="mailto:mbabagiray@aku.edu.tr">mbabagiray@aku.edu.tr</a>
	Orcid numbers :	0000-0002-5164-1284, 0000-0001-6255-1148, 0000-0002-1269-6370, 0000-0002-2482-6662

### 1. Introduction

Today, an increase is observed in global warming and acid rain events caused by the risk of depletion of fossil fuels and the rapid increase in emission emissions [1-4]. Due to these concerns, researchers have turned to studies aimed at increasing efficiency and reducing harmful emission gases in the energy conversion process. Today, internal combustion engines are widely used for the production of mechanical energy, especially in mobile vehicles. Although compression and spark ignition engines are mostly used in this internal combustion engine group, it is on the agenda for engines operating with the HCCI combustion principle, with high efficiency and low emission gas values [5-8].

The basic operating principle of the HCCI engine can be defined as the start of combustion by taking the fuel / air mixture into the

cylinder and compressing it [9-11]. HCCI combustion can occur with liquid or gaseous fuels by making structural changes on the existing internal combustion engine [12]. In addition to combustion, gasoline, diesel fuels, HCCI also allows its use with alternative fuels such as biofuels, biodiesel, and hydrogen [13]. The use of alternative fuels on the HCCI engine enables improvement in parameters such as engine operating efficiency and emission values [14, 15].

It is aimed to improve the performance and emission values of the HCCI engine by adding different additives to the fuels used on HCCI engines [16]. Gainey et al., experimentally studied the input parameters of an HCCI engine and the combustion process by adding different additives to the fuels used. Isopropanol, butanol, ethanol and methanol additives were added to the fuel. They saw that the reactivity of the isopropanol blended fuel is low and the ambient temperature must be high for the combustion to start. With the increase in

ambient temperature, they achieved the highest NO<sub>x</sub> emission release with isopropanol additive [17]. Uyumaz et al., experimentally investigated the effect of using isopropanol and n-butanol additive at different concentrations and the inlet air temperature on the HCCI engine. He observed that the start of combustion was delayed in all fuel mixtures with the increase of inlet air temperature. Increasing isopropanol concentration also advanced the initiation of combustion. It concluded that isopropanol fuel burns in a more controlled manner than n-butanol fuel [18]. Calam et al., experimentally investigated the effect of isopropanol use on HCCI engine combustion and emissions. They used pure n-heptane and n-heptane isopropanol fuels as test fuel. They saw that the burning time was prolonged with the use of the fuel added with isopropanol. They also observed a decrease in the rate of pressure increase with the fuel used in isopropanol [19]. Different optimization methods are used to determine optimum engine parameters and fuel mixtures. Ardebili et al. Aimed to determine the optimum fusel oil concentration by using RSM in their studies. They carried out experiments with a total of 5 different fuels between 0% and 100%. Optimum results were obtained with a fuel mixture with a concentration of 25% fusel oil [30]. Awad et al. Obtained successful results by using RSM in determining the optimum additive concentration in the fuel mixture. It shows that this method is suitable for use on internal combustion engines [20].

It is known that engine speed and lambda values, which are HCCI engine input parameters, affect engine performance and emissions. It is aimed to keep such parameters at the optimum level for the HCCI engine. The response surface method (RSM) is widely used in the optimization of internal combustion engine parameters. Solmaz et al. used the RSM method for optimization of an HCCI engine parameters. When they compared the values they obtained after optimization with the results they obtained with the experimental method, they obtained successful results [11]. Mahla et al. Optimized using the RSM method in a compression ignition engine operating with biogas and diesel fuel. As a result of the study, it was seen that the parameter values obtained by the optimization method were consistent with the experimental results [21].

In this study, performance, emission, and combustion results of HCCI engine mode under different isopropanol concentrations and engine parameters conditions were obtained experimentally and statistically. Engine speed, excess air ratio and fuel types with different isopropanol concentrations were used as variable parameters. The effective torque, IMEP, ITE, MPRR, COVIMEP, UHCs, CO and NO<sub>x</sub> values were examined. Statistical analysis was carried out using the RSM in the Design Expert 12 environment. Counter charts, ANOVA results and quartic models were obtained by inputting the performance, emission, and combustion values of the HCCI engine to the RSM interface. Optimization was carried out in order to determine the optimum input parameters by inputting the targeted response parameters from the HCCI engine.

## 2. Material and Methods

### 2.1 Experimental Setup

The experiments were performed in a Ricarda Hydra single cylinder test engine. Besides, in the experiments, SI-HCCI was used as the test engine. Schematic view of the experimental setup and the

properties of the test engine are seen in Fig.1. and Table 1, respectively.

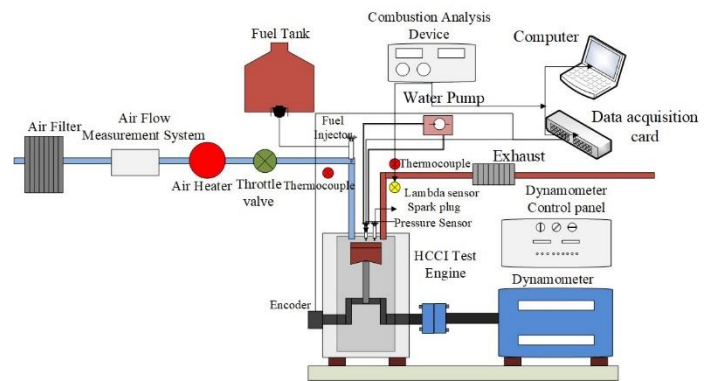


Figure 1. Schematic view of the experimental setup

Equations must be numbered consecutively and located at the right margin as in Eq. (1) below. Clear original figures in black and white should be used.

Table 1. Properties of HCCI engine

Brand-Model	Ricardo Hydra
Number of cylinder	1
Volume (mL)	450
Bore x Stroke (mm)	80.26 x 88.90
Compression ratio	5:1-13:1
Maximum power (kW)	15 @ 4500 rpm
Maximum speed (rpm)	5400
Maximum cylinder pressure	120 bar
Fuel system	Port type
Cooling system	Water cooled

During the experiment, a homogeneous air-fuel mixture was taken into the cylinder with the port injection system. The injection amount of the injector was adjusted using the potentiometer. The injectors were electronically controlled to determine fuel consumption and keep the air / fuel ratio constant. Injection properties of all fuels are determined before the tests are carried out. The potentiometer scale was set to 1.0, 2.0, 4.0, 6.0, 8.0 and 10.0 and the test motor was run at constant speed. The gas tank was placed on a precision scale (precision 0.01 g) and the fuel quantity was set at 120 seconds. In the current system, the injector is adjusted according to the position of the potentiometer.

In the experiments, the potentiometer was precisely adjusted for each lambda value. The motor was placed in a McClure DC dynamometer capable of absorbing 30 kW of power. The heating system, which heats the intake air, is in front of the intake manifold attached to the cylinder block. A K type thermocouple was used to measure the air inlet temperature. A closed loop controller was used to keep the temperature constant. In-cylinder pressure was measured with Kistler 6121 model piezoelectric pressure sensor and its technical specifications are given in Table 2.

Table 2. Pressure sensor specifications

Brand – Model	Kistler – 6121
Measuring range (bar)	0 to 250
Sensitivity (pC/bar)	14.7
Temperature (K)	223 to 623
Linearity (+/- %)	<0.5

The measured signals were amplified in the Cussons P4110 model combustion analyzer and analyzed using a National Instruments brand USB 6259 model data acquisition card and recorded in the computer. In addition, Opkon brand 0.36 CAD precision encoder was used to determine the position of the piston in the cylinder. The technical characteristics of the encoder are presented in Table 3. Fifty consecutive data cycles were averaged to prevent cyclical differences that could occur during the experiment.

Table 3. Encoder specifications

Brand – Model	Opkon
Output	Line driver
Supply DC Voltage (V)	5
Shaft - Body Diameter (mm)	8 - 50
Pulse per Rotation	1000
Temperature (K)	253 to 353
Max. Operating Speed (rpm)	4000

The engine was first started in spark ignition mode and then the spark plug was turned off from the control panel to allow HCCI combustion. The engine coolant and lubricating oil temperatures were checked to make the results more stable. As a result of this process, the cooling water temperature was fixed at 343 K and the lubricating oil temperature as 333 K. The experiments were carried out at an engine speed of 800-1200 rpm and a constant intake air temperature of 333 K. In this study, IP20, IP40 and n-heptane test fuels were used. The properties of n-heptane and isopropanol are shown in Table 4 [6, 20, 22, 23].

Table 4. Properties of fusel oil and n-heptane fuels [9]

	isopropanol	n-heptane
RON	107	0
Density (kg/m <sup>3</sup> at 15.4 °C)	809	695
Boiling point (K)	355	371
Low heating value (kJ/kg)	30,447	44,566

Exhaust gas was analyzed using Bosch's BEA350 emission meter. Table 5 shows the technical characteristics of the exhaust gas analyzer used in the test.

Table 5. Exhaust gas analyser specifications

	Measuring range	Sensitivity
CO (%)	0 – 14	0.001
CO <sub>2</sub> (%)	0 – 18	0.01
HC (ppm)	0 – 9999	1
NO <sub>x</sub> (ppm)	0 – 5000	1
O <sub>2</sub>	0 – 25	0.01
Opacity (%)	0-100	0.1
Lambda	0 - 4	0.001

## 2.2. Combustion Analysis Method

The in-cylinder pressure was calculated by averaging the fifty cycle data obtained. For this purpose, a special algorithm was designed using the MATLAB. With the help of this algorithm, in-cylinder pressure, heat release, IMEP, start of combustion, burning time and specified thermal efficiency are calculated.

HRR is determined with the help of the first law of thermodynamics. Therefore, mass and gas leaks in a cycle are ignored. In calculating the heat dissipation, heat transfer from the cylinder wall to the outside is included. HRR based on HCCI engine crankshaft angle is calculated using Eq. (1) of the paper in front 9. They should be numbered consecutively. While referring a journal paper, volume, number, page numbers and year must be given. Standard APA referencing style must be used.

$$\frac{dQ}{d\theta} = \frac{k}{k-1} p \frac{dV}{d\theta} + \frac{k}{k-1} V \frac{dP}{d\theta} + \frac{dQ_{heat}}{d\theta} \quad (1)$$

Calculation of the amount of heat transfer occurring on the cylinder walls of the internal combustion engine (ICE) based on Newton's cooling principle is calculated with Eq. (2):

$$\frac{dQ_{heat}}{d\theta} = \frac{1}{6 \times n} \times h_g \times A \times (T_g - T_w) \quad (2)$$

The ITE value of the HCCI engine was calculated with Eq. (3).

$$\eta_T = \frac{W_{net}}{\dot{m}_{fuel\ oil} \times Q_{LHV\ fuel\ oil} + \dot{m}_{n-heptane} \times Q_{LHV\ n-heptane}} \quad (3)$$

The net work value of one cycle of the HCCI engine was calculated with Eq. (4).

$$W_{net} = \int PdV \quad (4)$$

IMEP was calculated with Eq. (5).

$$IMEP = \frac{W_{net}}{V_{stroke}} \quad (5)$$

## 3. Design of Optimization Parameters

In optimization studies, the results obtained from engine tests are expected to be statistically optimum. Therefore, the response surface methodology (RSM) is used in this research study. The software chosen for the response surface methodology is Design Expert 12. Central Compound Design (CCD) was used in the design of the response surface methodology which is generally preferred in optimizations. The experiments were optimized using ANOVA (analysis of variance) table. Engine speed (rpm), air excess coefficient and

fuel type were determined as independent variables. The design matrix has been changed for the three variables and the limit parameters are given in the Table 6. Total of 26 experiments were expected for three determined dependent variables in order to provide optimum working conditions.

Table 6. Operating range and levels for independent variables

Ind. variables	Unit	$X_i$	Operating Range and Levels				
			$-\alpha$	-1	0	+1	$+\alpha$
Engine speed	(rpm)	$X_1$	800	800	1000	1200	1200
Lambda		$X_2$	1,6	1,6	2,2	2,8	2,8
Isopropanol ratio	(%)	$X_3$	20	20	-	40	40

In the established model, the engine speed was determined between 800 - 1200 rpm, and the air excess coefficient was determined between 1.6 - 2.8. IP20 (20% Isopropanol-80% Heptane) and IP40 (40% Isopropanol-60% Heptane) were selected as the fuel type. Effective torque (Nm), IMEP (bar), MPRR (bar/oCA), COVIMEP (%), CA10 ( $^\circ$ ), CA50 ( $^\circ$ ), CA10-CA90 ( $^\circ$ ), indicated thermal efficiency (%) and CO (%), HC (ppm), and NOx (ppm) emissions were determined as dependent variables (response variables). The quartic model was chosen for the optimization of all dependent variables. General equation of the quartic model [24]:

$$\eta = \beta_0 + \sum_{i=1}^k \beta_i x_i + \sum_{i=1}^k \beta_{ii} x_i^2 + \sum_{i=1}^k \beta_{iii} x_i^3 + \sum_{i=1}^k \beta_{iiii} x_i^4 + \sum_{i=1}^k \sum_{j=1, j < i}^k \beta_{ij} x_i x_j \quad (6)$$

In Eq. (6),  $\eta$  is the response,  $\beta_0$  means constant,  $\beta_i, \beta_{ii}, \beta_{iii}$  and  $\beta_{iiii}$  are regression coefficients,  $\beta_{ij}$  means quartic coefficient, and  $x_i$  denotes input variable. The significance level F-value and p-value of the independent variables are determined. In dependent variables, the fact that the large F-value and small p-value are increases the importance level. The p-value shows the effect of input parameters on response values. If the p-value of any input parameter is less than 0.05, that parameter has a great effect on the model [25]. The indicator that the regression statistics are compatible is expressed with goodness of fit ( $R^2$ ). The  $R^2$  value indicates the agreement of the statistical model results with the experimental results [26].

#### 4. Analysis of the Model

The model which to coherent the between parameters are fine because the difference between  $R^2$  and the goodness of predictions (Adj.  $R^2$ ) of the regression statistics in all the analysis results are less than 0.02. Emission and performance values have been examined and optimized by taking into account parameters such as engine speed, air excess coefficient and different fuel type, which we have determined as input values in the HCCI engine that we conducted the experiments. The values obtained were analysed and interpreted in detail under separate titles and detailed graphics. In ad-

dition, optimum parameter values were determined to reach the targeted response values.

#### 4.1. Interaction Effects of Optimization

##### 4.1.1. Effective torque

The optimization values about effective torque are shown in the Table 7. According to the ANOVA results for effective torque, it is seen that the established model has a significant effect on effective torque. The p-value that measures the effect of engine speed, air excess coefficient and fuel type on effective torque is below 0.05. According to the F-value, it can be concluded that the fuel type is more effective on the effective torque than the engine speed and the air excess coefficient.

Table 7. ANOVA table for effective torque (Nm)

Source	Sum of Sq.	Mean Sq.	F-value	p-value	Remarks
Model	123,38	7,71	136,89	< 0.0001	significant
$X_1$ - Engine speed	0,6006	0,6006	10,66	0,0098	significant
$X_2$ -Lambda	11,39	11,39	202,22	< 0.0001	significant
$X_3$ -Fuel	29,09	29,09	516,46	< 0.0001	significant
Residual	0,507	0,0563			
Cor Total	123,88				

In the analysis which is using the quartic model, the  $R^2$  value of the goodness of fit is checked to determine the correlation fit of the input parameters used in the research. For the effective torque, the  $R^2$  value was seen as 0.9959 and the regulated  $R^2$  (Adj.  $R^2$ ) value was obtained as 0.9886. Since the difference is less than 0.02, it has been seen that the results are within acceptable limits and compatible. The quartic model Eq. (7) for effective torque generated by the response surface method.

$$T_{ef} \text{ (Nm)} = 6 - 0,388X_1 - 1,688X_2 + 1,584X_3 - 0,431X_1X_2 - 0,113X_2X_3 + 1,638X_1^2 - 0,888X_2^2 - 0,394X_1X_2X_3 + 0,569X_1^2X_2 - 0,155X_1^2X_3 + 0,606X_1X_2^2 + 0,52X_2^2X_3 - 1,394X_1^2X_2^2 - 0,344X_1^2X_2X_3 + 0,894X_1X_2^2X_3 \quad (7)$$

The effective torque value in internal combustion engines is important parameters in terms of performance. Figures 2a and 2b there are graphs of IP20 and IP40 fuels, respectively. The graphs show the effect of air excess coefficient on effective torque depending on engine speed. The increase in the amount of isopropanol in the fuel mixture has increased the effective torque value. Isopropanol's high-octane number and its density in the mixture is the reason for the increase. In addition, as the excess air coefficient increases in the experiments, the torque value decreases. Reason for this is that the air / fuel ratio in the cylinder is a lean mixture. While a maximum torque of 6.5 Nm was obtained in the experiments with IP20, maximum torque values of 12.4 Nm were reached with IP40 [9, 27].

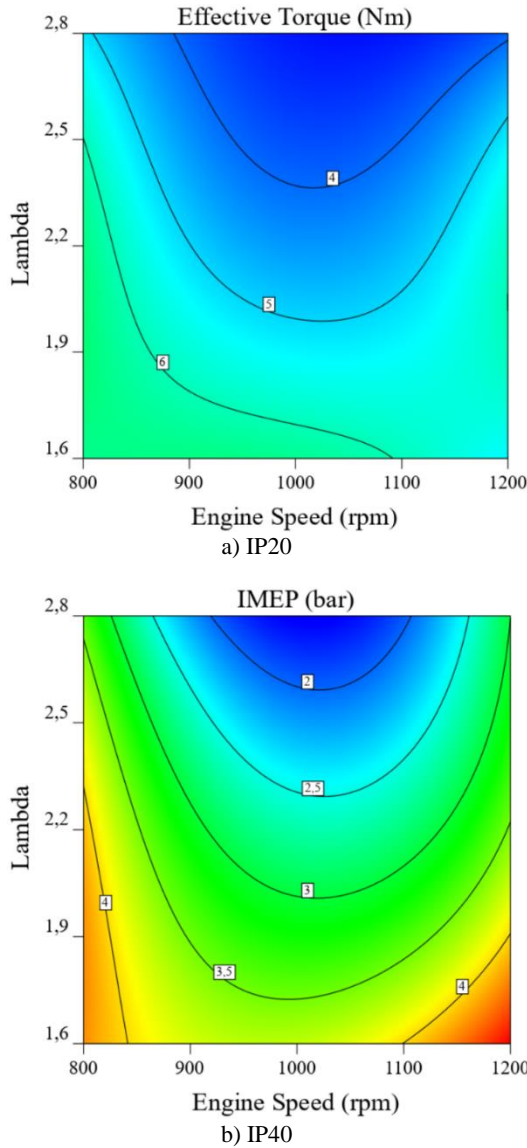


Figure 2. Effect of lambda and engine speed on effective torque(a and b)

**4.1.2. Indicated mean effective pressure (IMEP)**

ANOVA results with IMEP values are shown in Table 8. As seen in the table, it is significant in terms of the IMEP of the model. It is seen that the effect of independent variables on IMEP is significant (p-value <0.05). The p-value is less than 0.05 in all input parameters. The p-value is <0.0001 in all parameters of engine speed, air excess coefficient and fuel type. The fuel type has the highest F value than others. This means that the fuel is an effective parameter on IMEP.

Table 8. ANOVA table for indicated mean effective pressure (IMEP)

Source	Sum of Sq.	Mean Sq.	F-value	p-value	Remarks
Model	10,7	0,669	798,9	< 0.0001	significant
X1- Engine speed	0,1846	0,1846	220,43	< 0.0001	significant
X2 -Lambda	1,59	1,59	1897,57	< 0.0001	significant
X3 -Fuel	3,72	3,72	4438,59	< 0.0001	significant
Residual	0,0075	0,0008			
Cor Total	10,71				

For the indicated mean effective pressure (IMEP), the correlation coefficient R2 was 0.9990 and the adjusted correlation coefficient R2 (Adj. R2) was 0.9980. Since the difference is less than 0.02, it has been seen that the results are within acceptable limits and compatible. The quartic model Eq. (8) generated by the response surface method for indicated mean effective pressure.

$$\begin{aligned}
 \text{IMEP}(\text{bar}) = & 3,245 - 0,215X_1 - 0,63X_2 - 0,566X_3 - 0,13X_1X_2 \\
 & - 0,068X_1X_3 - 0,395X_2X_3 + 0,676X_1^2 - 0,216X_2^2 \\
 & - 0,077X_1X_2X_3 + 0,229X_1^2X_2 + 0,458X_1^2 + 0,128X_1X_2^2 \\
 & + 0,231X_2^2X_3 + 0,177X_1^2X_2X_3 + 0,161X_1X_2^2X_3
 \end{aligned} \tag{8}$$

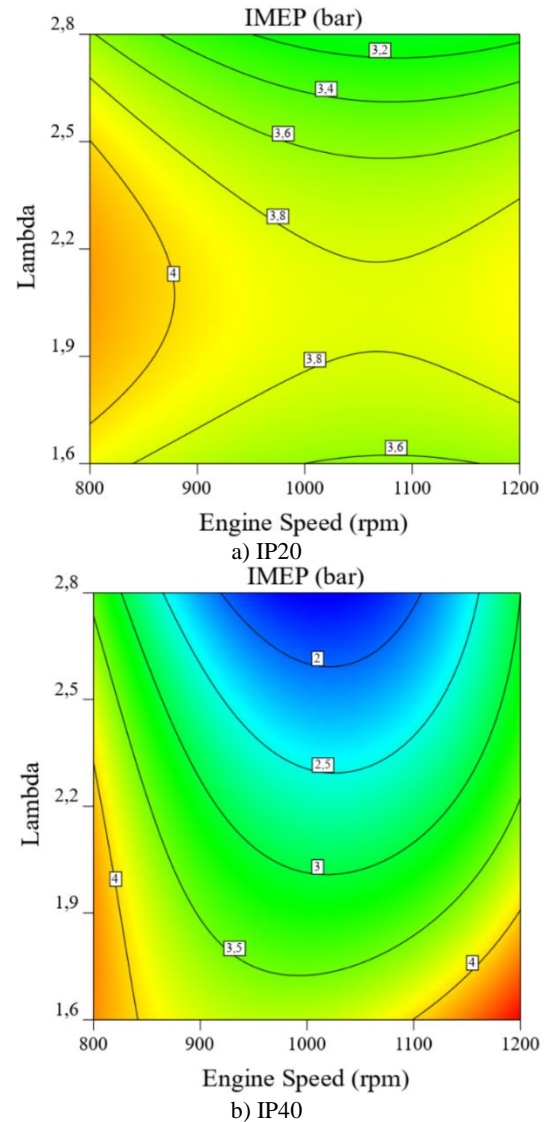


Figure 3. Effect of lambda and engine speed on indicated mean effective pressure (IMEP) (a and b)

Figures 3a and 3b shows the effect of the air excess coefficient and engine speed on IMEP of the HCCI engine operating with IP20 and IP40 fuels, respectively. In both fuel types, the IMEP air excess coefficient was 1.6 and the lowest IMEP coefficient was obtained under 2.8. The engine could not be started in conditions where the air excess coefficient is lower than 1.6. The reason for this is that the

engine knocks due to the rich mixture of the fuel taken into the cylinder [28]. The conditions with an excess air coefficient of 1.6 to 2.8 indicate the operating range in HCCI engines for n-heptane isopropanol mixture fuel. At values where the excess air coefficient is higher than 2.8, the combustion in the HCCI engine could not be fully achieved because the engine did not work properly. Combustion slows down as the octane number of the fuel obtained by mixing isopropanol with n-heptane fuel increases [18, 29].

**4.1.3. Maximum pressure rise rate (MPRR)**

ANOVA results for maximum pressure rise rate (MPRR) is showed the statistical values of this study are shown in Table 9. According to the ANOVA results, it is seen that the model is significant and important in terms of MPRR. The p-value measuring the effect of the model formed by the air excess coefficient and fuel type on the maximum pressure increase rate is below 0.05. However, the p-value of the engine speed is above 0.05. So the engine speed has a non-significant effect on the MPRR. These values also show that the change of the maximum pressure increase rate does not depend on the engine speed. When the ANOVA analysis is examined, the air excess coefficient has the highest F-value among the other two input parameters. In this case, it is seen that the air excess coefficient is effective on the MPRR.

Table 9. ANOVA table for maximum pressure rise rate (MPRR)

Source	Sum of Sq.	Mean S q.	F-value	p-value	Remarks
Model	439,02	27,44	79,25	< 0.0001	significant
X <sub>1</sub> - Engine speed	0,9487	0,9487	2,74	0,1322	not significant
X <sub>2</sub> -Lambda	89,7	89,7	259,08	< 0.0001	significant
X <sub>3</sub> -Fuel	7,46	7,46	21,55	0,0012	significant
Residual	3,12	0,3462			
Cor Total	442,14				

About the maximum pressure rise rate (MPRR), the correlation coefficient R<sup>2</sup> was 0.9930 and the adjusted correlation coefficient R<sup>2</sup> (Adj. R<sup>2</sup>) was 0.9804. It was seen that the correlation values were within acceptable boundary conditions. The quartic model Eq. (9) for maximum pressure rise rate generated by the response surface method.

$$\begin{aligned}
 \text{MPRR}(\text{bar}/^\circ\text{CA}) = & 2,04 - 4,736X_2 - 0,802X_3 + 0,86X_1X_2 \\
 & + 1,337X_1^2 + 3,726X_2^2 + 0,606X_1X_2X_3 \\
 & - 1,378X_1^2X_3 - 1,238X_1^2X_2^2 + 1,974X_1^2X_2X_3
 \end{aligned}
 \tag{9}$$

Figures 4a and 4b show the effect of IP20 and IP40 fuels on maximum pressure rise rate, respectively. A decrease was observed in MPRR values with the increase of excess air in both fuels. Reason for this is that the amount of fuel taken into the cylinder is reduced due to the lean mixture caused by the excess air. In addition, the MPRR value of IP40 fuel is lower than IP20. This is because high octane fuel slows down the combustion [19, 29, 30]. In the experiments conducted with IP40 fuel, the lowest maximum pressure rate was measured as 0.84 bar/°CA at 2.8 air excess coefficient at 1200

rpm. Under the same conditions, the maximum pressure rise rate of IP20 fuel was found to be 1.34 bar/°CA, which is the lowest MPRR value among the measured values in IP20 fuel. Although the low MPRR value is aimed for internal combustion engines, it is seen that it is at an acceptable level up to 10 bar/°CA [31].

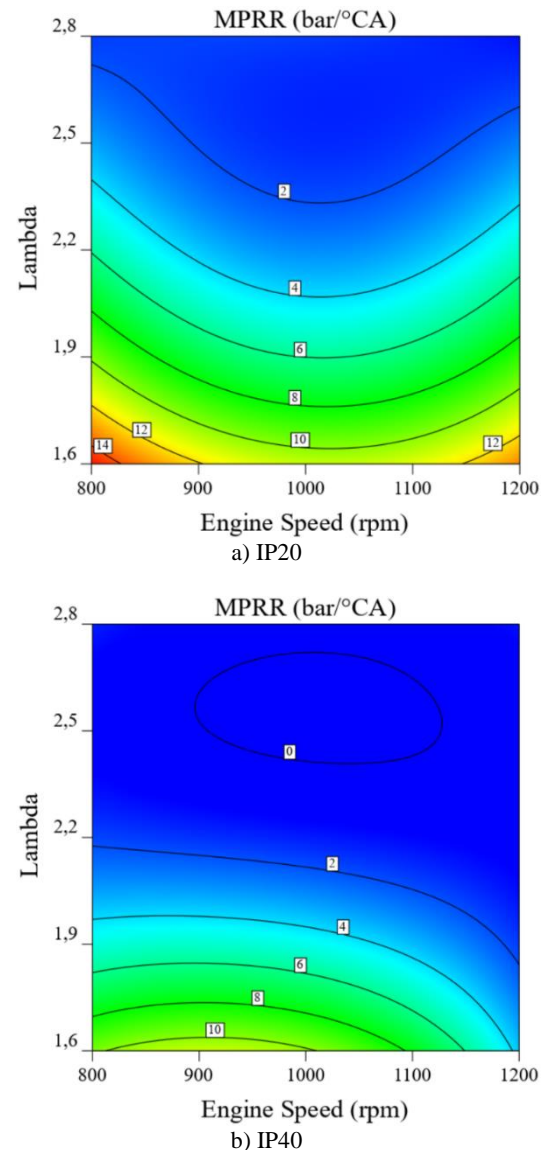


Figure.4. Effect of lambda and engine speed on maximum pressure rise rate (MPRR) (a and b)

**4.1.4. COV<sub>IMEP</sub>**

ANOVA results with COV<sub>IMEP</sub> values are given in Table 10. As seen in the ANOVA table, the effect of engine speed, air excess coefficient and fuel type on COV<sub>IMEP</sub> is significant. When the table was examined, it was seen that the model was meaningful. The p-value of the model and all input parameters is less than 0.0001. When the ANOVA table is examined according to the F-value, it is seen that the air excess coefficient is more important on COV<sub>IMEP</sub> than the others.

Table 10. ANOVA table for COVIMEP (%)

Source	Sum of Sq.	Mean Sq.	F-value	p-value	Remarks
Model	64,58	4,04	484,94	< 0.0001	significant
X <sub>1</sub> - Engine speed	3,79	3,79	455,73	< 0.0001	significant
X <sub>2</sub> -Lambda	13,08	13,08	1571,91	< 0.0001	significant
X <sub>3</sub> -Fuel	11,19	11,19	1344,77	< 0.0001	significant
Residual	0,0749	0,0083			
Cor Total	64,65				

The coefficient R<sup>2</sup> of the model created for COVIMEP was 0.9988 and the adjusted correlation coefficient R<sup>2</sup> (Adj. R<sup>2</sup>) value was 0.9968. These results show that the created model is congruent. The quartic model Eq. (10) generated by the response surface method for COV<sub>IMEP</sub>:

$$\begin{aligned}
 COV_{IMEP}(\%) = & 3,987 + 0,974X_1 + 1,809X_2 + 0,982X_3 \\
 & + 0,341X_1X_2 + 0,874X_1X_3 + 0,524X_2X_3 \\
 & - 0,971X_1^2 + 0,348X_2^2 - 1,228X_1^2X_2 + 0,163X_1^2X_3 \\
 & - 0,658X_1X_2^2 - 0,745X_2^2X_3 + 1,623X_1^2X_2^2 \\
 & + 0,641X_1^2X_2X_3 - 0,563X_1X_2^2X_3
 \end{aligned} \quad (10)$$

Figures 5a and 5b show COVIMEP values of IP20 and IP40 fuels, respectively. The charts are based on the excess air rate and engine speed. An increase in COVIMEP values was observed with the increase of excess air in the use of both types of fuels. This increase causes an increase in the probability of engine knock. In addition, the increase in the amount of isopropanol in the fuel caused an increase in the COVIMEP value. The reason for this is that the octane number slows down the combustion and causes the combustion process to be delayed. Also, the latent heat of vaporization of isopropanol is higher than n-heptane, causing an additional delay of combustion [19, 32]. Under these conditions where the engine speed is 1200 rpm and the excess air ratio is 2.8, approximately 8% COVIMEP value was obtained with IP40 fuel and approximately 4.40% with IP20 fuel. The maximum value of COVIMEP should not exceed the 10% threshold [33].

**4.1.5. CA10**

ANOVA results with CA10 values are given in Table 11. As seen in the ANOVA table, the p-value of the input parameters is less than 0.05. This shows that the effect of engine speed, air excess coefficient and fuel type for CA10 value is significantly important. The p-value of the created model is less than 0.0001. Considering the F-value, it is seen that the input parameters with a high effect are excess air ratio, fuel and engine speed, respectively.

The correlation coefficient (R<sup>2</sup>) of the model created for CA10 (°) was 0,9994 and the adjusted correlation coefficient R<sup>2</sup> (Adj. R<sup>2</sup>) value was 0,9984. These results show that the created model is congruent. The quartic model Eq. (11) for CA10 (°) generated by the response surface method.

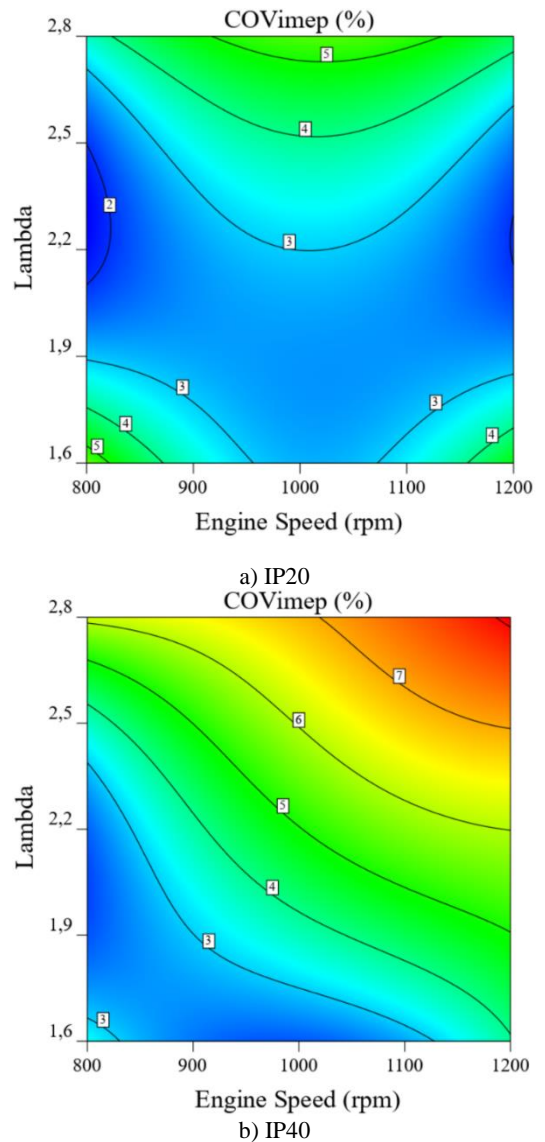


Figure 5. Effect of lambda and engine speed on COV<sub>IMEP</sub>(a and b)

$$\begin{aligned}
 CA10(°) = & 2,88 - 0,27X_1 + 2,82X_2 + 1,407X_3 - 0,63X_1X_2 \\
 & - 0,45X_1X_3 + 0,96X_2X_3 + 0,27X_1^2 - 1,56X_2^2 \\
 & - 0,18X_1X_2X_3 - 0,66X_1^2X_2 + 0,206X_1^2X_3 \\
 & + 0,54X_1X_2^2 - 0,304X_2^2X_3 + 0,57X_1^2X_2^2 \\
 & - 0,51X_1^2X_2X_3 + 0,27X_1X_2^2X_3
 \end{aligned} \quad (11)$$

Figures 6a and 6b shows the start of combustion (SOC) in HCCI engine with use of IP20 and IP40 test fuels, respectively. The graphs are based on the excess air rate and engine speed. In internal combustion engines, the crank angle position corresponding to different percentages of heat dissipation in the cylinder (10%, 50% and 90%) are expressed as CA10, CA50 and CA90, respectively. The crank angle position (CA10) corresponding to a heat dissipation of 10% is considered to be the SOC. The start of combustion in HCCI combustion depends on the chemical kinetics and the pressure-temperature history in the combustion chamber [34]. shows. For this reason, the combustion starts at earlier crank angles. It is seen that the start of the combustion is delayed for all test fuels with the depletion of

the mixture, ie the increase in the excess air coefficient. The main reason for this is the low reactivity of the mixture at high air excess coefficient values [28] (lambda 2.2 and engine speed 1000 rpm). IP20 fuel starts combustion 1.44°CA after TDC, and IP40 fuel starts to burn only 4.32°CA after TDC.

Table 11. ANOVA table for CA10 (°)

Source	Sum of Sq.	Mean Sq.	F-value	p-value	Remarks
Model	138,17	8,64	978,24	< 0.0001	significant
X <sub>1</sub> - Engine speed	0,2916	0,2916	33,03	0,0003	significant
X <sub>2</sub> -Lambda	31,81	31,81	3603,43	< 0.0001	significant
X <sub>3</sub> -Fuel	22,96	22,96	2601	< 0.0001	significant
Residual	0,0794	0,0088			
Cor Total	138,25				

4.1.6. CA50

ANOVA results with CA50 values are given in Table 12. As seen in the ANOVA table, the effect of the engine speed (p-value = 0.0714) is not significant, while the effect of the air excess coefficient and fuel type on the model, whose p-value is less than 0.05 which is significant. However, the generally created model is meaningful. The p-value of the created model is less than 0.0001. Considering the F-value, it is seen that the fuel type is more effective than other input parameters.

Table 12. ANOVA table for CA50 (°)

Source	Sum of Sq.	Mean Sq.	F-value	p-value	Remarks
Model	437,39	27,34	55,05	< 0.0001	significant
X <sub>1</sub> - Engine speed	2,07	2,07	4,18	0,0714	not significant
X <sub>2</sub> -Lambda	49,28	49,28	99,25	< 0.0001	significant
X <sub>3</sub> -Fuel	175,69	175,69	353,82	< 0.0001	significant
Residual	4,47	0,4966			
Cor Total	441,86				

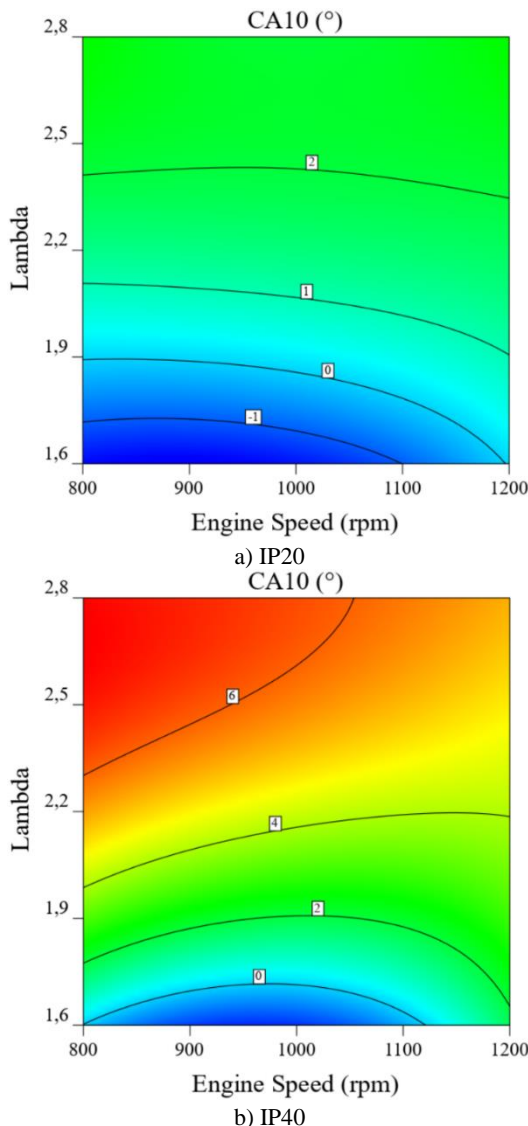
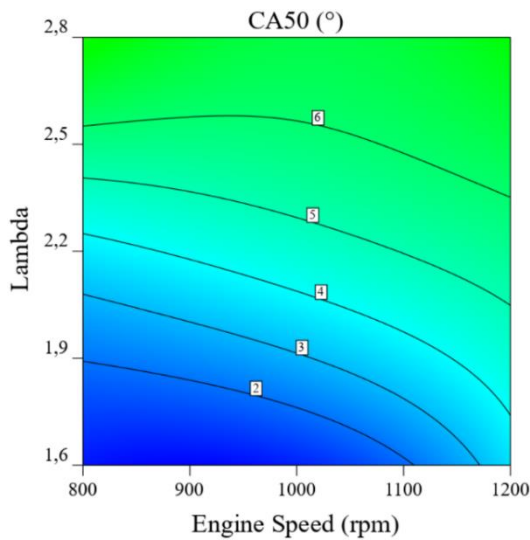


Figure 6. Effect of lambda and engine speed on CA10(a and b)

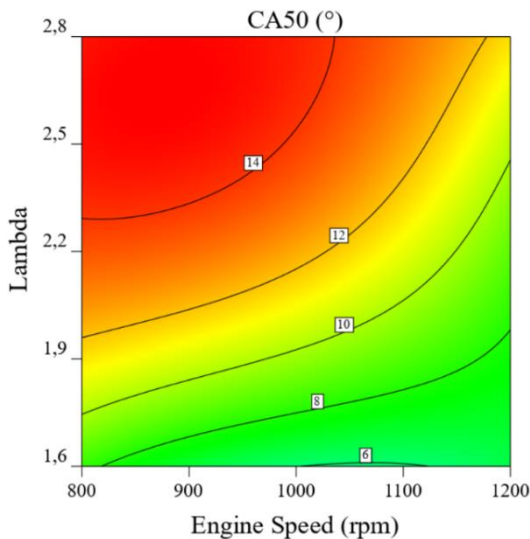
The correlation coefficient (R2) of the model created for CA50 (°) was 0.9899 and the adjusted correlation coefficient R2 (Adj. R2) value was 0.9719. These results show that the created model is congruent. The quartic model Eq. 12 for CA50 (°) by the response surface method.

$$CA50(°)=8,46+3,51X_2+3,89172X_3-1,62X_1X_3-1,53X_2^2 \quad (12)$$

Figures 7a and 7b show the crank angle CA50 values at which 50% of the cumulative heat dissipation occurs for HCCI combustion in the use of IP20 and IP40 test fuels, respectively, and the location of the CA50 significantly affects the thermal efficiency. The octane number is increasing and the fuel is more difficult to evaporate. With the increase in the amount of isopropanol in the fuel mixture, the combustion degree is delayed. The situation that causes this is, as the mixture becomes leaner, the reaction rate decreases and the combustion slows down. Accordingly, the CA50 is delayed [35, 36]. CA50 value, which represents the crankshaft angle at which 50% of the combustion occurs, should occur when the piston exceeds TDC by 7-11 °CA [37]. It is seen that the CA50 values are lower in the use of IP20 fuel mixture compared to the use of the IP40 fuel mixture, because the resistance to combustion increases with the increase of isopropanol concentration in the fuel.



a) IP20



b) IP40

Figure 7. Effect of lambda and engine speed on CA50(a and b)

4.1.7. CA10-CA90

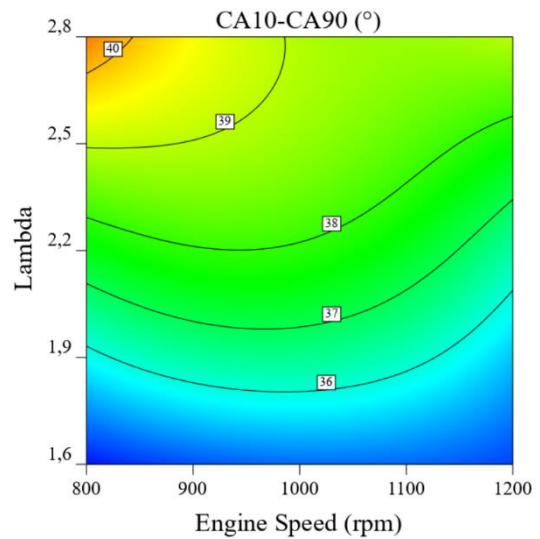
ANOVA results with CA10-CA90 values are given in Table 13. As seen in the ANOVA table, the p-value of all input parameters is less than 0.05. Generally, the created model is meaningful. The p-value of the created model is less than 0.0001. Considering the F-value, it is seen that the excess air coefficient is more effective than the other input parameters.

The correlation coefficient (R2) of the model created for CA10-CA90 (°) was 0.9919 and the adjusted correlation coefficient R2 (Adj. R2) value was 0.9776. Since the difference between them is less than 0.02, it shows that the created model is compatible. The quartic model Eq.13 for CA10-CA90 (°) generated by the response surface method.

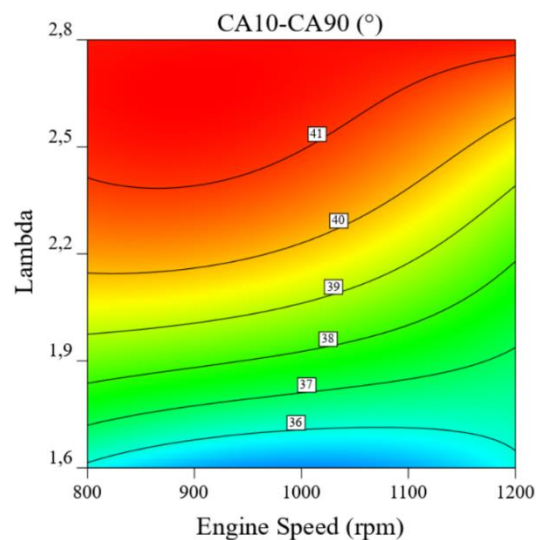
$$CA10-CA90(°) = 38,88 - 0,81X_1 + 2,7X_2 + 0,962069X_3 + 0,54X_2X_3 - 0,81X_1^2 - 1,44X_2^2 + 0,675X_1X_2^2 + 1,125X_1^2X_2^2 - 0,585X_1^2X_2X_3 \quad (13)$$

Table 13. ANOVA table for CA10-CA90 (°)

Source	Sum of Sq.	Mean Sq.	F-value	p-value	Remarks
Model	124,17	7,76	69,27	< 0.0001	significant
X <sub>1</sub> - Engine speed	2,62	2,62	23,42	0,0009	significant
X <sub>2</sub> -Lambda	29,16	29,16	260,28	< 0.0001	significant
X <sub>3</sub> -Fuel	10,74	10,74	95,83	< 0.0001	significant
Residual	1,01	0,112			
Cor Total	125,17				



a) IP20



b) IP40

Figure 8. Effect of lambda and engine speed on CA10-90(a and b)

Combustion duration (CD) is named as CA10-CA90 in combustion analysis. Figures 8a and 8b show the combustion durations of the IP20 and IP40 test fuels, respectively, CA10 indicates the point

where 10% of the cumulative heat release emerges (also the beginning of the combustion), while CA90 indicates the point where 90% of the cumulative heat release emerges in combustion analysis and the combustion is finished. It is considered as the moment [6]. CA10-CA90 expresses the combustion duration as the crank angle. As the fuel rich mixture taken into the cylinder, the combustion duration has decreased. Therefore, the combustion duration was shorter in the tests with low excess air coefficient. In addition, the increase in the octane number of the fuel increased the combustion duration. Increasing the octane number delays low and high temperature oxidation zones in HCCI combustion and causes the negative temperature zone to expand [38]. Therefore, the combustion duration of IP40 fuels took longer than IP20 fuels. In the experiment performed with 2.8 air excess coefficient and 800 rpm using IP40 fuel, the highest combustion duration (41.4 °CA) was realized, while the lowest combustion duration (33.84 °CA) IP20 fuel was 1.6 air excess coefficient and 800 rpm. has also been realized.

**4.1.8. Indicated thermal efficiency**

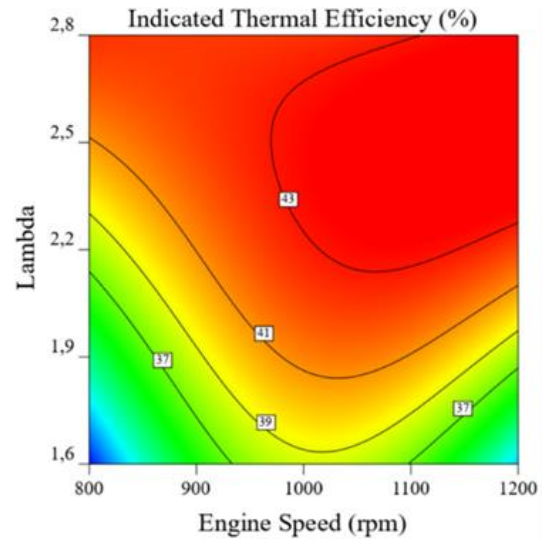
ANOVA results obtained for the indicated thermal efficiency are given in Table 14. As seen in the ANOVA table, the model created is meaningful and significant (p-value <0.0001). Among the input parameters, engine speed and fuel type p-value is less than 0.05. While the effect of engine speed and fuel type on the indicated thermal efficiency is high, the air excess coefficient is not significant. When the F-value is examined, it is seen that the fuel type has a more important effect than the other input parameters.

Table 14. ANOVA table for indicated thermal efficiency (%)

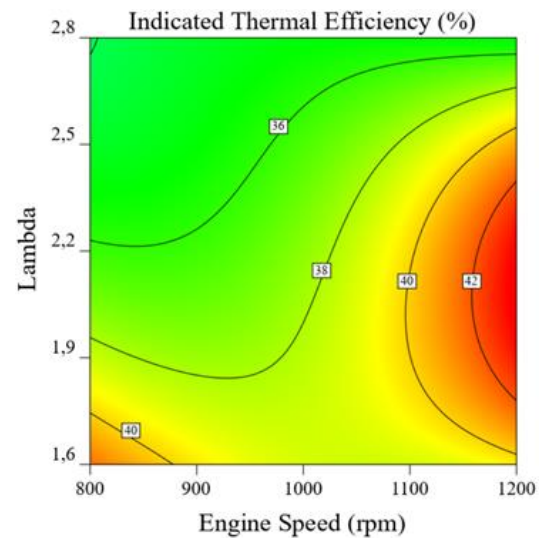
Source	Sum of Sq.	Mean Sq.	F-value	p-value	Remarks
Model	444,84	27,8	71,2	< 0.0001	significant
X1- Engine speed	34,16	34,16	87,49	< 0.0001	significant
X2 -Lambda	0,0462	0,0462	0,1184	0,7387	not significant
X3 -Fuel	83,95	83,95	214,98	< 0.0001	significant
Residual	3,51	0,3905			
Cor Total	448,36				

The correlation coefficient (R2) of the model created for the indicated thermal efficiency (%) was 0.9922 and the adjusted correlation coefficient R2 (Adj. R2) was 0.9782. Since the difference between them is less than 0.02, it shows that the created model is compatible. The quartic model Eq. 14 for the Indicated thermal efficiency (%) by the response surface method.

$$\eta_{ITE}(\%)=40,16+2,923X_1-2,690X_3-1,883X_2X_3-1,438X_2^2+0,621X_1X_2X_3+1,909X_1^2X_2+2,583X_1^2X_3-2,556X_1X_2^2+0,853X_2^2X_3-1,731X_1^2X_2^2-3,204X_1^2X_2X_3-1,334X_1X_2^2X_3 \quad (14)$$



a) IP20



b) IP40

Figure 9. Effect of lambda and engine speed on indicated thermal efficiency(a and b)

Figures 9a and 9b show the indicated thermal efficiency values depending on the air excess coefficient and engine speed of the IP20 and IP40 test fuels, respectively. In the use of IP20 fuel, the occurrence of CA50 just after TDC has increased the indicated thermal efficiency. The highest indicated thermal efficiency for IP20 fuel was realized at 1200 rpm motor speed with an air excess coefficient of 2.8 and the CA50 7.02°CA after TDC. The indicated thermal efficiency here was 43.35%. In the use of IP40 test fuel, the indicated thermal efficiency was lower than the IP20 test fuel because most of the combustion occurred in the expansion time. While the indicated thermal efficiency was 41.87% under conditions where CA50 was realized 8.64 °CA after TDC, it was realized 14.76 °CA after TDC

CA50 in operating conditions where the air excess coefficient was 2.8 at 800 rpm engine speed as a result of the depletion of the mixture. As a result of this situation, it caused the indicated thermal efficiency to decrease up to 34.21%.

**4.2. Interaction Effects of Exhaust Emissions**

**4.2.1. Unburned hydrocarbon emissions (UHCs)**

ANOVA results for unburned hydrocarbon emissions are shown in Table 15. As seen in the ANOVA table, the model created is meaningful and significant (p-value <0.0001). The input parameters of engine speed, air excess coefficient and fuel type p-value are less than 0.05. All intake parameters have an impact on unburned hydrocarbon emissions. When analysed in terms of F-value, it is seen that engine speed has a more important effect than the other two input parameters.

Table 16. ANOVA table for unburned hydrocarbon emissions (ppm)

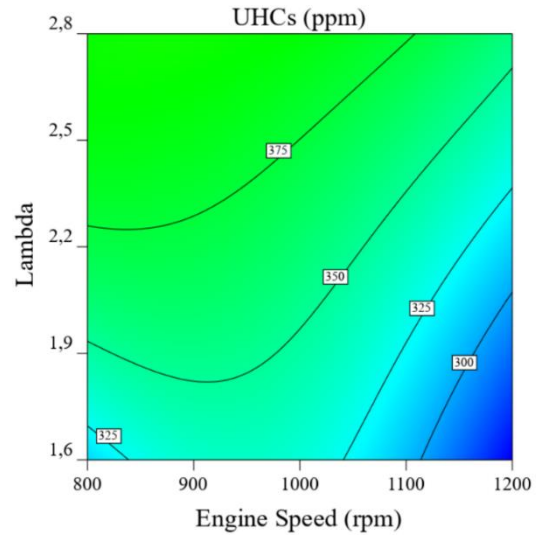
Source	Sum of Sq.	Mean Sq.	F-value	p-value	Remarks
Model	69865,27	4366,58	324,17	< 0.0001	significant
X <sub>1</sub> - Engine speed	7744	7744	574,91	< 0.0001	significant
X <sub>2</sub> -Lambda	3844	3844	285,38	< 0.0001	significant
X <sub>3</sub> -Fuel	1001,8	1001,8	74,37	< 0.0001	significant
Residual	121,23	13,47			
Cor Total	69986,5				

The correlation coefficient (R2) of the model created for unburned hydrocarbon emissions (ppm) was 0.9983 and the adjusted correlation coefficient R2 (Adj. R2) was 0.9952. This result shows that the created model is compatible. The quartic model Eq. 15 for unburned hydrocarbon emissions (ppm) generated by the response surface method:

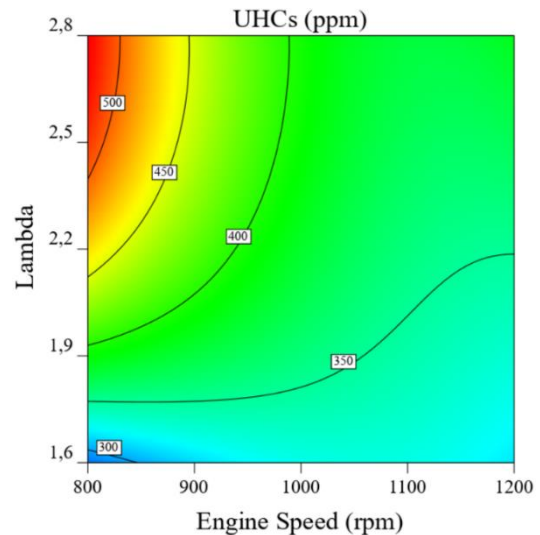
$$\begin{aligned}
 \text{UHCs(ppm)} = & 370 - 44X_1 + 31X_2 + 9,293X_3 - 19,125X_1X_2 - 14X_1X_3 + 5X_1^2 - 8,5X_2^2 \\
 & - 24,875X_1X_2X_3 + 30,375X_1^2X_2 + 24,474X_1^2X_3 + 17,875X_1X_2^2 \\
 & - 9,026X_2^2X_3 - 12,625X_1^2X_2^2 + 12,625X_1^2X_2X_3 + 12,125X_1X_2^2X_3
 \end{aligned}
 \tag{15}$$

HC emissions occur as an incomplete combustion product. Among the reasons for the formation of HC emissions, incomplete combustion air-fuel mixture in the regions close to the cylinder walls and the occurrence of incomplete combustion, especially at low engine speeds, depending on the operating conditions of the engine [39]. In HCCI engines, UHCs emissions are similar to those of the SI engine. In particular, UHCs emissions occur as a result of HCCI combustion at low temperature [40]. Figures 10a and 10b show the air excess coefficient of the IP20 and IP40 test fuels in the HCCI engine and unburned hydrocarbon values depending on the engine speed, respectively. As the air excess coefficient increases, it is seen that HC emissions increase all fuels [41]. This is because the amount of energy released as a result of combustion and the gas temperatures

at the end of the combustion decrease with the depletion of the mixture. As the amount of isopropanol in the mixture fuels increased, HC emissions increased, the reason for this is the expansion of the volume as a result of the shift of the combustion to the expansion time and the slowdown of in-cylinder oxidation reactions. Comparing the results of the experiments conducted under the same conditions under the same conditions at 1200 rpm engine speed, the test results were 308 ppm in the IP20 test fuel, while it increased 14% in the IP40 test fuel and became 354 ppm.



a) IP20



b) IP40

Figure 10. Effect of lambda and engine speed on UHCs(a and b)

**4.2.2. Carbon monoxide emissions (CO)**

ANOVA results for carbon monoxide emissions are shown in Table 17. As seen in the ANOVA table, the model created is meaningful and significant (p-value <0.0001). The air excess coefficient and fuel type p-value, which are the inlet parameters, are less than 0.05. However, the p-value of the engine speed is over 0.05. Therefore, engine speed has no effect on carbon monoxide emissions. When

examined in terms of the F-value, it is seen that the air excess coefficient has a more important effect.

Table 17. ANOVA table for carbon monoxide emissions (%)

Source	Sum of Sq.	Mean Sq.	F-value	p-value	Remarks
Model	0,2395	0,015	39,65	< 0.0001	significant
X <sub>1</sub> - Engine speed	0,0019	0,0019	5,01	0,0519	not significant
X <sub>2</sub> -Lambda	0,0588	0,0588	155,81	< 0.0001	significant
X <sub>3</sub> -Fuel	0,0231	0,0231	61,29	< 0.0001	significant
Residual	0,0034	0,0004			
Cor Total	0,2429				

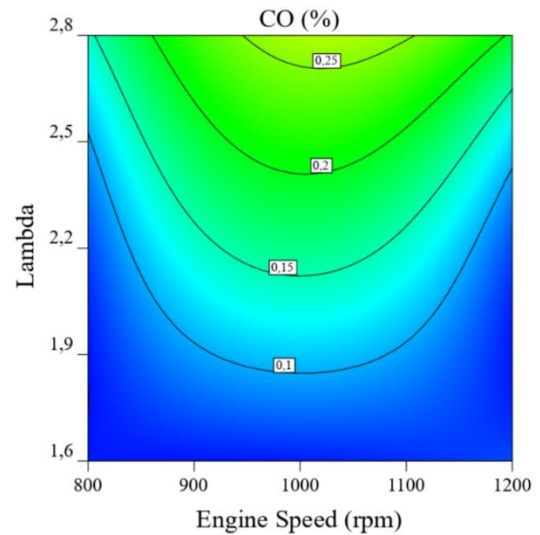
The correlation coefficient (R2) of the model created for carbon monoxide emissions (%) was 0.9860 and the adjusted correlation coefficient R2 (Adj. R2) value was 0.9661. This result shows that the created model is compatible. The quartic model Eq. (16) for carbon monoxide emissions (%) generated by the response surface method:

$$CO(\%)=0,209+0,121X_2+0,045X_3-0,082X_1^2+0,054X_1^2X_2^2-0,028X_1X_2^2X_3 \quad (16)$$

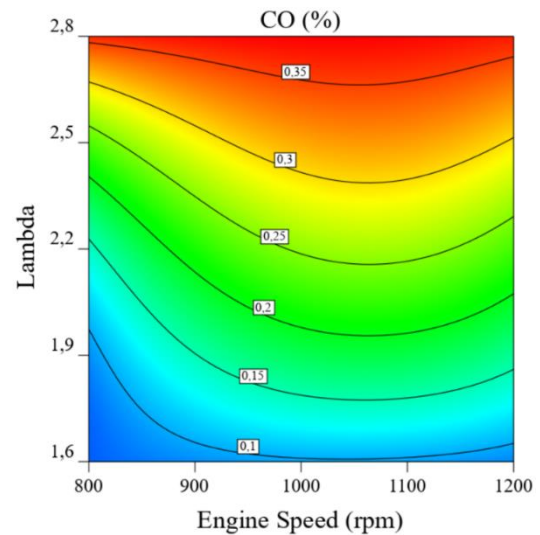
CO emissions are a type of emission that occurs when there is not enough oxygen in the cylinder or when oxidation reactions are disrupted due to low temperature. As can be seen from the ANOVA table, CO emissions are sensitively affected by the changes in the excess air coefficient. CO emissions are constantly increasing under rich mixture conditions where the excess air coefficient is low. However, even if there is sufficient oxygen in the cylinder under extremely lean mixing conditions, CO emissions increase again due to the low gas temperatures in the cylinder. The low temperature inside the cylinder prevents the conversion of CO to CO<sub>2</sub> [6, 42]. Figures 11a and 11b, show the air excess coefficient of the IP20 and IP40 test fuels in the HCCI engine and carbon monoxide emission values depending on the engine speed, respectively. CO emissions increased with the depletion of the mixture in both test fuels. Comparing the results of the experiments conducted under the same conditions at an engine speed of 2200 rpm, the test results were 0.084% in the IP20 test fuel and 0.212% in the IP40 test fuel.

#### 4.2.3. Nitrogen oxide emissions (NO<sub>x</sub>)

ANOVA results for nitrogen oxide emissions are shown in Table 18. As seen in the ANOVA table, the model created is meaningful and important (p-value <0.0001). The p-value of the air excess coefficient for the input parameter is less than 0.05. However, the p-value of the engine speed and fuel type is over 0.05. Therefore, fuel type and engine speed have no effect on nitrogen oxide emissions.



a) IP20



b) IP40

Figure 11. Effect of lambda and engine speed on CO(a and b)

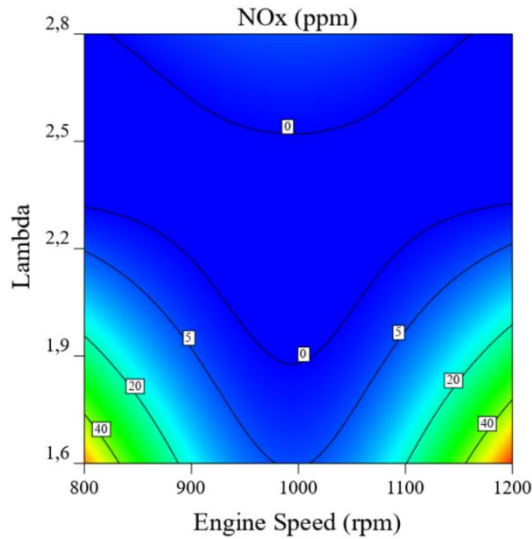
Table 18. ANOVA table for nitrogen oxide emissions (ppm)

Source	Sum of Sq.	Mean Sq.	F-value	p-value	Remarks
Model	9691,83	605,74	21,29	< 0.0001	significant
X <sub>1</sub> - Engine speed	0	0	0	10.000	not significant
X <sub>2</sub> -Lambda	169	169	5,94	0,0375	significant
X <sub>3</sub> -Fuel	40,97	40,97	1,44	0,2608	not significant
Residual	256,06	28,45			
Cor Total	9947,88				

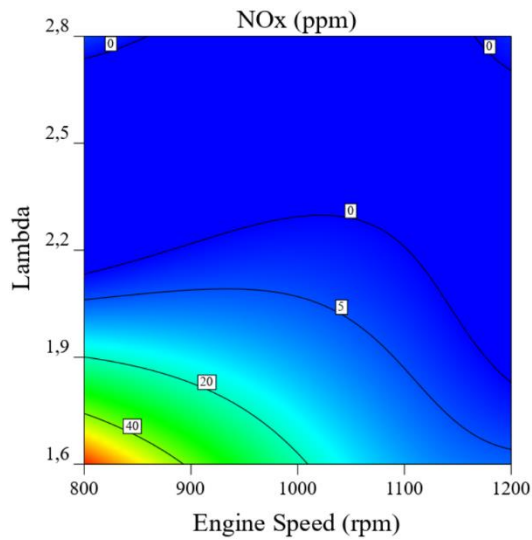
The correlation coefficient (R2) of the model created for nitrogen

oxide emissions (ppm) was 0.9743 and the adjusted correlation coefficient R2 (Adj. R2) was 0.9285. This result shows the created model within the boundaries. The quartic model Eq. (17) for nitrogen oxide emissions (ppm) generated by the response surface method:

$$\begin{aligned}
 NO_x(\text{ppm}) = & -6,5X_2 + 5,875X_1X_2 - 6,5X_2X_3 \\
 & + 7,625X_1X_2X_3 - 16,375X_1^2X_2 \\
 & - 6,578X_1^2X_3 + 16,63X_1^2X_2^2 \\
 & + 13,88X_1^2X_2X_3 - 7,38X_1X_2^2X_3
 \end{aligned}
 \tag{17}$$



a) IP20



b) IP40

Figure 12. Effect of lambda and engine speed on NOx(a and b)

Reason for NOx emission formation is that the end-of-combustion temperature exceeds approximately 2073 K [43]. Figures 12a and 12b show the nitrogen oxide emission values of the IP20 and IP40 test fuels, respectively, depending on the HCCI engine air excess co-

efficient and engine speed. The reason for this is that the gas temperature in the cylinder is high, as the rich mixture has a better combustion and oxidation rate. However, it is seen that the amount of NOx emission decreases when the excess air ratio and engine speed values increase in both test fuels.

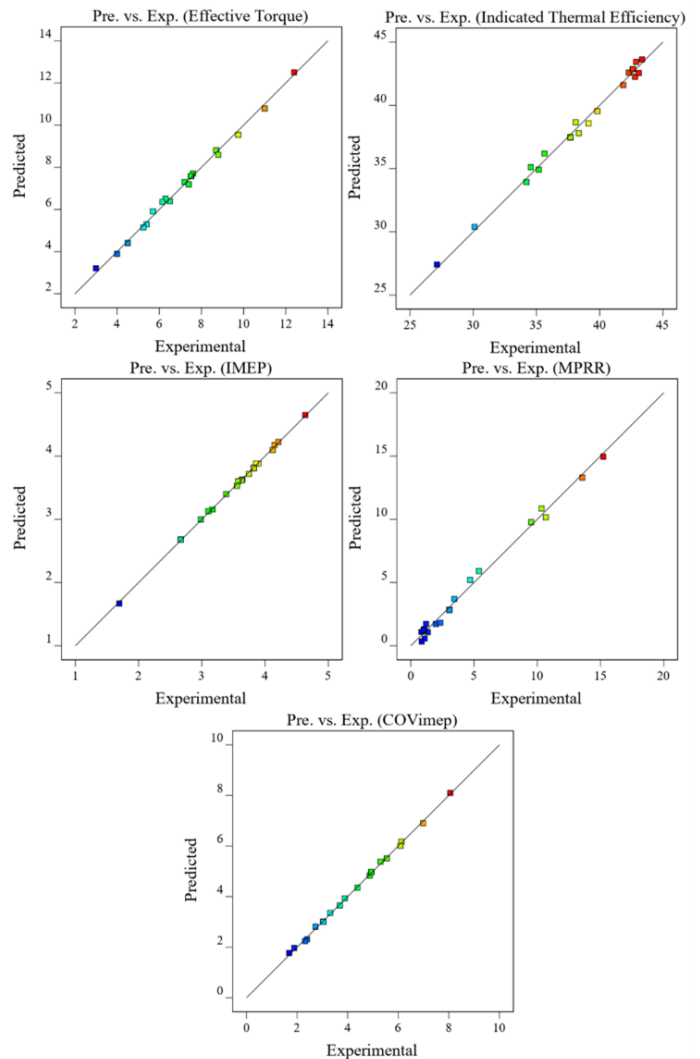


Figure 13. Predicted and Experimental values of Effective Torque, ITE, IMEP, MPRR, COV<sub>IMEP</sub>

### 4.3. Optimization and Validation

In this study, engine speed, excess air coefficient and fuel type are used as input parameters. The response values predicted with the experimental data obtained in line with the experiments performed were optimized and verified. Optimization was made with the response surface methodology and the Design Expert 12 program was used. When the values shown in Fig. 13 and Fig. 14 are examined, the experimental data and the estimated data are almost exactly the same. Considering these results, it is seen that the model created is successful. The deviations in the graphs are quite low, since the R2 and adjusted R2 correlation values are in appropriate intervals in all responses. The high correlation values and the close experimental and estimated data proves the accuracy of the quartic equation used

in the model.

As a result of the response surface methodology optimization, it is concluded that the optimum operating parameters are an engine speed of 1200 rpm and an excess air ratio of 1.725 by using IP40test fuel. Response parameters under optimum operating conditions Effective Torque 11.438 Nm, IMEP 4.366 bar, MPRR 2.747 bar/°CA, COVIMEP 4.364%, CA10 2.315 °CA, CA50 7 °CA, CA10-CA90 36.245 °CA, UHCs 324.562 ppm, CO 0.0118% and NOx 2.549 ppm were determined. The results obtained in the MPRR, COVIMEP and CA50 responses were within the target range. The desirability value of this optimization was found to be 0.857. The fact that the result is close to 1.000 shows that the optimization made is compatible with the experimental study.

In order to run the engine's responses with the desired data, the optimum input parameters must be determined. One of the most important factors in determining the optimum input parameters is the establishment of optimization criteria. Optimization criteria are given in Table 19. The input parameter values were determined as 800-1200 rpm for the motor speed, 1.6 - 2.8 for the excess air ratio value and 20% and 40% for the isopropanol density in the heptane (IP20-IP40). Among the targeted response parameters, IMEP, effective torque and thermal efficiency values are aimed to be maximum, while HC, CO and NOx emission values are aimed to be minimum. MPRR values are at acceptable levels between 1 - 8 (bar/°CA) and COVIMEP values are 1 - 6 (%) It is aimed that the CA50 value, which directly affects the effective torque and the indicated thermal efficiency value, is between 7 - 11 (°CA).

Table 19. Respond Surface Methodology optimization criteria

Parameter	Approach	Limits		Importance
		Lower	Upper	
Engine speed	in range	800	1200	3
Lambda	in range	1,6	2,8	3
Fuel	in range	20Izo	40Izo	3
Effective Torque	maximize	3	12,4	3
IMEP	maximize	1,69452	4,63569	3
MPRR	in range	1	8	3
COVimep	in range	1	6	3
CA10	none	-1,8	6,84	3
CA50	in range	7	11	3
CA10-CA90	none	33,84	41,4	3
Indicated Thermal Efficiency	maximize	27,14	43,35	3
HC	minimize	255	526	3
CO	minimize	0,044	0,371	3
NOx	minimize	0	64	3

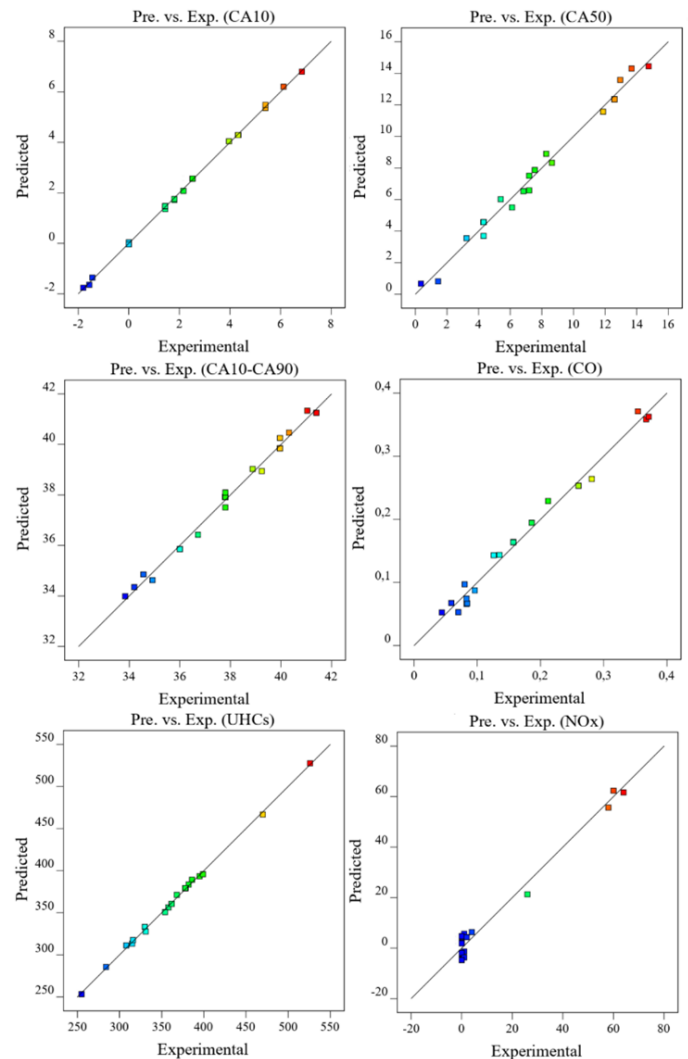


Figure 14. Predicted and Experimental values of CA10, CA50, CA10-CA90, UHCs, CO, NOx

## 5. Conclusions

The dates of manuscript received, revised and accepted will be In this study, the effect of isopropanol heptane mixture test fuels (IP20 and IP40) on combustion and exhaust emissions at constant intake air inlet temperature (60 °C) at different engine speed (800 rpm - 1200 rpm) and air excess coefficient (1.6 - 2.8) in an HCCI engine. The aim is to determine the optimum input parameters required to obtain the appropriate response parameters by analysing and optimizing with the response surface method. With this research, effective torque, indicated mean effective pressure, indicated thermal efficiency, maximum pressure increase rate, COVIMEP, CA10, CA50, CA10-CA90 values and HC, CO and NOx emissions were determined as response parameters. Engine speed, excess air ratio and isopropanol in fuel. It has been observed that the effective torque and the indicated thermal efficiency values increase with the increase of the input parameters. The increase in the input parameters caused the CA50 value to approach the targeted values. Also, the addition of isopropanol to n-heptane fuel caused the working range to narrow. The main reason for this is which, due to the high-octane number of

isopropanol, combustion is delayed and most of the heat dissipation occurs in the expansion time. The maximum effective torque value of the engine used was obtained as 12.4 Nm at 2.8 air excess coefficient at 1200 rpm by using IP40 test fuel. Maximum indicated thermal efficiency value in IP20 test fuel use was found as 43.35% at 1200 rpm engine speed and 2.8 excess air ratio value conditions. When the value of indicated air pressure was examined, the maximum indicated air pressure value was found as 1.6 air excess coefficient at 1200 rpm using IP40 test fuel as 4.64 bar. For the maximum pressure rise rate (MPRR), as the air excess coefficient decreased, that is, as the mixture got richer, the maximum pressurise rate increased. The high-octane number of isopropanol slowed the combustion and kept the pressure increase rate below the critical level. At 1000 rpm conditions where the air excess coefficient is 1.6, the pressure increase rate of IP20 and IP40 fuels is approximately 10.52 bar/°CA, while IP20 and IP40 are 1.2095 bar/°CA and 0.8416 bar, respectively, when the air excess coefficient is 2.8 under the same conditions. While the COVIMEP value is higher in IP40 test fuel, it decreases in IP20 test fuel. In the use of IP20 test fuel, the start of combustion and started later than IP40 fuel. Due to its high-octane number, the place of CA50 in IP40 fuel starts later than IP20. The combustion duration is expressed with the CA10-CA90 value. In the use of IP40 test fuel, the combustion shifted to the expansion time and lasted quite long. With IP20 fuel, the highest indicated thermal efficiency was obtained at high air excess coefficient values. The highest indicated thermal efficiency was recorded as 43.35% in the use of IP20 fuel under conditions where the air excess coefficient at 1200 rpm is 2.8. Increasing the concentration of isopropanol in the test fuel mixture causes the combustion to shift mostly to the expansion time under lean mixture conditions. Therefore, the temperatures at the end of combustion decreased and CO and HC emissions increased simultaneously in engine speeds and fuel types with high air excess coefficient. NO<sub>x</sub> emission, which is generally measured as 0, has increased in the regions where the mixture is rich. It is seen that it is appropriate to use isopropanol as fuel in HCCI engines with high compression ratio. According to the optimization results of the experimental data, the desirability value was obtained as 0.857.

### Conflict of Interest Statement

The authors declare that there is no conflict of interest in this study.

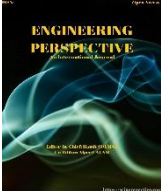
### CRediT Author Statement

**Seyed Mohammad Safieddin Ardebili:** Supervision, Methodology, Writing-original draft; **Çağatay Nacak:** Application of RSM, Writing-original draft; **Tolga Kocakulak:** Experimental set-up, Writing-original draft; **Mustafa Babagiray:** Experimental set-up, Conceptualization, Writing-original draft

### References

- Lü, X., Ji, L., Zu, L., Hou, Y., Huang, C., and Huang, Z. (2007) Experimental study and chemical analysis of n-heptane homogeneous charge compression ignition combustion with port injection of reaction inhibitors. *Combustion and flame*. 149(3): p. 261-270.
- Li, Y., Chen, Y., Wu, G., and Liu, J. (2018) Experimental evaluation of water-containing isopropanol-n-butanol-ethanol and gasoline blend as a fuel candidate in spark-ignition engine. *Applied Energy*. 219: p. 42-52.
- Polat, S., Solmaz, H., Yılmaz, E., Calam, A., Uyumaz, A., and Yücesu, H.S. (2020) Mapping of an HCCI engine using negative valve overlap strategy. *Energy Sources, Part A: Recovery, Utilization, and Environmental Effects*. 42(9): p. 1140-1154.
- Uyaroğlu, A., Gürü, M., Kocakulak, T., Uyumaz, A., and Solmaz, H. (2021) Combustion, performance and emission analyses of organic Manganese-Added *crambe abyssinica* biodiesel in a direct injection diesel engine. *Fuel*. 297: p. 120770.
- An, Y., Jaasim, M., Raman, V., Pérez, F.E.H., Sim, J., Chang, J., Im, H.G., and Johansson, B. (2018) Homogeneous charge compression ignition (HCCI) and partially premixed combustion (PPC) in compression ignition engine with low octane gasoline. *Energy*. 158: p. 181-191.
- Calam, A., Solmaz, H., Yılmaz, E., and İcingür, Y. (2019) Investigation of effect of compression ratio on combustion and exhaust emissions in A HCCI engine. *Energy*. 168: p. 1208-1216.
- Aydoğan, B. (2021) Combustion, Performance and Emissions of Ethanol/n-Heptane Blends in HCCI Engine. *Engineering Perspective*. 1(1): p. 5.
- Uyumaz, A., Aydoğan, B., Calam, A., Aksoy, F., and Yılmaz, E. (2020) The effects of diisopropyl ether on combustion, performance, emissions and operating range in a HCCI engine. *Fuel*. 265: p. 116919.
- Calam, A., Aydoğan, B., and Halis, S. (2020) The comparison of combustion, engine performance and emission characteristics of ethanol, methanol, fusel oil, butanol, isopropanol and naphtha with n-heptane blends on HCCI engine. *Fuel*. 266: p. 117071.
- Polat, S., Yücesu, H.S., Solmaz, H., Uyumaz, A., Kannan, K., and Shahbakhti, M. (2019) An Experimental Study on the Variation of COVIMEP and Ringing Intensity at Different Air Excess Coefficients in a HCCI Engine, in *International Symposium on Automotive Science and Technology-2019: Ankara, Turkey*.
- Solmaz, H., Ardebili, S.M.S., Calam, A., Yılmaz, E., and İpci, D. (2021) Prediction of performance and exhaust emissions of a CI engine fueled with multi-wall carbon nanotube doped biodiesel-diesel blends using response surface method. *Energy*. p. 120518.
- Bahng, G., Jang, D., Kim, Y., and Shin, M. (2016) A new technology to overcome the limits of HCCI engine through fuel modification. *Applied Thermal Engineering*. 98: p. 810-815.
- Elzahaby, A.M., Elkelawy, M., Bastawissi, H.A.-E., El Malla, S.M., and Naceb, A.M.M. (2018) Kinetic modeling and experimental study on the combustion, performance and emission characteristics of a PCCI engine fueled with ethanol-diesel blends. *Egyptian Journal of Petroleum*. 27(4): p. 927-937.
- Elkelawy, M., Yu-Sheng, Z., Hagar, A.E.-D., and Yu, J.-Z. (2008) Challenging and future of homogeneous charge compression ignition engines; an advanced and novel concepts review. *Journal of power and energy systems*. 2(4): p. 1108-1119.
- Taghavifar, H., Nemati, A., and Walther, J.H. (2019) Combustion and exergy analysis of multi-component diesel-DME-methanol blends in HCCI engine. *Energy*. 187: p. 115951.
- Bastawissi, H.A.E., Elkelawy, M., Panchal, H., and Sadasivuni, K.K. (2019) Optimization of the multi-carburant dose as an energy source for the application of the HCCI engine. *Fuel*. 253: p. 15-24.
- Gainey, B., Yan, Z., and Lawler, B. (2021) Autoignition characterization of methanol, ethanol, propanol, and butanol over a wide range of operating conditions in LTC/HCCI. *Fuel*. 287: p. 119495.

18. Uyumaz, A. (2015) An experimental investigation into combustion and performance characteristics of an HCCI gasoline engine fueled with n-heptane, isopropanol and n-butanol fuel blends at different inlet air temperatures. *Energy Conversion and Management*. 98: p. 199-207.
19. Calam, A. and Aydoğan, B. (2019) Experimental Investigation of Performance Combustion and Emission Characteristics in an HCCI Engine Fuelled Isopropanol and Heptane Fuel Mixtures. *Gazi Üniversitesi Fen Bilimleri Dergisi Part C*. 7(4): p. 818-833.
20. Awad, O.I., Mamat, R., Ali, O.M., Azmi, W., Kadirgama, K., Yusri, I., Leman, A., and Yusaf, T. (2017) Response surface methodology (RSM) based multi-objective optimization of fusel oil-gasoline blends at different water content in SI engine. *Energy Conversion and Management*. 150: p. 222-241.
21. Mahla, S.K., Safieddin Ardebili, S.M., Mostafaei, M., Dhir, A., Goga, G., and Chauhan, B.S. (2020) Multi-objective optimization of performance and emissions characteristics of a variable compression ratio diesel engine running with biogas-diesel fuel using response surface techniques. *Energy Sources, Part A: Recovery, Utilization, and Environmental Effects*. p. 1-18.
22. Calam, A., İcingür, Y., Solmaz, H., and Yamık, H. (2015) A comparison of engine performance and the emission of fusel oil and gasoline mixtures at different ignition timings. *International journal of green energy*. 12(8): p. 767-772.
23. Awad, O.I., Ali, O.M., Mamat, R., Abdullah, A., Najafi, G., Kamarulzaman, M., Yusri, I., and Noor, M. (2017) Using fusel oil as a blend in gasoline to improve SI engine efficiencies: A comprehensive review. *Renewable and Sustainable Energy Reviews*. 69: p. 1232-1242.
24. Myers, R.H., Montgomery, D.C., Vining, G.G., Borror, C.M., and Kowalski, S.M. (2004) Response surface methodology: a retrospective and literature survey. *Journal of quality technology*. 36(1): p. 53-77.
25. Myers, R.H., Khuri, A.I., and Carter, W.H. (1989) Response surface methodology: 1966-1988. *Technometrics*. 31(2): p. 137-157.
26. Xiao, M., Shen, X., Ma, Y., Yang, F., Gao, N., Wei, W., and Wu, D. (2018) Prediction of surface roughness and optimization of cutting parameters of stainless steel turning based on RSM. *Mathematical Problems in Engineering*. 2018.
27. Li, Y., Meng, L., Nithyanandan, K., Lee, T.H., Lin, Y., Chia-fon, F.L., and Liao, S. (2016) Combustion, performance and emissions characteristics of a spark-ignition engine fueled with isopropanol-n-butanol-ethanol and gasoline blends. *Fuel*. 184: p. 864-872.
28. Halis, S., Nacak, Ç., Solmaz, H., Yilmaz, E., and Yucesu, H.S. (2018) Investigation of the effects of octane number on combustion characteristics and engine performance in a HCCI engine. *Journal of Thermal Science and Technology*. 38(2): p. 73-84.
29. Calam, A. and İcingür, Y. (2019) Hava fazlalık katsayısı ve oktan sayısı değişiminin HCCI yanma karakteristiklerine ve motor performansına etkileri. *Politeknik Dergisi*. 22(3): p. 607-618.
30. Xingcai, L., Yuchun, H., Libin, J., Zu Linlin, a., and Zhen, H. (2006) Heat release analysis on combustion and parametric study on emissions of HCCI engines fueled with 2-propanol/n-heptane blend fuels. *Energy & fuels*. 20(5): p. 1870-1878.
31. Bendu, H. and Murugan, S. (2014) Homogeneous charge compression ignition (HCCI) combustion: Mixture preparation and control strategies in diesel engines. *Renewable and Sustainable Energy Reviews*. 38: p. 732-746.
32. Aydoğan, B. and Calam, A. (2020) Combustion, performance and emission characteristics of a HCCI engine fuelled with n-butanol/n-heptane blends. *International Journal of Automotive Engineering and Technologies*. 9(1): p. 1-10.
33. Canakci, M. (2012) Combustion characteristics of a DI-HCCI gasoline engine running at different boost pressures. *Fuel*. 96: p. 546-555.
34. Maurya, R.K. and Agarwal, A.K. (2014) Experimental investigations of performance, combustion and emission characteristics of ethanol and methanol fueled HCCI engine. *Fuel processing technology*. 126: p. 30-48.
35. Halbe, M.H., Fain, D.J., Shaver, G.M., Kocher, L., and Koeberlein, D. (2017) Control-oriented premixed charge compression ignition CA50 model for a diesel engine utilizing variable valve actuation. *International Journal of Engine Research*. 18(8): p. 847-857.
36. Hakansson, A. (2007) CA50 estimation on HCCI engine using engine speed variations. Lund University: MSc Thesis.
37. Calam, A. (2021) Homojen Dolgulu Sıkıştırma ile Ateşlemeli Bir Motorda n-heptan-Tetrahidrofuran Karışımlarının Yanma, Performans ve Emisyonlara Etkisi. *Politeknik Dergisi*. p. 1-1.
38. Wang, Z., Liu, H., Ma, X., Wang, J., Shuai, S., and Reitz, R.D. (2016) Homogeneous charge compression ignition (HCCI) combustion of polyoxymethylene dimethyl ethers (PODE). *Fuel*. 183: p. 206-213.
39. Zhao, H. (2007) HCCI and CAI engines for the automotive industry. Elsevier.
40. Zheng, Z. and Yao, M. (2009) Charge stratification to control HCCI: Experiments and CFD modeling with n-heptane as fuel. *Fuel*. 88(2): p. 354-365.
41. Bendu, H., Deepak, B., and Murugan, S. (2016) Application of GRNN for the prediction of performance and exhaust emissions in HCCI engine using ethanol. *Energy conversion and management*. 122: p. 165-173.
42. Jun, D. and Iida, N. (2004) A study of high combustion efficiency and low CO emission in a natural gas HCCI engine. *SAE transactions*. p. 1306-1316.
43. Dec, J.E. and Yang, Y. (2010) Boosted HCCI for high power without engine knock and with ultra-low NOx emissions-using conventional gasoline. *SAE International Journal of Engines*. 3(1): p. 750-767.



## Modeling of an Electric Tractor and Determining Energy Consumption Values for Different Duties

Venkata Krishna Teja Thallapalli<sup>1</sup>, Ahmet Onur Kiyaklı<sup>2</sup>, Tolga Kocakulak<sup>3\*</sup>

<sup>1</sup> JB Institute of Engineering & Technology, Mechanical Engineering Department, Hyderabad, India

<sup>2</sup> Automotive Engineering Department, Faculty of Technology, Gazi University, Ankara, 06500, Turkey

<sup>3</sup> Burdur Mehmet Akif Ersoy University, Technical Sciences of High Vocational School, Burdur, Turkey

### ABSTRACT

In this study, a model of an electric tractor was created in MATLAB / Simulink environment, and performance and fuel consumption values were determined. The power transmission system, control unit, electric motor model, energy consumption, and battery subsystems of the electric tractor are included. Reference is made to a study in the literature, as there is no standardized test procedure for tractors. The energy consumption values of the electric tractor for rotary harrow, atomizer, and shredder duties have been examined. In determining the performance of the electric tractor, only the maximum speed value was included. If the reduction ratio of the electric tractor is 50, 60, 70, 80, 90, 100, the maximum speed values and the amount of energy consumed during the process of different duties were determined and evaluated. If the reduction ratio is below 50, no results could be obtained because he could not fulfill his duties in this study. It has been determined that if the reduction ratio is 50, the electric tractor consumes 3.985, 1.266, and 3.787 kWh energy in rotary harrow, atomizer, and shredder duties, respectively. It has been determined that if the reduction ratio is 100, the electric tractor consumes 3.604, 1.145, and 3.535 kWh energy in rotary harrow, atomizer, and shredder duties, respectively. It is concluded that if the reduction ratio of the electric tractor is 50, 60, 7, 80, 90, and 100, it reaches the maximum speed values of 62.25, 51.91, 44.52, 38.97.34.65, and 31.19 km / h, respectively.

**Keywords:** Agriculture; Electric vehicle; Modelling; Non-Road mobile machineries; Tractor

History  
Received:  
Accepted:

Author Contacts  
\*Corresponding Author

e-mail addresses : [kteja4000@gmail.com](mailto:kteja4000@gmail.com), [okiyakli@gmail.com](mailto:okiyakli@gmail.com), [tkocakulak@mehmetakif.edu.tr](mailto:tkocakulak@mehmetakif.edu.tr)  
ORCID numbers : 0000-0003-3368-1263, 0000-0002-5798-0762, 0000-0002-1269-6370

<http://dx.doi.org/10.29228/eng.pers.51651>

### 1. Introduction

In recent years, there has been increasing attention paid to the electrification of non-road mobile machinery, focusing on the machinery involved in construction and agricultural applications [1]. The tractor is a wheeled or tracked vehicle used for the traction of agricultural machinery [2]. This explanation remains quite simple for a machine, which currently involves a multitude of applications. This machine has been considered one of the advances, which significantly influences agriculture during the twenty-first century. Electric Tractor will save farmers' time because the electric tractor will be that its motor won't have around 300 sections that accompany the engine of a diesel tractor. Battery trading, regenerative braking, power reversal, and fast charging are among the features of the electric tractor. Electric tractors vary from traditional tractors in that they are driven by either diesel or gasoline. They are powered by electronic batteries that can recharge simply by plugging them into a

socket [3,4]. The electric tractor is deliberate by zero-emission, which is harmless to the ecosystem [5,6,7].

Electric tractors have several advantages over their diesel counterparts. Most prominently, they don't produce CO<sub>2</sub> emissions or other air pollution directly [8]. Indeed, the electricity they use is generated by natural gas or other fossil fuels or a blend of energy sources [9]. Electric tractors have fewer moving parts, which means fewer issues. As a result, repair and maintenance costs are reduced, and the tractor can operate for more extended periods [10,11]. Electric tractors are efficient; it gives excellent accuracy when it works. When it comes to converting thermal energy into mechanical energy, the diesel tractor is 35% efficient. Compare that with charging or discharging batteries 80% with the efficiency, while electric tractors are more efficient. The adoption of electric machines and battery technologies together with efficient diesel engines or, in some cases, replacing them in full electric configurations can reduce or completely avoid

local pollutant emissions [12,13,14]. Electric motors have certain drawbacks, such as charging and the need for costly line extensions [15]. Furthermore, speed-controlled motors are very expensive and necessitate a lot of specialized equipment, making installation more difficult.

This machinery is involved in various operations with different intensities; therefore, there is increasing interest in electrification, as the powertrain could achieve better versatility. For example, the hybrid powertrain could fulfill heavy operation requirements by combining ICE and Electric Machine (EM). Moreover, the proper power management of the load point of ICE and EM would allow better efficiency to be achieved for the overall system. On the other hand, working in pure electric mode only with the EM could be sufficient for light operations [16]. This latter case brings attractive benefits, such as reducing local emissions on crop fields or inside greenhouses, and reducing noise and vibration, improving the comfort and health of operators. Furthermore, other studies regarding the advantages of consumption and working autonomy have been carried out [17,18].

Ratzinger et al. created conventional, fully electric, serial hybrid, and parallel hybrid non-road vehicles. The model they created examined the effects of these vehicle structures and charging methods on CO<sub>2</sub> emission emissions. They made use of mathematical equations in the modeling process. They observed a 20% reduction in CO<sub>2</sub> emission when using the "charge-depleting" method instead of the "charge-sustaining" method on the serial hybrid vehicle. The vehicle structures discussed in the study determined that the conventional vehicle emitted 26.4, the fully electric vehicle 20.6, the parallel hybrid vehicle 23.1, and the serial hybrid vehicle 21.1 kg CO<sub>2</sub> / h. Therefore, this study concluded a fully electric vehicle structure according to CO<sub>2</sub> emission [19]. The work in [20] addresses the operational feasibility of agricultural tractors powered by electricity. The performed study is based on developing a small-scale prototype of EVs rated at 40 W using a DC motor. Besides, introducing a theoretical configuration for the electric tractor using a single electric motor is analyzed. However, a detailed analysis of the motor drive and control system associated with the electric tractor is not presented, and the performance evaluation of a real scale prototype.

On the other hand, the performance of a micro tractor is investigated in [21] using three different types of motors: a three-phase alternating current motor rated at 2.2 kW, 220 Vac, and 3465 rpm; a DC motor rated at 2.2 kW, 36 Vdc, and 2900 rpm; and an ICE rated at 2.6 kW and 3600 rpm. Zhang et al. worked on a new design scheme of the Electric tractor drive system, simplifies the power transmission mode, makes the chassis layout more flexible and simpler, puts forward the design theory and method of the driving system, and combines the case to design and calculate, completes the drive motor, the transmission, Parameter design and main performance analysis of main components such as Powerpack. The research shows that the 5km/h of the Power battery is 6.7h to meet the present 6h requirements [22]. Zhang et al. constructed an agricultural machine endowed with an industrial DC motor and performed plowing tests in different types of soils. The obtained results concluded that as the working depth of the plow increased, the electric motor torque oscillated with great amplitudes correlated with the soil resistance heterogeneity [23]. Thus, the research led to finding various ways to design and optimize the drive train system of such electric tractors [24]. Xiaofei et al., an electric AWD tractor, was developed

based on a power transmission system.

A simulation model reflecting the specifications of this electric AWD tractor was developed and verified using measured data from driving tests conducted under off-road and on-road conditions. The measured data were converted to torque using equations and were used for simulation conditions. A comparison of the simulation analysis results with the measured data showed that the torque generated on the axle was similar in value and shape, and we found no significant differences in the statistical analysis results. Although the SOC level showed a significant difference in the statistical analysis results, the rate of change per minute, and the SOC, the simulation results were reliable. The axle torque is closely related to the SOC level because it is proportional to the current supplied from the battery to the electric motor. As the measured data for both factors matched the simulation results, we determined that the operating time of the platform can be estimated through simulation. The workable time of the electric AWD tractor was estimated through simulation models and existing research data. As a result of the simulation, the workable time for plow tillage using the electric AWD tractor was estimated to be about 2.4 h. The results are less than the target hours (three hours) of work. In future studies, performance could be improved through battery optimization through a simulation [25].

In this study, an electric tractor model was created in MATLAB / Simulink environment. Energy consumption values and some performance values were determined in different duties on the created model. Rotary harrow, atomizer, and shredder are handled as missions. The energy consumption and performance values obtained because of the study were evaluated.

## 2. Material and Methods

In this study, an electric tractor's performance and energy consumption values were examined by creating a model in Matlab/Simulink environment. The effect of the power transmission reduction ratio on the maximum tractor speed was investigated. The energy consumption values of the electric tractor under different reduction ratios and different duty conditions were obtained and examined. The electric vehicle control system, power transmission system, electric motor, resistance forces, and battery models were created. Some of the electric tractor and simulation parameters used in the modeling process are given in Table 1.

Table 1. Electric tractor and simulation parameters

Parameters	Value
Mass	2500 kg
Battery voltage	700 V
Battery capacity	50 kWh
Electric motor max torque	320 Nm
Electric motor max speed	12000 rpm
Transmission ratio	50, 60, 70, 80, 90, 100
Aerodynamic coefficient	0.68
Wheel diameter	1500 mm
Powertrain systems efficiency	0.97

### 2.1 Modeling of Electric Tractor Control System

The electric tractor model consists of many systems and subsystems. These systems work simultaneously with each other. The control scheme, including the system and subsystems of the electric tractor, is given in Figure 1.

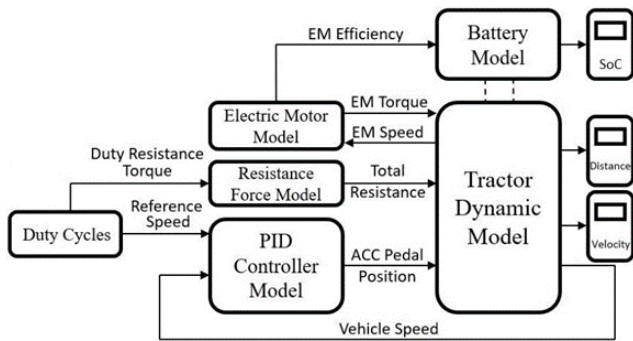


Figure 1. Schematic representation of electric tractor systems

PID controls carry out gas and brake pedal control of the electric tractor. The speed information of the duty cycle is accepted as the reference speed of the tractor. The reference speed is transferred to the PID controller model, and the instantaneous speed information is obtained from the vehicle dynamic model. The PID controller thus calculates the accelerator and brake pedal position. The PID control model is shown in Figure 2.

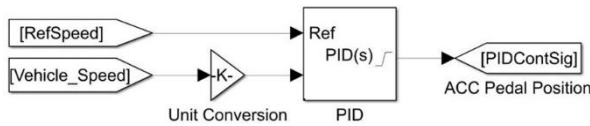


Figure 2. PID controller model

### 2.2 Modeling of Electric Tractor Powertrain System

In the electric tractor, the power transfer between the electric motor and the wheels is carried out by the powertrain system. The schematic representation of the electric tractor power transmission system is shown in Figure 3.

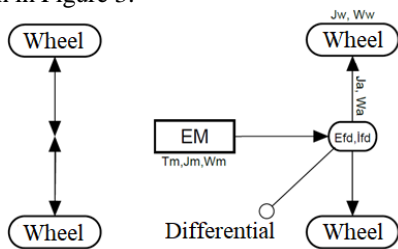


Figure 3. Schematic representation of the power transmission system

The angular acceleration of that shaft is calculated by dividing the net torque acting on a shaft by the moment of inertia of that shaft. By integrating the angular acceleration, the angular velocity of that shaft is obtained. With this principle, the transfer function of the electric vehicle powertrain is derived. The transfer function representing the electric vehicle powertrain system is given in Equation 1.

$$\omega_w = \int_t \frac{T_m i_{fd} \eta_{fd} - T_L}{J_m i_{fd}^2 \eta_{fd} + 2J_a + 4J_w} dt \quad (1)$$

In the equation,  $T_m$  represents engine torque,  $i_{fd}$  represents differential reduction ratio,  $\eta_{fd}$  represents differential efficiency,  $J_a$  represents axle moment of inertia, and  $J_w$  represents wheel moment of inertia.  $T_L$  represents the torque to the total load acting on the tractor and is calculated by adding the resistance forces acting on the tractor and the duty cycles.

### 2.3 Modeling of Electric Motor Model

In the electric motor model used on the electric tractor, Remy brand HVH250-090 model electric motor maps, which can produce a maximum torque of 320 Nm and reach a maximum speed of 12000 rpm, are used. The speed, torque, and efficiency maps of the electric motor are shown in Figure 4.

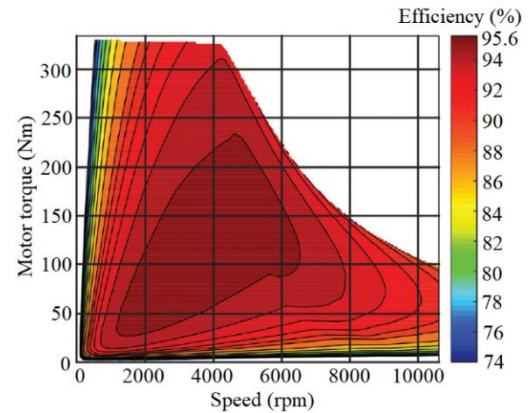


Figure 4. Electric motor speed, torque, and efficiency map

The engine speed calculated in the tractor dynamic model is transmitted to the electric motor subsystem. In the electric motor model, the maximum output torque of the motor is determined using the 2D motor torque map, and the motor efficiency is determined using the 3D motor efficiency map. The Simulink model of the electric motor is shown in Figure 5.

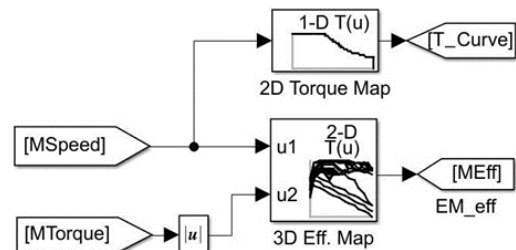


Figure 5. Electric motor Simulink model

### 2.4 Electric Tractor Resistance Force Model

The road resistances that the electric tractor encounters during the movement process are included in the model. Calculation of the acceleration resistance force is carried out by Equation 2. In the equation,  $m$  represents the tractor mass, and  $a$  represents the acceleration.

$$F_i = ma \quad (2)$$

The rolling resistance force encountered by the electric tractor is calculated by Equation 3. Thus,  $C_r$  is the rolling resistance coefficient, and  $g$  is the gravitational acceleration.

$$F_r = mgC_r \quad (3)$$

Since high speeds are not reached in agricultural vehicles and construction machines, the aerodynamic resistance force is not considered very important and can be neglected. In this model, the maximum speed values that the electric tractor can reach are calculated. Therefore, the aerodynamic drag force is included in the model. The aerodynamic drag force is calculated by Equation 4. In the equation,  $C_d$  is the aerodynamic drag coefficient,  $A_f$  is the front section area, and  $V$  is the vehicle speed.

$$F_a = 0.5\rho C_d A_f V^2 \tag{4}$$

The sum of the resistance forces acting on the electric tractor is calculated by Equation 5.

$$F_{Load} = F_i + F_a + F_r \tag{5}$$

The calculation of the total resistance torque is calculated by the product of the total resistance force and the radius of the wheel and is given in Equation 6.

$$T_{resistance} = F_{resistance} \times r_w \tag{6}$$

The Simulink model, in which the resistance forces acting on the electric vehicle and the torque values affected by the duties are calculated, is given in Figure 6.

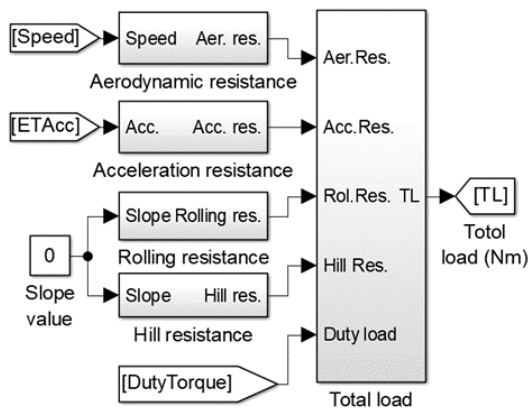


Figure 6. Model of resistance forces on the electric tractor

### 2.4 Electric Tractor Resistance Force Model

The energy consumption values of the electric tractor in rotary harrow, atomizer, and shredder duties were obtained. Since there are no standard test procedures established for the duties of the electric tractor, the cycle values of the duties are taken from the reference source [26,27]. The speed and torque cycles of the duties were created by making the necessary adjustments in the referenced graphics. The speed cycles of the duties are shown in Figure 7. Rotary harrow and atomizer duty has a speed of 3.4 km / h, and shredder duty has a speed of 5 km / h. Rotary harrow duty is performed for 800 seconds, atomizer duty for 250 seconds, and shredder duty for 700 seconds.

Torque graphics of the duty cycles used in the study are given in Figure 8. The highest torque values were encountered in the rotary harrow mission. Conversely, the lowest torque value was obtained in the shredder duty.

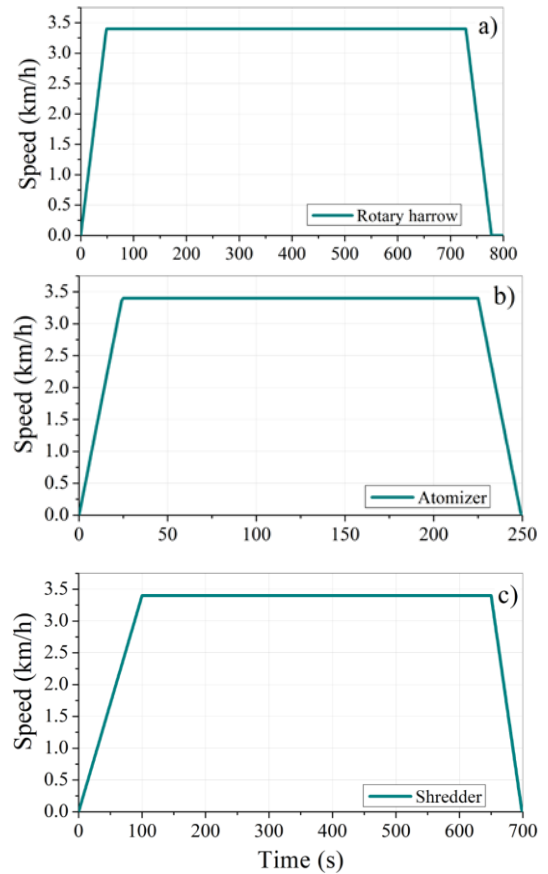


Figure 7. Duty cycle speed graph for rotary harrow (a), atomizer (b) and shredder (c)

### 3. Result and Discussion

In this study, energy consumption and performance values for different duties are calculated by creating a model of an electric tractor. In the simulation process, three different speed cycles were used to reach a maximum speed of 3.4 km / h and 5 km / h for the electric tractor. The results, including comparing the actual speed and reference speed values of the electric tractor during the rotary harrow, atomizer, and shredder missions, are shown in Figure 9

Suppose the total reduction ratio of the electric tractor is 70. In that case, the instantaneous efficiency values of the electric motor obtained during the rotary harrow, atomizer, and shredder missions are shown in Figure 10. Thus, an electric tractor rotary harrow, atomizer, and shredder duties have been observed to have reached the minimum 81%, 83%, 85%, and maximum 88%, 88%, 91% efficiency values, respectively.

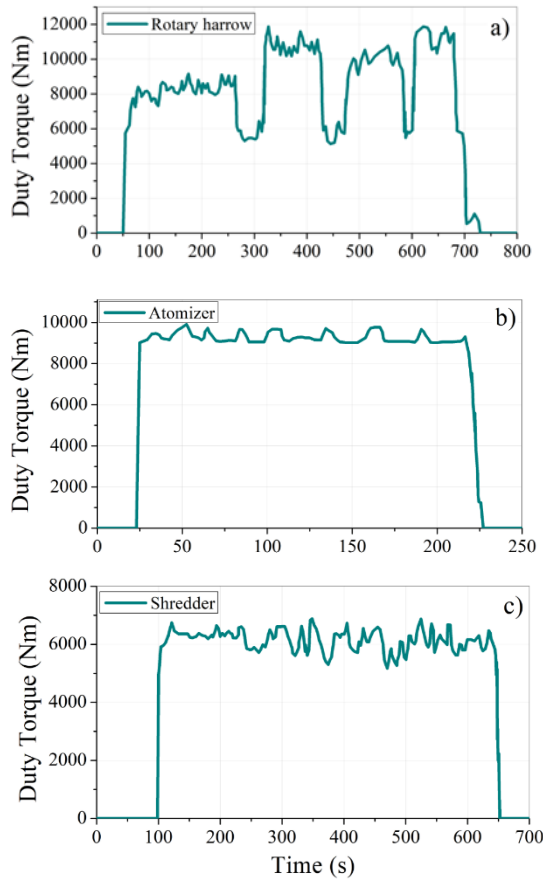


Figure 8. Duty cycle torque graph for rotary harrow (a), atomizer (b) and shredder (c)

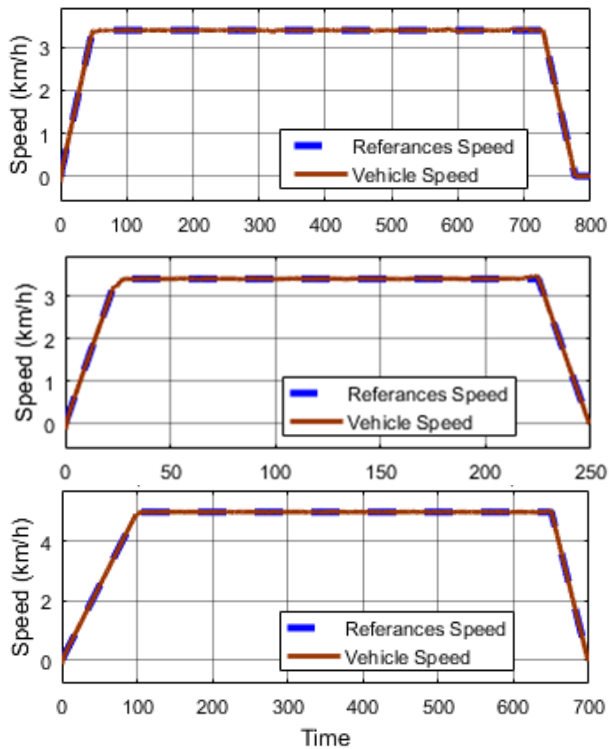


Figure 9. Comparison of References and Vehicle Speed for rotary harrow (a), atomizer (b), shredder (c)

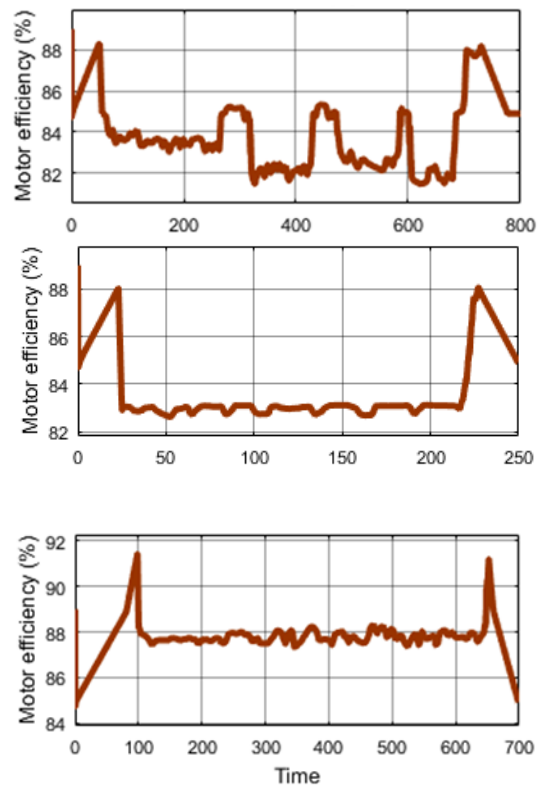


Figure 10. Motor efficiency graph for rotary harrow (a), atomizer (b), shredder (c)

It has been observed that if the reduction ratio of the electric tractor is 70, it can go over 40 km / h. If the reduction ratio is 70, energy consumption values have been calculated in rotary harrow, atomizer, and shredder missions and are given in Figure 11. Rotary harrow duty takes 800 seconds, atomizer duty takes 250 seconds, and shredder duty lasts 700 seconds. Therefore, it is seen that the energy consumption is low due to the low duty time of the atomizer.

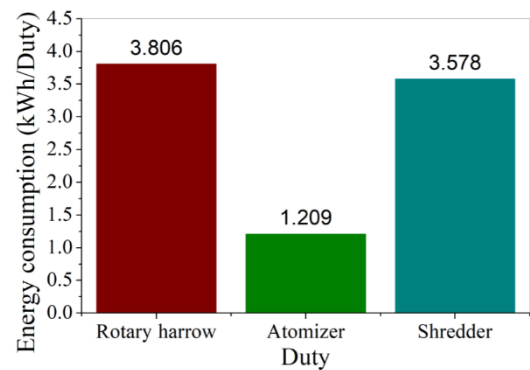


Figure 11. Energy consumption values of the electric tractor in different duties

Suppose the reduction ratio value is lower than 50. In that case, the torque value that can perform the specified duties cannot be exceeded, and the tractor cannot travel at reference speed values. Using the electric tractor in three different duties, the situation of 50, 60, 70, 80, 90, and 100 reduction ratio was examined. The graphic containing the energy consumption values of the electric tractor depending on different duties and different reduction ratios is given in Figure 12. During the

Rotary Harrow mission, 3,985, 3,882, 3,806, 3,746, 3,674 and 3,604 kWh energy consumption were respectively. The atomizer duty, respectively, 1,266, 1,233, 1,209, 1,19, 1,168, and 1,145 kWh energy consumption, was realized. The Shredder mission, 3,787, 3,683, 3,578, 3,485, 3,408, and 3,535 kWh energy consumption, was achieved, respectively. If the reduction ratio of the electric tractor was increased from 50 to 100, energy savings of 9.56% were achieved in rotary harrow duty, 9.55% in atomizer duty, and 6.65% in shredder duty.

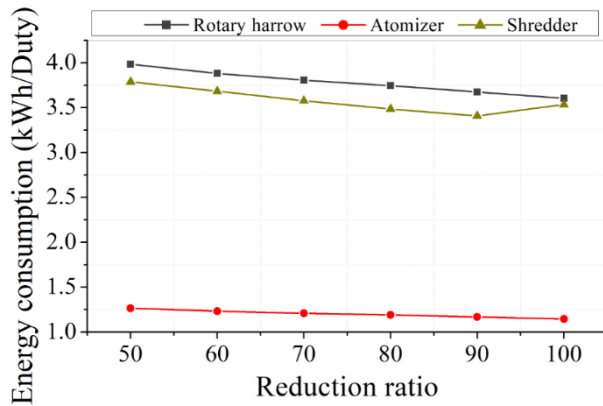


Figure 12. Fuel consumption value (kWh) for different duty and reduction ratio

The maximum speed performance values of the electric tractor in different reduction ratios are shown in Figure 13. For example, if the reduction ratio is 50, 60, 70, 80, 90, and 100, it is seen that the maximum speed values are 62.25, 51.91, 44.52, 38.97, 34.65, and 31.19 km / h, respectively.

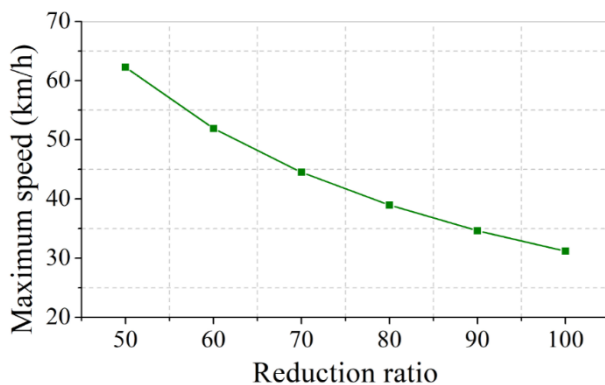


Figure 13. Performance characteristic for different reduction ratio

#### 4. Conclusion

In this study, a model of an electric tractor has been created, and different duties have investigated energy consumption. If the reduction ratio of the electric tractor is 50, it has been determined that it consumes 3,985, 1,266, and 3,787 kWh energy in rotary harrow, atomizer, and shredder duties, respectively. If the reduction ratio is below 50, the energy consumption values are not included, since the required torque value cannot be provided for the duties dealt with in the study. The effect of the electric tractor reduction ratio on energy consumption values was determined. If the reduction ratio value is 100 instead of 50, it was observed that the energy consumption decreased by 9.56%, 9.55%, and 6.65% in rotary harrow, atomizer, and shredder duties, respectively. If

the reduction ratio value is 100 instead of 50, the result is that the maximum vehicle speed drops from 62.25 km / h to 31.19 km / h.

#### Nomenclature

$F_i$	Acceleration resistance force
$F_r$	Rolling resistance force
$C_r$	Rolling resistance coefficient
$A_f$	Frontal area of the tractor
$F_a$	Aerodynamic drag force
$C_d$	Aerodynamic drag coefficient
$r_w$	Radius of the wheel

#### Conflict of Interest Statement

The Authors declare that there is no conflict of interest.

#### CRedit Author Statement

**Venkata Krishna Teja Thallapalli:** Data curation, Resources, Methodology

**Ahmet Onur Kiyaklı:** Conceptualization, Visualization, Writing–review & editing, Validation

**Tolga Kocakulak:** Investigation, Supervision, Writing-original draft, Project administration

#### References

- Lajunen, A., Sainio, P., Laurila, L., Pippuri-Mäkeläinen, J., & Tammi, K. (2018). Overview of powertrain electrification and future scenarios for non-road mobile machinery. *Energies*, 11(5), 1184.
- Bawden, O. J. (2015). Design of a lightweight, modular robotic vehicle for the sustainable intensification of broadacre agriculture (Doctoral dissertation, Queensland University of Technology).
- Solmaz, H., & Kocakulak, T. (2020). Determination of lithium-ion battery characteristics for hybrid vehicle models. *International Journal of Automotive Science and Technology*, 4(4), 264-271.
- Kocakulak, T., Solmaz, H. (2020). Control of pre and post-transmission parallel hybrid vehicles with fuzzy logic method and comparison with other power systems. *Journal of the Faculty of Engineering and Architecture of Gazi University*, 35(4), 2269-2286.
- Hoffmann, P. (2012). *Tomorrow's energy: hydrogen, fuel cells, and the prospects for a cleaner planet*. MIT press.
- Sperling, D. (2018). *Three revolutions: Steering automated, shared, and electric vehicles to a better future*. Island Press.
- RD, C. (2020). Study on the behavior of a battery mounted on an electric tractor prototype. *INMATEH-Agricultural Engineering*, 62(3).
- Luna, T. F., Uria-Maldonado, M., Silva, M. E., Vaz, C. R. (2020). The influence of e-carsharing schemes on electric vehicle adoption and carbon emissions: An emerging economy study. *Transportation Research Part D: Transport and Environment*, 79, 102226.
- Raheli, E., Wu, Q., Zhang, M., Wen, C. (2021). Optimal coordinated operation of integrated natural gas and electric power systems: A review of modeling and solution methods. *Renewable and Sustainable Energy Reviews*, 145, 111134.
- Cortés-Murcia, D. L., Prodhon, C., Afsar, H. M. (2019). The electric

- vehicle routing problem with time windows, partial recharges, and satellite customers. *Transportation Research Part E: Logistics and Transportation Review*, 130, 184-206.
11. Karki, A., Phuyal, S., Tuladhar, D., Basnet, S., Shrestha, B. P. (2020). Status of pure electric vehicle power train technology and future prospects. *Applied System Innovation*, 3(3), 35.
  12. Lajunen, A., Sainio, P., Laurila, L., Pippuri-Mäkeläinen, J., Tammi, K. (2018). Overview of Powertrain Electrification and Future Scenarios for Non-Road Mobile Machinery. *Energies*, 11, 1184.
  13. Kiyakli, A. O., & Solmaz, H. (2018). Modeling of an electric vehicle with MATLAB/Simulink. *International journal of automotive science and technology*, 2(4), 9-15.
  14. Yurdaer, E., & Kocakulak, T. (2021). Comparison of Energy Consumption of Different Electric Vehicle Power Systems Using Fuzzy Logic-Based Regenerative Braking. *Eng Perspect*, 1(1), 11-21.
  15. Brinkel, N. B. G., Schram, W. L., AlSkaif, T. A., Lampropoulos, I., van Sark, W. G. J. H. M. (2020). Should we reinforce the grid? Cost and emission optimization of electric vehicle charging under different transformer limits. *Applied Energy*, 276, 115285.
  16. Xie, Y., Li, Y., Zhao, Z., Dong, H., Wang, S., Liu, J., Duan, X. (2020). Microsimulation of electric vehicle energy consumption and driving range. *Applied Energy*, 267, 115081.
  17. Troncon, D., Alberti, L. Mattetti, M. (2019). A Feasibility Study for Agriculture Tractors Electrification: Duty Cycles Simulation and Consumption Comparison. In *Proceedings of the 2019 IEEE Transportation Electrification Conference and Expo (ITEC)*, Detroit, MI, USA, 19–21, 1–6.
  18. Troncon, D., Alberti, L., Bolognani, S., Bettella, F., Gatto, A. (2019). Electrification of agricultural machinery: A feasibility evaluation. In *Proceedings of the 2019 Fourteenth International Conference on Ecological Vehicles and Renewable Energies*, Monte-Carlo, Monaco, 8–10, 1–7.
  19. Ratzinger, J. M., Buchberger, S., Eichseder, H. (2020). Electrified powertrains for wheel-driven non-road mobile machinery. *Automotive and Engine Technology*, 1-13.
  20. Volpato, C.E.S., de Paula, V.R., Barbosa, J.A. (2016). Evaluation of the operational viability of the use of electricity as a source of power in agricultural tractors. 2016 ASABE Annual Int. Meeting, Orlando, FL, USA, 1.
  21. Rodrigues, D. E., Teixeira, M. M., Fernandes, H. C., Modolo, A. J., & Rodrigues, G. J. (2006). Desempenho de um microtrator utilizando-se motores com diferentes alternativas energéticas. *Acta Scientiarum. Technology*, 28(1), 55-63.
  22. Xiaofei Zhang. (2017). Design Theory and Performance Analysis of Electric Tractor Drive System. Tianjin, China.
  23. Xie, B., Zhang, C., Chen, S., Mao, E. R., Du, Y. F. (2015), Transmission performance of two-wheel drive electric tractor. *Transactions of the Chinese Society for Agricultural Machinery*, 46(6), pp. 8-13.
  24. Xiaofei Z., (2017), Design Theory and Performance Analysis of Electric Tractor Drive System, *International Journal of Engineering Research & Technology (IJERT)*, pp 235–238;
  25. Baek, S. Y., Kim, Y. S., Kim, W. S., Baek, S. M., & Kim, Y. J. (2020). Development and Verification of a Simulation Model for 120 kW Class Electric AWD (All-Wheel-Drive) Tractor during Driving Operation. *Energies*, 13(10), 2422.
  26. Mocera, F. (2021). A Model-Based Design Approach for a Parallel Hybrid Electric Tractor Energy Management Strategy Using Hardware in the Loop Technique. *Vehicles*, 3(1), 1-19.
  27. Mocera, F., Somà, A. (2020). Analysis of a Parallel Hybrid Electric Tractor for Agricultural Applications. *Energies*, 13(12), 3055.